12-14-2015

Two-Dimensional Transient Spectroscopy Measuring Heterogeneity in Electronic and Rotational Dynamics

Haorui Wu
University of South Carolina - Columbia

Recommended Citation

Wu, H.(2015). *Two-Dimensional Transient Spectroscopy Measuring Heterogeneity in Electronic and Rotational Dynamics.* (Doctoral dissertation). Retrieved from https://scholarcommons.sc.edu/etd/3198

TWO-DIMENSIONAL TRANSIENT SPECTROSCOPY MEASURING HETEROGENEITY IN ELECTRONIC AND ROTATIONAL DYNAMICS

by

Haorui Wu

Bachelor of Science
Lanzhou University, 2010

Submitted in Partial Fulfillment of the Requirements

For the Degree of Doctor of Philosophy in

Chemistry

College of Arts and Sciences

University of South Carolina

2015

Accepted by:

Mark A. Berg, Major Professor

Sophya V. Garashchuk, Committee Chair

S. Michael Angel, Committee Member

Thomas M. Crawford, Committee Member

Lacy Ford, Senior Vice Provost and Dean of Graduate Studies

DEDICATION

This dissertation dedicates to all my family members, my mentor, my friends, and to all those who have been there supporting and helping me.

ACKNOWLEDGEMENTS

I would never been able to finish my graduation work without the guidance from these people I'm greatly thankful.

First, I would like to thank my advisor, Prof. Mark Berg, for all the efforts and patiences he puts on me, and all the encouraging advices when I was struggling. Over and over, he gave me helpful ideas and led me to the right direction. One important thing I learned is to not only acquire knowledge in my own field, but also absorb all information that is useful. All the projects I've done provided me chances to learn things more comprehensively and expanded my realm of knowledge. I believe that these will benefit me a lot in the future, too.

Next, I want to express my thanks to my committee members, Prof. Sophya Garashchuk, Prof. Michael Angel and Prof. Thomas Crawford. Thanks for their nice, friendly communications and useful advices on my graduation work.

In addition, I would like to thank for all my colleagues, Dr. Kalyanasis Sahu, Dr. Sean Kern, Dr. Yuri Glinka, Dr. Sachin Dev Verma, David Phillips and Jason Darvin. It's my great pleasure to work with all of you. I would like to acknowledge National Science Foundation (NSF) for providing us fundings to carry on experiments and researches.

I would also like to thank for all the friends I met here in Columbia. My life is becoming interesting and wonderful because all of you. Our friendship is a treasure thing to me. Finally, I would like to express my deepest thanks to all my family members,

without their supports, it’s impossible for me to live alone in a foreign country for five years. Lots of things can change during five years, but I know their love to me will never change.

ABSTRACT

Multiple population-period transient spectroscopy (MUPPETS) is a picosecond, time resolved experiment that uses a sequence of six laser pulses. It was previously known that MUPPETS could measure heterogeneity in electronic-state decay. This dissertation presents two projects that extend MUPPETS to new processes. One process is the extension from 2-level system into 3-level system, another new process extends the kinetics from electronic decay to rotational decay. In addition, a third, ongoing project on rotational dynamics in ionic liquids will also be discussed briefly.

The first project consisted of two main parts. The first part focused on the biexciton decay in semiconductor nanoparticles. The power dependence of the excited state decay in nanoparticles has been attributed to biexcitons, but those measurements are easily contaminated with other species. New theoretical work in excitonic systems shows that MUPPETS can measure biexciton decays free from contaminations. Our experiments successfully isolate the biexciton decay of CdSe/ZnS core–shell nanoparticles. The biexciton signal shows a highly dispersed, nonexponential dynamics, which is inconsistent with current theories of Auger recombination.

The second part of the first project investigated the heterogeneity of exciton decay. There is a fast, nonradiative decay in the exciton decay of core–shell nanoparticles, which has been attributed to a subset of poorly passivated particles. Using a new theory of multi-level systems, our MUPPETS experiments showed that such a subpopulation does not exist. We suggest that the early component in exciton decay is caused by surface relaxation.

The second project probed heterogeneity in the local dynamics of polymers, as sensed by solute rotation. The rotation of a solute in a small molecule solvent is exponential, but it becomes nonexponential in a polymer melt. This nonexponential behavior may be explained by either variations in the local viscosity of the polymer—a heterogeneous model—or local anisotropy of the polymer structure—a homogeneous model. To measure heterogeneity in rotation rates, we extended the original MUPPETS experiment to a polarized version. The new method was demonstrated on the anisotropy decay of Pyrromethene 597 in poly(dimethylsiloxane) (PDMS). The results show strong molecule-to-molecule variation in the rotation rate. They are consistent with local, short-length scale variations in viscosity within the polymer. No evidence for local anisotropy was found.

In the final projects, the rotational dynamics of a solute in ionic liquids was measured with 1D polarization experiments. Experiments and simulations have suggested that heterogeneous microstructures exist in ionic liquids. A new signal normalization channel was built to reduce noise, increase long term stability and improve the ability to detect nonexponential decay. Rotational decays are measured for ionic liquids with different chain lengths and different mixture ratio with acetonitrile. Weakly nonexponential decays were found for long chains, but none was found for short chains. Experiments and analysis are ongoing.

TABLE OF CONTENTS

LIST OF FIGURES

LIST OF ABBREVIATIONS

MDCS	Multidimensional Coherence Spectroscopy
MEM	Maximum-Entropy Method
MUPPETS	Multiple Population-Period Transient Spectroscopy
PDMS	Poly(dimethylsiloxane)

CHAPTER 1 INTRODUCTION

1.1 OVERVIEW

Nonexponential kinetics is common as the system studied becomes more complex. Instead of having a single kinetic rate, which can be described by an exponential function, the measured rates can have a broad dispersion. This rate dispersion is generally attributed to two mechanisms: first is that each molecule can have differernt relaxation rate thus the ensemble average gives a nonexponential decay, this is called a heterogeneous mechanism. Another explanation is that each molecule is inherently nonexponential, but decays for all the molecules are identical, this is known as a homogeneous model.

The Berg group has pioneered two-dimensional methods to resolve this problem. Previously, MUPPETS was utilized in 2-level systems to detect heterogeneity in electronic state decay. It distinguishes the cause of rate dispersion between heterogeneous and homogeneous mechanism.

This thesis describes three new technical things. 1) showed how to isolate biexciton from exciton signal, 2) measured heterogenetity in multilevel system, 3) showed how to include polarization to measure heterogeneity in molecular rotation

Using these new technics we discovered: 1) biexciton shows a biexponential form and its mechanism is undetermined, 2) nonradiative decay in core-shell nanoparticles is due to surface relaxation, 3) heterogeneity in local viscosity are formed inside polymer.

Five papers have been published based on the work in this thesis and correspond to Chapts 2-6. Chapter 2 deals with the theoretic work that extends MUPPETS from 2-level to multi-level system. It was published as Wu, H.; Berg, M. A., Journal of Chemical Physics 2013, 138 (3), 034201. Chapter 3 focues on isolation the biexciton signal experimentally. It was published as Sahu, K.; Wu, H.; Berg, M. A., Journal of the American Chemical Society 2013, 135 (3), 1002–1005. Chapter 4 measures the cause of heterogeneity in nonradiative decay in core-shell nanoparticles. It was published as Sahu, K.; Wu, H.; Berg, M. A., Journal of Physical Chemistry B 2013, 117 (49), 15257-15271. Chapter 5 discusses the effect of other processes in experiments such as thermal grating. It was published as Wu, H.; Sahu, K.; Berg, M. A., Journal of Physical Chemistry B 2013, 117 (49), 15272-15284. Chapter 6 investigates heterogeneity in rotational dynamics in polymer melt. It was published as Wu, H.; Berg, M. A., Journal of Physical Chemistry Letters 2014, 5 (15), 2608–2612. An additional paper on the theory of polarized MUPPETS is anticipated in the future.

1.2 MULTIPLE POPULATION-PERIOD TRANSIENT SPECTROSCOPY

<u>Mu</u>ltiple <u>P</u>opulation-<u>Pe</u>riod <u>T</u>ransient <u>S</u>pectroscopy (MUPPETS) is a two-dimensional (2D) time resolved spectroscopy. It is two-dimensional because two evolving periods are involved. Two excitation pulses are separated by a first evolving period τ_1, the change in absorption due to both excitation pulses is measured in another evolving time τ_2. The first evolution period in MUPPETS is usually worked as a rate filter, it filters fast subensembles in a heterogeneous system. And the dynamics of slow subensembles are probed at second evolution period. Depending on the length of first evolving period, dynamics of assemble average versus selected groups can be extracted.

Although only three interactions are necessary in the MUPPETS experiment, six pulses are used in practice (Figure 1.1). Lower order three beam or four beam signals are removed due to the unmatching of excitation and detection wave-vector. Therefore, a unique MUPPETS signal is generated using this 6 beam geometry. Two probes are detected by photodiodes, and the difference of the two signals was measured by lock-in amplifier.

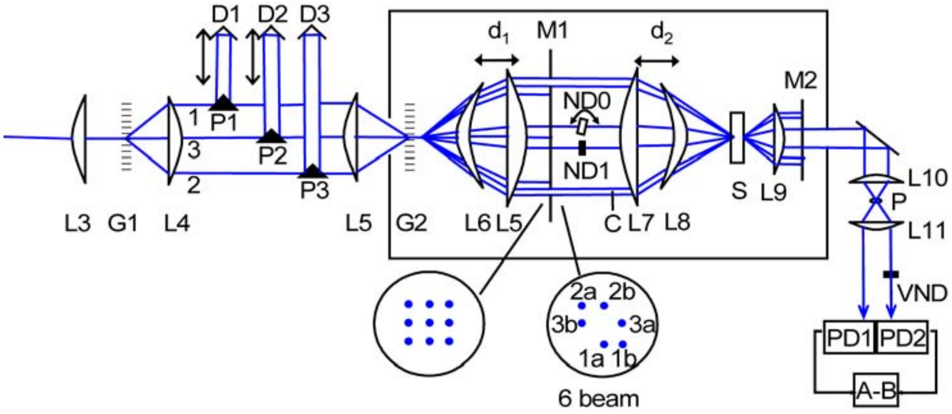

Figure 1.1. Schematic of MUPPETS setup. L1–L10 lenses, G1 and G2 transmission gratings, P1–P3 reflective prisms, D1–D3 delay lines, C chopper, ND neutral density filter, T1–T5 timing/phase plates, M1 and M2 masks, S sample, P pinhole, VND linear variable neutral density filter, PD1 and PD2 matched photodiodes, A-B Differential inputs of a lock-in amplifier. Different masks are used for 1D and 2D transient grating experiments.

1.3 NANOPARTICLE DYNAMICS MEASURED WITH MULTI-LEVEL MUPPETS

1.3.1 Biexciton Dynamics

In nanoparticles, the nonradiative decay greatly impedes the applications that require strong emission such as light-emitting diodes (LEDs) [1-4], bio-imaging[5, 6], and nanocrystal (NC) lasing.[7, 8] One major process that decreases the efficiency of emission is biexciton decay[9, 10]. Another process of nonradiative decay is through the surface trapping sites.

Previous measurements of biexciton decay were complicated by the possible presence of other species. By extending the theory of MUPPETS from 2-level model to a 3-level one, we predicted the possibility of isolating biexciton from other interferences. In this model, three energy states are used to represent ground state, exciton state and biexciton state, respectively. Complete MUPPETS pathways are then expanded. The amplitude for each pathway is calculated using a nonorthogonal basis set. Two 2D correlation functions contribute to the MUPPETS signal. Detailed discussion is covered in chapter 2.

One of the significance of this theory is it predicts the sign of exciton and biexciton signal to be opposite. MUPPETS is then used to look at biexciton decay in nanoparticles experimentally. Since the biexciton decays in a faster time scale and has a negative sign compared to exciton, the total MUPPETS signal should have a rise feature at short time. A strong power dependent effect is observed in the MUPPETS result at $\tau_1 = 0$. A linear regression technique decomposes this power dependent data into two components: a power-independent component repsents the component not changing with laser power and a power-dependent component corresponds to the part varying with power. However, the rise feature of biexciton is not seen in MUPPETS data at any power. It took us a while to realize that the rise feature will only be presented at very low power. At high power, it will be obscured by the positive biexciton signal in power-dependent part. Finally, the negative biexciton amplitude is observed in MUPPETS at a very low power condition. Subtracting power-independent MUPPETS result from the pump–probe result gives us the separated biexciton signal.

The biexciton signal is fitted to a biexponential function. Biexciton decay is generally believed to have an Auger recombination mechanism. However, the current explanation of Auger mechanism is a signle exponential decay. Thus, either current theory on biexciton decay needs to be revised or new theory needs to be discovered to explain this phenomenon.

1.3.2 Core-Shell exciton decay

The cause of nonradiative decay in core-shell nanoparticles is still a mystery. One explanation could be the defects on the surface, this could allow electrons to relax nonradiatively. However, for these high quantum yield core-shell nanoparticles, most of the surface defects should have been passivated. Another possibility is that the surface of the nanoparticle is undergoing a relaxation process during the excitation, for each electron, the decay is not in a constant rate, therefore, the ensemble decay is still nonexponential.

We used multi-level MUPPETS to investigate the cause of heterogeneity in exciton decay. The full set of 2D MUPPETS experimental data is reported for the first time. Depending on whether the exciton is homogeneous or heterogeneous dispersed and whether exciton/biexciton is correlated or not, four models can be established. The two 2D correlation functions that contribute to MUPPETS signal are then derived differently in these four models. MUPPETS data at all τ_1 matches best with the prediction of homogeneous exciton decay and uncorrelated exciton/biexciton model. We suggest a surface relaxation mechanism is accounting for this nonexponential behavior. The fact single exciton decay is not correlated with the biexciton decay suggests that the biexciton decay has an independent mechanism. More detailed discussion is shown in chapter 4.

1.4 LOCAL POLYMER DYNAMICS MEASURED WITH POLARIZED MUPPETS

Our third new technique investigated the rotational behavior in different solvents/fluids. In small molecule solvents, the rotational dynamics of a solute is usually exponential. However, in polymers, the anisotropy decay becomes nonexponential. It is still unknown the cause of this nonexponential behavior. One possible explanation is that local viscosity is developed in the polymer melts. Therefore, molecules in different local regions are sensing different viscosity and rotate differently, but each single rate is an exponential one. Another explanation argues the existence of anisotropic local structure created by long chain solvents. On a faster time scale, solutes are wobbling around this local anisotropy axis, on a slower scale, both the solute and solvent molecules are rotating together. Here, for each solute, the rotation is nonexponential.

Polarized MUPPETS was developed to address this problem. In 1D polarization experiments, the rotational dynamics is decomposed into two correlation functions, a rotational component $C^{\{2\}}(\tau_1)$ and an electronic component $C^{\{0\}}(\tau_1)$. The 1D rotation can be easily obtained from these two correlation functions. In MUPPETS experiments, four 2D correlation functions are generated, depending on whether electronic decay or rotational decay is measured in τ_1 and τ_2. The one measures rotational dynamics during both τ_1 and τ_2 is of most interest to us. However, it is nontrivial to measure this correlation function. As all six pulses in MUPPETS are polarized, even if there are two choices of polarization for each pulse, as much as 64 different combinations can be generated. Not to mention geometries with other polarization choices. Fortunately, using our methods discussed in previous reference[11], we found a set of two measurements can be used to extract the 2D rotational component in polarized MUPPETS experiments.

During implementing the optical setup for polarized MUPPETS, we encountered several problems. In order to adjust the polarization for each pulse, three sets of half wave-plates were put in between delaylines. In order to improve the delayline moving stability, we replaced a reflective mirror on one delayline into a corner cube. This accompanies another problem, that is, the corner cube will always change the polarization of input pulse. Therefore, another quarter wave-plate was put in to compensate the change brought by the corner cube. Finally, an extinguish ratio of 1000:1 is achieved in current setup for all pulses.

Polarized MUPPETS was then used to investigate the cause of heterogeneity in rotational decay in polymer melt. Measurements were done at two polarization sets mentioned above at varies τ_1. At $\tau_1 = 0$, 2D rotation is identical to the 1D rotation, which indicates that the rate filter is off. By increasing filtering time τ_1, the measured 2D rotational rate is becoming slower and more single exponential. This indicates the filtering of rapid relaxation molecules, suggests the existence of regions with different local viscosity. At $\tau_1 = 500$ ps, the 2D rotation is found to be nearly single exponential. This further confirmed the prediction of heterogeneous mechanism. Complete description of this topic in covered in chapter 6.

1.5 NONEXPONENTIAL SOLUTE ROTATION IN IONIC LIQUIDS

One additional work I've also done is to understand the cause of heterogeneity in rotational decay in ionic liquids. The rotational decay in these ionic liquids is also found to be dispersed. Simulations on molecular dynamics have speculated the microstructure of these liquids, i.e., polar and nonpolar regions separated in those liquids.[12] The solvation response studies have found that the nonexponential behavior in diffuse part is due to the existence of spatial heterogeneity in these liquids. Thus, the study of heterogeneity in rotations experimentally would also be a great complement to these researches.

Two sets of 1D polarization experiments were done to explore the rotational dynamics of these liquids. In one set, probes were dissolved into imidazolium ionic liquids (IL) with different alkyl side chain mixed with acetonitrile ($x_{IL} = 0.2$), it is found the rotational decay slows down as the alkyl chain lengthen. The shape of rotational decay becomes stretched exponential in these ionic liquids, which might be due to the development of local heterogeneous microstructure. But this change in the shape of decay is not as obvious as we expected. In the second series, Probe molecules were dissolved into one mixture of ionic liquid and acetonitrile, but the molar fraction of ionic liquids is varying. In that set, the decay time increases as the amount of ionic liquids increase, but again no obvious change in the shape of decay is found.

CHAPTER 2 MULTIPLE POPULATION-PERIOD TRANSIENT SPECTROSCOPY IN EXCITONIC SYSTEMS

2.1 INTRODUCTION

Kinetic measurements are a major subset of physical chemistry and take on many different forms appropriate to different processes and timescales. Nonetheless, almost all are one dimensional (1D): a single period of time exists between a single perturbation of the system and a later detection of its evolved state. Our group has been exploring multidimensional kinetics in which there is more than one perturbation, and thus, more than one period of time evolution.[11, 13-21] We have called our approach, which uses weak optical perturbations, multiple population-period transient spectroscopy (MUPPETS). So far, its focus has been on nonexponential relaxation (rate dispersion) in two-level systems. In those systems, MUPPETS can separate homogeneous and heterogeneous contributions to rate dispersion. This paper lays a theoretical foundation for MUPPETS in multilevel systems and especially in excitonic systems—those with equally spaced levels and optical transitions and relaxations that occur in single steps. The most important new features are the ability to accurately separate exciton and biexciton dynamics and to measure correlations in the rate dispersion of exciton and biexciton relaxation. Related experimental results on exciton and biexciton dynamics in CdSe nanoparticles will be published in the near future. [22, 23]

The concept of MUPPETS is illustrated in Fig. 1. A total of six pulses are used: three (1–3) simultaneous pairs (a and b) separated by two times, τ_1 and τ_2. Each pair causes an incoherent transition, i.e., a transition from one quantum mechanical population to another. Any coherences are assumed to be quenched by rapid dephasing. The novel aspect of MUPPETS is that the correlated relaxation of the population during two time periods is measured. Ensemble averaging or relaxation of the molecule does not occur between these periods, so different processes are accessible than in experiments with only one relaxation time. Understanding the resulting multidimensional correlation functions when several population states are accessible is a primary aim of this paper.

The pulses in each pair come from different directions, so the populations consist of spatial gratings.[24-26] Detection is by diffraction of pulse 3a from the final population grating and heterodyning the diffracted light with pulse 3b. (Practical detection schemes also account for diffraction in the opposite direction.[15]) As Fig. 1(a) suggests, it is possible to arrange the phase-matching geometry such that diffraction only occurs from planes created by the combined action of all four excitation pulses. These more technical aspects of the experiment will not be treated here. It is only important to know that it is practical to isolate a signal that is confined to exactly one electric-field interaction with each of the six pulses.

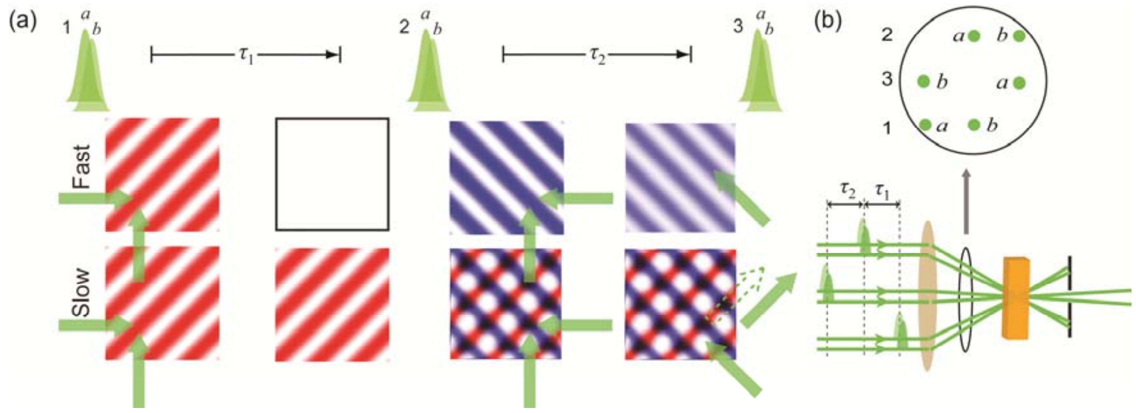

Figure 2.1. Schematic of the MUPPETS experiment. (a) The upper and lower panels represent rapidly and slowly relaxing subensembles within the sample. Two simultaneous pulses (1a and 1b) from different directions intersect in the sample to create a spatial grating of excited-state molecules (red). After a time τ_1, a second pair of pulses (2a and 2b) create a second grating of excited molecules (blue). The slow subensemble now contains vertical diffraction planes formed by regions that have interacted twice (black), once (red and blue) and never (white). After an additional time τ_2, pulse 3a is diffracted from these planes and is combined with pulse 3b for heterodyne detection. The diffraction isolates the signal unique to one interaction with the first excitation and one interaction with the second excitation. (b) An accurate representation of the pulse directions used in the experiment: tan–lens, orange–sample.

As with 1D kinetics, theoretical concepts transcend the various experimental implementations needed for different timescales and processes. In existing experiments, MUPPETS has focused on electronic-state relaxation on subnanosecond timescales. However, the theoretical ideas developed here are equally applicable to any timescale. With modest modification, they can also find application to other types of perturbation and other relaxation processes.

MUPPETS has strong parallels to multidimensional coherence spectroscopy (MDCS). MUPPETS measures multiple periods of incoherent evolution (kinetic rates), whereas MDCS measures multiple periods of coherent evolution (spectral frequencies). MDCS began with two-level systems, in which they give “echo” phenomena.[27, 28] These experiments separate homogeneous and inhomogeneous contributions to spectral linewidths, just as MUPPETS of two-level systems separates homogeneous and heterogeneous rate dispersion. When MDCS was extended to multilevel systems, it became various forms of spectral correlation spectroscopy, which reveal coupling between different spectral transitions.[29-33] MDCS is well established in NMR[29, 30] and, more recently, has been extended to electronic[31] and vibrational[32, 33] transitions. In the latter two forms, it has been especially valuable in excitonic systems,[34-40] where the transitions are strongly overlapped in one-dimensional (1D) spectra. By analogy, one anticipates that MUPPETS in multilevel systems will probe correlations in the relaxation of different transitions and will be especially relevant in excitonic systems, where spectral discrimination of different transitions can be difficult.

One goal of the paper is to clarify the meaning of the intertransition correlations that we anticipate. Another is to illustrate the interplay of the intertransition and intratransition contributions to the total experimental signal. To tackle these problems, we first develop simplified methods for calculating multidimensional incoherent signals in excitonic systems and then use them to calculate results for several simple, limiting models.

In two-level systems, it is common to reduce the dimensionality of the problem by changing the basis set. The total population is invariant, and only the dynamics of the population difference need to be calculate. The primary simplifications in the current calculations come from extending this idea to multilevel systems. A nonorthogonal coordinate system is required, but this feature is easily handled by the Hilbert-space formalism that we introduced previously.[16, 17] The primary new difficulty in multilevel systems is the possibility of cross-relaxation between basis states. Fortunately, this effect is minimized when higher excitons relax faster than lower excitons. This situation is common due to processes that are called exciton−exciton annihilation in molecular systems or Auger relaxation in semiconductors. Approximations for this case are found. Section 2.1 develops the general formalism, and then Sec. 2.2 looks in more detail at two-dimensional (2D) MUPPETS for several different energy-level schemes.

These results lead to several useful results that are explored in Sec. 2.3. Separating exciton and biexciton kinetics can be difficult when the spectral exciton shift is small. MUPPETS is a sensitive and robust method for separating exciton and biexciton dynamics that does not rely on spectral separation. It is also insensitive to the formation of photoproducts, which can complicate power-dependent measurements. In general, the level of coupling between zero-order chromophores needed to create an exciton for purposes of MUPPETS (an incoherent exciton) is much lower than that needed to create an exciton for purposes of coherent spectroscopy (a coherent exciton). Thus, MUPPETS can be useful for studying weakly coupled systems.

Example calculations are presented on four model systems with identical 1D kinetics in Sec. 2.4.3. These models mix homogeneous and heterogeneous exciton relaxation with biexcitons that are either correlated or uncorrelated with the exciton relaxation. Despite having identical one-dimensional (1D) kinetics and despite the overlap of intra- and inter-transition features, each model produces very different 2D results and would be readily distinguishable in a 2D MUPPETS experiment. Rate correlation between different transitions is shown to be analogous to homogeneous kinetics on a single transition. Correlation between exciton and biexciton relaxation is possible whether or not the individual transitions are homogeneous or heterogeneous. Intertransition rate correlations indicate a shared feature in the two relaxation mechanisms such as dependence on a common bath mode.

Real MUPPETS experiments detect not only the resonant signal due to the chromophore, but also see solvent heating due to chromophore relaxation.[18] These thermal effects are the multidimensional extension of thermal-grating spectroscopy.[24-26] They are both a complication to measuring the resonant signal and a potential route to measuring nonradiative relaxation between spectroscopically dark states. The theory needed to calculate thermal effects in multilevel MUPPETS experiments is developed in Sec. 2.5.

2.2 THEORY FOR MULTI-STATE SYSTEMS

The Hilbert-space pathway formalism for calculating multidimensional incoherent experiments has been discussed in detail previously.[16, 17, 21] In this formalism, as the number of states in the system increases, the number of pathways increases combinatorially. This section seeks to simplify such calculations. Section 2.1 summarizes previous Hilbert-space results in a convenient notation. Section 2.2 introduces a new basis set to simplify these calculations in a general multi-state system. Section 2.3 then specializes to excitonic systems, which will be the focus of the remainder of the paper.

2.2.1 Review of incoherent Hilbert-space calculations

The signal from an N-dimensional heterodyned experiment is the change in fluence of the (N+1)th (local oscillator) beam $\delta I_{N+1}(\Phi)$ relative to its total fluence I_{N+1}, as a function of the local-oscillator–probe phase difference Φ. This change can be expressed as an absorbance $A^{(N)}(\Phi;\ \tau_{N},\dots,\ \tau_1)$,

$$A^{(N)}(\Phi;\tau_N,\ldots,\tau_1)=(-1)^N\frac{\delta I_{N+1}(\Phi)}{I_{N+1}},\tag{1}$$

where τ_n is the time interval between pulses n and $n+1$. Fourier transforming the phase-dependence extracts a complex absorbance $A^{(N)}(\tau_N,\ldots,\tau_1)$, which obeys a generalized Beer's law,[18, 21]

$$A^{(N)}(\tau_N,\ldots,\tau_1)=(-1)^N\rho L\langle\boldsymbol{\sigma}_D\rangle^{\circ}.\tag{2}$$

This expression contains the detection cross-section operator $\boldsymbol{\sigma}_D$, the number density of solute molecules ρ, and the length of the sample L.

The expectation value of $\boldsymbol{\sigma}_D$ is calculated as a matrix element in the incoherent Hilbert space,

$$\langle\boldsymbol{\sigma}_D\rangle^{\circ}=[\boldsymbol{I}\,|\,\boldsymbol{\sigma}_D\,|\,\boldsymbol{f}(\tau_N,\ldots,\tau_1)]^{\circ},\tag{3}$$

where $[I|$ is the identity state [see Eq. (17)] and $|f]$ is the final state of the system at the time of detection. The degree sign indicates that the calculations are done without the phase factors for the excitation fields.[18] The phase convention for the complex absorbance is the same as for the complex cross-section: real parts correspond to absorption; imaginary parts correspond to index-of-refraction. The final state $|f]$ is obtained from the initial, equilibrium state $|eq]$ by successive operators $\mathbf{T}_n$, representing optical transitions due to the nth excitation, and $\mathbf{G}(t_n, t_{n-1})$, representing evolution between times t_{n-1} and t_n,

$$|\,\boldsymbol{f}(\tau_N,\ldots,\tau_1)]^{\circ}=\mathbf{G}(t_N,t_{N-1})\mathbf{T}_N^{\circ}\ldots\mathbf{G}(t_1,t_0)\mathbf{T}_1^{\circ}\,|\,\boldsymbol{eq}].\tag{4}$$

Throughout the paper, absolute times will be denoted t_n, and time intervals will be given by

$$\tau_n = t_n - t_{n-1} \,. \tag{5}$$

The equation of motion for an arbitrary state $|P]$ contains the rate operator $\mathbf{R}(t)$:

$$\frac{d}{dt} | P] = -\mathbf{R}(t) \, | P] \,. \tag{6}$$

For nonexponential relaxations, the rates are time dependent. The Green's operator $\mathbf{G}(t_n, t_{n-1})$ is then nonstationary:

$$\mathbf{G}(t_2, t_1) = \exp_+ \left(-\int_{t_1}^{t_2} \mathbf{R}(t) dt \right), \tag{7}$$

where the exponential is time ordered.[41]

The optical-transition operator $\mathbf{T}_n^\circ$ is given by

$$\mathbf{T}_n^\circ = \sum_{i,j \in \{a,b\}} I_{n,ij} \boldsymbol{\sigma}_T \mathbf{K}_{n,ij} \left(\vec{\mathbf{M}} \bullet \vec{\Pi}_{n,ij} \right). \tag{8}$$

The nth excitation consists of two pulses labeled a and b (see Fig. 1), and in Eq. (8), the sum runs over the four permutations of these pulses. The effective fluence of the pair $I_{n,ij}$ is the geometric mean of the fluences of the two pulses, $I_{n,i}$ and $I_{n,j}$: $I_{n,ij} = \left(I_{n,i} I_{n,j} \right)^{1/2}$.

The transition cross-section operator $\boldsymbol{\sigma}_T$ is constructed from the absorption cross-sections of the electronic transitions of the system. Unlike the detection cross-section $\boldsymbol{\sigma}_D$, which is complex, $\boldsymbol{\sigma}_T$ has only real elements. The dipole-moment tensor $\vec{\mathbf{M}}$ and the polarization tensors $\vec{\Pi}_{n,ij}$ are required to calculate the effects of chromophore rotation, but will be neglected in this paper. The phase-matching conditions are generated by the grating-vector operator $\mathbf{K}_{n,ij}$. We assume that one combination of pulses is perfectly phase matched, and all others are poorly phase matched.

With these assumptions, the equation for the signal reduces to

$$\begin{aligned} A^{(N)}(\tau_N,\ldots,\tau_1) = (-1)^N \rho L I^{(N)} [\boldsymbol{I} \,|\, \boldsymbol{\sigma}_D \mathbf{G}(t_N,t_{N-1})\ldots \\ \times \boldsymbol{\sigma}_T \mathbf{G}(t_1,t_0) \boldsymbol{\sigma}_T \,|\, \boldsymbol{eq}] \end{aligned} \quad , \tag{9}$$

with

$$I^{(N)} = I_{N,ab} \cdots I_{1,ab} \tag{10}$$

representing the total excitation fluence from N pulse pairs. In the case where every pulse has the same fluence I, $I^{(N)} = I^N$. The next step is to introduce complete sets of states between each pair of operators in Eq. (9). The results are more compact if we adopt the notation

$$[\boldsymbol{n} \,|\, \mathbf{O} \,|\, \boldsymbol{m}] = O_n^m \tag{11}$$

for the matrix element of an operator **O** between states $[n|$ and $|m]$. Assuming summation over repeated indices, Eq. (9) reduces to

$$\begin{aligned} \frac{A^{(N)}(\tau_N,\ldots,\tau_1)}{\rho L I^{(N)}} = (-1)^N \Big\langle (\sigma_D)_I^n \, G_n^m(t_N,t_{N-1})\ldots \\ \times (\sigma_T)_k^j \, G_j^i(t_1,t_0) (\sigma_T)_i^{eq} \Big\rangle \end{aligned} \quad . \tag{12}$$

Each term in the implied sum represents one Hilbert-space pathway. This sum is calculated for a single chromophore before averaging over the ensemble, as indicated by the angular brackets.

If the optical cross-sections are independent of time, the time dependence and relative weight of each pathway can be separated:

$$\frac{A^{(N)}(\tau_N,\ldots,\tau_1)}{\rho L I^{(N)}} = \left(-1\right)^N B^{n,\ldots,j,eq}_{I,\ldots,k,i}\, C^{m,\ldots,i}_{n,\ldots,j}(\tau_N,\ldots,\tau_1)\,. \tag{13}$$

Each pathway is defined by the set of intermediate states $\{i, \ldots, n\}$. The dynamics associated with a pathway are given by the correlation-function matrix

$$C^{m,\ldots,i}_{n,\ldots,j}(\tau_N,\ldots,\tau_1) = \left\langle G^m_n(t_N,t_{N-1})\ldots G^i_j(t_1,t_0)\right\rangle. \tag{14}$$

Each element of this $2N$-dimensional matrix is an N-time-interval correlation function. Each correlation function is the ensemble average of N time-evolution operators. The relative weight of each pathway is given by

$$B^{n,l,\ldots,eq}_{I,m,\ldots,i} = \left(\sigma_D\right)^n_I \cdots \left(\sigma_T\right)^j_k \left(\sigma_T\right)^{eq}_i\,. \tag{15}$$

Because two of its indices are fixed, this matrix also has $2N$ dimensions. Each element gives the total cross-section of the corresponding element of the correlation-function matrix. The scalar product of these two matrices in Eq. (13) sums the correlation functions from all the pathways with their appropriate cross sections.

2.2.2 Basis set to reduce the dimensionality of the problem

Here, we consider the general problem of a good basis set for pathway calculations in a system with $\mathcal{N}$ optical levels, $\{|0], |1], \ldots, |\mathcal{N}-1]\}$. It is desirable to have the initial, equilibrium state $|eq]$ as one member of the basis set. If the state spacing is large, only the lowest state is occupied in equilibrium: $|0] = |eq]$. It is also desirable to have the identity state $[I|$ as a member of the basis set. Thus, in the new, primed basis set, $\{|0'], |1'], \ldots, |\mathcal{N}-1']\}$, we require

$$|0'] = |eq] = |0] \tag{16}$$

and

$$[0'| = [\boldsymbol{I}| = \sum_{n=0}^{\mathcal{N}-1} [\boldsymbol{n}| \, . \tag{17}$$

With these conditions, all pathways begin with $|0']$ and end with $[0'|$ [see Eqs. (9) and (12)].

An orthogonal basis set cannot satisfy both Eqs. (16) and (17). However, in a nonorthogonal basis, bras and kets need not be identical: they are described by different, dual basis sets.[42] In such a nonorthogonal system, the nonzero kets must be orthogonal to $[0'|$:

$$[0' | \boldsymbol{n}'] = [I | \boldsymbol{n}'] = \delta_{0,n} \, . \tag{18}$$

Because the identity state measures the total population of a state,[16] Eq. (18) means that the nonzero primed kets do not have any net population: they consist only of population differences. As a result, the rate operator $\mathbf{R}(t)$ cannot connect the zero and nonzero kets without changing the total population of the system. These two sets of states, zero prime and nonzero prime, are the irreducible sets resulting from the law of population conservation. In addition, $|0'] = |eq]$ cannot decay; it is unaffected by $\mathbf{R}(t)$. Thus, it is possible to reduce the dimensionality of the rate matrix $R^{i'}_{j'}(t)$ by eliminating its 0′ row and column.

The exact form of the nonzero states has not been specified. We choose the first excited state [1′| so it is the only nonzero transition out of |0′]:

$$[\boldsymbol{n}' \,|\, \boldsymbol{\sigma}_T \,|\, 0'] = \delta_{n'1'} \left(\sigma_T\right)_{1'}^{0'} . \tag{19}$$

The transition cross-section acts on a general state |*P*] in a perturbative fashion:[17]

$$\left(\mathbf{1} + \lambda \boldsymbol{\sigma}_T\right) | \boldsymbol{P}] = | \boldsymbol{P}] + \lambda \boldsymbol{\sigma}_T \,|\, \boldsymbol{P}] . \tag{20}$$

By the conservation of population, $\boldsymbol{\sigma}_T$ acting on any state can only create a new state with no population, that is, a superposition of nonzero primed states. Thus,

$$[0' \,|\, \boldsymbol{\sigma}_T \,|\, \boldsymbol{n}'] = 0 . \tag{21}$$

With Eqs. (19) and (21), the transition cross-section matrix $\left(\sigma_T\right)_j^i$ can also be reduced in dimension by eliminating its 0′ row and column.

This procedure drops one nonzero element $\left(\sigma_T\right)_{1'}^{0'}$ which occurs on the first step in every pathway. The effect of this element will be included in a new detection vector [σ_D|, which is defined by

$$[\sigma_D | = \frac{\left(\sigma_T\right)_{1'}^{0'}}{\mathrm{Re}\left(\sigma_D\right)_{0'}^{0'}} [0' \,|\, \boldsymbol{\sigma}_D . \tag{22}$$

Because all pathways end on [0′|, the detection matrix and final state can be replaced by this vector. Because there are no transitions into |0′], the first element of element of the detection matrix only occurs in static (*N* = 0) spectroscopy:

$$A^{(0)} = \rho L \left(\sigma_D\right)_{0'}^{0'} . \tag{23}$$

For all higher order measurements, the $n = 0$ element of $(\sigma_D)^{n'}$ can be dropped, and the detection vector can be reduced in dimension. The term $\mathrm{Re}\left(\sigma_D\right)_{0'}^{0'}$ is included in the definition of $[\sigma_D|$ for convenience: Using Eq. (23), the Nth-order absorbance will scale explicitly with the static absorbance $A'^{(0)}$.

Equation (13) can now be re-expressed as

$$\frac{A^{(N)}(\tau_N,\ldots,\tau_1)}{A'^{(0)}} = I^{(N)} \sigma^{n',\ldots,\ l',j'}_{\quad m',\ldots,k'}\, C^{m',\ldots,k',1'}_{n',\ \ldots,l',\ j'}(\tau_N,\ldots,\tau_1)\,, \tag{24}$$

for $N \neq 0$. The total cross-section,

$$\sigma^{n',\ldots,\ l',j'}_{\quad m',\ldots,k'} = \left(-1\right)^N \left(\sigma_D\right)^{n'} \left(\sigma_T\right)^{l'}_{m'} \cdots \left(\sigma_T\right)^{j'}_{k'}, \tag{25}$$

gives the relative weight of each pathway, but is a lower dimensional matrix than $B^{n,\ldots,j,eq}_{l,\ldots,k,i}$ [Eq. (15)]. It contains N cross-sections to match the N fluence factors in $I^{(N)}$. The correlation function is also simplified relative to Eq. (14), because its first index is now fixed. Equation (24) generalizes a familiar expression for the fractional population change in a pump–probe experiment,

$$\frac{\Delta A'(\tau)}{A'_0} = \frac{\Delta\rho(\tau)}{\rho_0} = -I\sigma C(\tau)\,. \tag{26}$$

The indices in Eq. (24) only run over nonzero values. Thus, in the primed basis set, the entire calculation is restricted to nonzero intermediate states, and the problem is reduced by one dimension. The reduction is possible because of the restrictions implied by population conservation.

For a two-level system, Eqs. (16) and (18) completely determine the primed basis set,

$$
\begin{aligned}
&|\,0'] = |\,0] \\
&|\,1'] = \frac{1}{\sqrt{2}}\big(|\,1] - |\,0]\big),
\end{aligned}
\tag{27}
$$

and its dual basis set,

$$
\begin{aligned}
&[0'\,| = [1\,| + [0\,| \\
&[1'\,| = \sqrt{2}[1\,| \quad .
\end{aligned}
\tag{28}
$$

It is also possible to include population conservation in a two-level system by using an orthogonal basis set.[17] Either approach is viable, but the current one generalizes to multilevel systems.

2.2.3 Application to excitonic systems

For more than two states, Eqs. (16) and (18) do not completely define the higher basis states. Choices can be made to further simplify the transition and rate matrices, but more detailed knowledge of the structure of these matrices is needed. We specialize to excitonic systems, which are defined as a set of equally spaced states or groups of nearly degenerate states that undergo optical transitions and relaxation in increments of one "quantum" at a time. The transition and rate matrices of an excitonic system are simplified if the nonzero primed basis kets are chosen to be differences of neighboring states,

$$
|\,\boldsymbol{n}'] = \frac{1}{\sqrt{2}}\big(|\,\boldsymbol{n}] - |\,\boldsymbol{n}-1]\big), \quad n \geq 1\,,
\tag{29}
$$

with the dual states

$$
[\boldsymbol{n}'\,| = \sqrt{2}\sum\nolimits_{i=n}^{\mathcal{N}} [\boldsymbol{i}\,|, \quad n \geq 1\,.
\tag{30}
$$

The remainder of the paper focuses on 1D and 2D experiments. These experiments cannot access states higher than |3], so four-level schemes will be sufficient. The standard basis set for such schemes is {|3], |2], |1], |0]} (triexciton, biexciton, exciton and ground states, respectively). The same rate matrix applies for all schemes,

$$R^{i}_{j}(t) = \begin{pmatrix} k_t(t) & 0 & 0 & 0 \\ -k_t(t) & k_b(t) & 0 & 0 \\ 0 & -k_b(t) & k_e(t) & 0 \\ 0 & 0 & -k_e(t) & 0 \end{pmatrix}. \tag{31}$$

where $k_t(t)$ is the triexciton-to-biexciton rate, $k_b(t)$ is the biexciton-to-exciton rate, and $k_e(t)$ is the exciton-to-ground-state rate. When transformed to the primed basis set, the rate matrix becomes

$$R^{i'}_{j'}(t) = \begin{pmatrix} k_t(t) & 0 & 0 & 0 \\ -k_b(t) & k_b(t) & 0 & 0 \\ 0 & -k_e(t) & k_e(t) & 0 \\ 0 & 0 & 0 & 0 \end{pmatrix}, \tag{32}$$

which can be reduced in dimensionality to

$$R^{i'}_{j'}(t) = \begin{pmatrix} k_t(t) & 0 & 0 \\ -k_b(t) & k_b(t) & 0 \\ 0 & -k_e(t) & k_e(t) \end{pmatrix}. \tag{33}$$

In addition, the total signal given by Eq. (24) simplifies because the first excited state defined by Eq. (19) is also the lowest state in the relaxation scheme given by Eq. (33), that is, $j = 1'$:

$$\frac{A^{(N)}(\tau_N,\ldots,\tau_1)}{A'^{(0)}} = I^{(N)} \sigma^{n',\ldots,\; l',1'}_{m',\ldots,k'} \, C^{m',\ldots,k',1'}_{n',\,\ldots,l',\,1'}(\tau_N,\ldots,\tau_1)\,, \tag{34}$$

Thus, the signal is calculated as a product of two 2(N−1)-dimensional matrices, one dimension lower than in Eq. (13).

Off-diagonal elements in the rate matrix add complexity to the calculations. It is not generally possible to diagonalize the rate matrix with any coordinate transformation. However, in the primed basis set, the off-diagonal terms becomes small if each higher exciton relaxes rapidly compared to lower excitons. As discussed in Sec. 2.4.2 below, this limit can be regarded as one of strong incoherent coupling. In the current example,

$$R_{j'}^{i'}(t) \xrightarrow{k_t \gg k_b \gg k_e} \begin{pmatrix} k_t(t) & 0 & 0 \\ 0 & k_b(t) & 0 \\ 0 & 0 & k_e(t) \end{pmatrix}. \qquad (35)$$

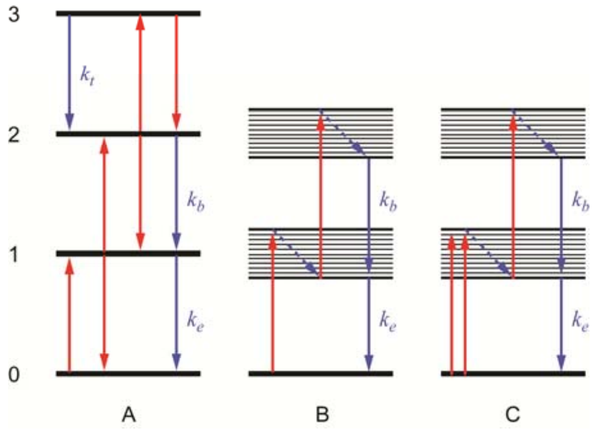

Figure 2.2. Three energy-level schemes for an excitonic system. Red arrows are allowed optical transitions with each arrow indicating a factor of σ in cross-section. Blue arrows indicate nonradiative transitions; dashed arrows are fast relaxations.

The transition and detection cross-section matrices depend on the spectroscopic details of the system. Three examples are shown in Fig. 2. They have been chosen to illustrate important limiting behaviors in the final signal. Scheme A represents an exciton consisting of many coupled chromophores ($M \to \infty$, see Sec. 2.4.2). The ground-to-exciton transition has the same cross-section as the exciton-to-biexciton and biexciton-to-triexciton transitions: $\sigma_{01} = \sigma_{12} = \sigma_{23} = \sigma$. In addition, the downward transitions have the same cross-section as the upward transitions: $\sigma_{01} = \sigma_{10}$, $\sigma_{12} = \sigma_{21}$ and $\sigma_{23} = \sigma_{32}$.

Alternatively, the exciton levels may not be eigenstates. They may have internal structure or dynamics within a band of nearly degenerate eigenstates. Scheme B is an example. Absorption to a bright state is followed by rapid relaxation to a state with zero emission cross-section: $\sigma_{10} = \sigma_{21} = 0$. The ground-to-exciton and exciton-to-biexciton transitions still have the same strength: $\sigma_{01} = \sigma_{12} = \sigma$. No triexciton state is included.

Scheme C is similar to scheme B, in that it has no triexciton and no emission ($\sigma_{10} = \sigma_{21} = 0$). However, it consists of few coupled chromophores, so the exciton-to-biexciton transition has a lower cross-section than the ground-to-exciton transition. We choose $\sigma_{01} = 2\sigma_{12} = 2\sigma$ ($M = 2$, see Sec. 2.4.2). CdSe nanoparticles with band-edge excitation are a real system approximated by model C.[22, 23, 43]

For scheme A in the standard basis set, the transition matrix is

$$\left(\sigma_T\right)^i_j = \sigma' \begin{pmatrix} -1 & 1 & 0 & 0 \\ 1 & -2 & 1 & 0 \\ 0 & 1 & -2 & 1 \\ 0 & 0 & 1 & -1 \end{pmatrix}, \tag{36}$$

and the detection matrix is

$$\left(\sigma_D\right)^j_i = \frac{\sigma}{2} \begin{pmatrix} -1 & 1 & 0 & 0 \\ -1 & 0 & 1 & 0 \\ 0 & -1 & 0 & 1 \\ 0 & 0 & -1 & 1 \end{pmatrix}, \tag{37}$$

where the prime indicates the real part of the complex cross-section. In the primed basis set, these matrices become

$$\left(\sigma_T\right)^{i'}_{j'} = \sigma' \begin{pmatrix} -2 & 1 & 0 & 0 \\ 1 & -2 & 1 & 0 \\ 0 & 1 & -2 & \sqrt{2} \\ 0 & 0 & 0 & 0 \end{pmatrix} \tag{38}$$

and

$$\left(\sigma_D\right)^{i'}_{j'} = \frac{\sigma}{2} \begin{pmatrix} -2 & 1 & 0 & 0 \\ -3 & 0 & 1 & 0 \\ -2 & -1 & 0 & \sqrt{2} \\ -\sqrt{2} & 0 & -\sqrt{2} & 2 \end{pmatrix}. \tag{39}$$

Reducing the dimensionality of the matrices yields

$$\left(\sigma_T\right)^{i'}_{j'} = \sigma' \begin{pmatrix} -2 & 1 & 0 \\ 1 & -2 & 1 \\ 0 & 1 & -2 \end{pmatrix}. \tag{40}$$

and

$$\left(\sigma_D\right)^{i'} = \sigma\begin{pmatrix} -1 & 0 & -1 \end{pmatrix}. \tag{41}$$

To evaluate the total signal for scheme A, Eqs. (40) and (41) are inserted into Eq. (25) and evaluated by standard matrix methods to yield the relative cross-section of each pathway $\sigma^{n',\ldots,\ l',1'}_{\quad m',\ldots,k'}$. The correlation function for each pathway $C^{m',\ldots,k',1'}_{n',\ \ldots,l',\ 1'}(\tau_N,\ldots,\tau_1)$ is evaluated by putting Eq. (33) into Eqs. (7) and (14). These components are put into Eq. (34) to give the experimental signal. Examples of this procedure are given in the next section.

2.3 PATHWAY CALCULATIONS IN EXCITONIC SYSTEMS

2.3.1 Cross-sections

In the standard basis set, Eq. (13) yields three pathways with nonzero amplitude for 1D experiments and 16 pathways for 2D experiments. In the primed basis set using Eq. (34), the number of pathways is reduced to one for 1D experiments and three for 2D experiments. These pathways are shown on the right-hand side of Fig. 3. Each pathway is represented as a series of transformation from the initial state on the right to the final state on the left. Each transformation is represented as an arrow and contributes a matrix element of the operator governing the transformation, which is shown below the pathways. The final state of each pathway is detected by forming the product with the detection vector $[\sigma_D|$. The strong selection rules in the primed basis set allow the one to quickly enumerate the pathways with nonzero amplitude on such diagrams.

The correlation function corresponding to each pathway is shown on the left-hand side of Fig. 3. It is formed from the matrix elements of the time-evolution operator of the corresponding pathway through Eq. (14). The steps in the pathways are labeled above the solid line with the indices used in our equations.

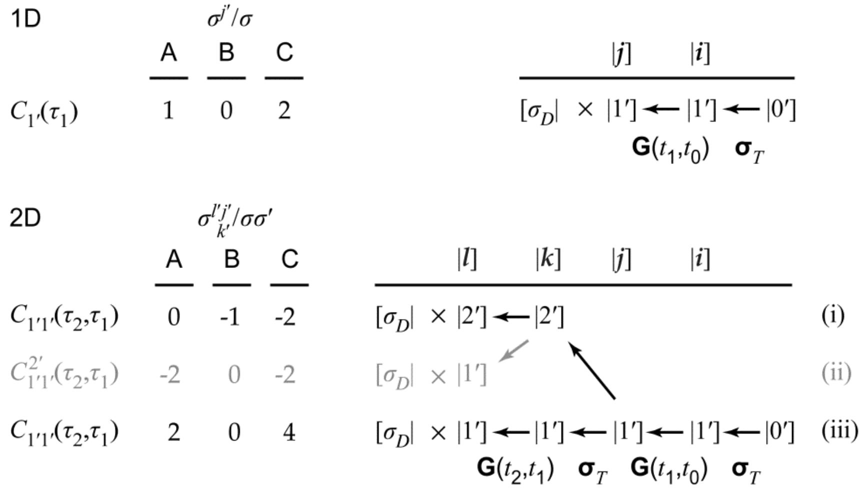

Figure 2.3. Pathways for the calculation of one-dimensional (1D) and two-dimensional (2D) signals. The right-hand side shows the allowed pathways between states $|n']$ in the primed basis set. The operators responsible for each transition are given below the arrows: **G**, the time-evolution operator, and $\boldsymbol{\sigma}_T$, the optical transition operator. The indices corresponding to each level in the pathway are indicated above the solid line. The final state in each pathway is detected by taking the product with the detection vector $[\sigma_D|$. The total cross-section for each pathway is given in the center of the figure for each of the energy-level schemes shown in Fig. 2. The correlation function for each pathway is given on the left. Pathways (i) and (iii) have only diagonal relaxation and dominate when the biexciton decay is faster than the exciton decay. Pathway (ii) (gray) involves cross-relaxation and is a minor contribution.

In the case where biexciton relaxation is faster than exciton relaxation, pathway (ii), which is in gray, has only a small contribution. That pathway will be discussed in Sec. 2.3.3. For now, we only consider the two dominant 2D pathways. Note that the triexciton state contributes to the detection cross-section in scheme A, but $|3']$ cannot occur as an intermediate state in a 2D experiment.

The total cross section for each pathway is calculated from the matrix elements of the cross-section operators, $\boldsymbol{\sigma}_T$ and $\boldsymbol{\sigma}_D$, according to Eq. (34). The exact cross-section for each pathway and, in particular, the relative contributions of exciton and biexciton dynamics, depend on the details of the state scheme. Results for the three schemes of Fig. 2 are shown in the center of Fig. 3. Scheme A is a limiting case (see Sec. 2.4.2

below) where excitons are detectable and biexcitons are not. The only pathway involving biexciton dynamics, pathway (i), has a cross-section of zero. Scheme B is in the opposite limit: biexcitons are directly detectable and excitons are not. Scheme B gives no signal in a 1D experiment, and 2D pathway (iii) has a cross-section of zero. However, 2D pathway (i) has a nonzero cross-section and can be measured in Scheme B. Information on both exciton and biexciton dynamics are available from this pathway.

Scheme C is an intermediate case where pathways ending with either excitons or biexcitons contribute to the signal. The notable feature is that the two pathways (i) and (iii) have opposite signs. Generally, the biexciton relaxes faster than the exciton, and the signal will initially rise as the negative biexciton signal decays. This feature allows 2D MUPPETS to cleanly separate exciton and biexciton dynamics, as will be illustrated in Sec. 2.4.1.

To summarize, the relative contributions of exciton and biexciton dynamics to a 2D experiment vary with the transition cross-sections of the system of interest. These cross-sections determine both the relative signs and magnitudes of the correlation functions that are measured, and thus, the type of dynamical information that is available.

2.3.2 Diagonal correlation functions

The reduction in the number of pathways in the primed basis set not only simplifies the calculation of amplitudes; it also reduces the number of correlation functions to a minimum. Figure 3 shows that a 1D experiment is described by a single correlation function $C_{1'}^{1'}(\tau_1)$. This correlation function is diagonal in the sense that in one time period it only measures survival of one basis state. In this case, the notation can be simplified: $C_i^i(\tau_1) = C_i(\tau_1)$. This type of correlation function is normalized to one at the time origin.

Using Eqs. (7), (14) and (33), the exciton decay measured in a 1D experiment is given by

$$\begin{aligned} C_{1'}(\tau_1) &= \left\langle G_{1'}^{1'}(t_1, t_0) \right\rangle \\ &= \left\langle \exp\left(-\int_{t_0}^{t_1} k_e(t)dt \right) \right\rangle . \end{aligned} \tag{42}$$

A similar correlation function,

$$\begin{aligned} C_{2'}(\tau_1) &= \left\langle G_{2'}^{2'}(t_1, t_0) \right\rangle \\ &= \left\langle \exp\left(-\int_{t_0}^{t_1} k_b(t)dt \right) \right\rangle , \end{aligned} \tag{43}$$

defines the biexciton decay, but it cannot be measured in a 1D experiment.

The 2D signals are dominated by diagonal correlation functions. The exciton–exciton correlation function,

$$\begin{aligned} C_{1'1'}(\tau_2, \tau_1) &= \left\langle G_{1'}^{1'}(t_2, t_1) G_{1'}^{1'}(t_1, t_0) \right\rangle \\ &= \left\langle \exp\left(-\int_{t_1}^{t_2} k_e(t)dt - \int_{t_0}^{t_1} k_e(t)dt \right) \right\rangle , \end{aligned} \tag{44}$$

occurs in pathway (iii) of Fig. 3. It is essentially similar to the 2D correlation function previously studied in two-level systems.[14, 19, 21] If the decay is nonexponential due to homogeneous causes, the 2D correlation function is the product of 1D correlation functions,

$$C_{1'1'}(\tau_2, \tau_1) = C_{1'}(\tau_2) C_{1'}(\tau_1) . \tag{45}$$

If the decay is heterogeneous, the 2D correlation function is equal to the 1D correlation function of the sum of the time variables,

$$C_{1'1'}(\tau_2, \tau_1) = C_{1'}(\tau_2 + \tau_1) \, . \tag{46}$$

Thus, with 2D MUPPETS in an excitonic system, it is possible to distinguish homogeneous and heterogeneous mechanisms of rate dispersion of the exciton decay, just as it is in a two-level system.

A new feature of MUPPETS in multilevel systems is the possibility of cross-correlations between different relaxations. For example, pathway (i) in Fig. 3 has an exciton–biexciton correlation function,

$$\begin{aligned} C_{2'1'}(\tau_2, \tau_1) &= \left\langle G_{2'}^{2'}(t_2, t_1) G_{1'}^{1'}(t_1, t_0) \right\rangle \\ &= \left\langle \exp\left(-\int_{t_1}^{t_2} k_b(t)dt - \int_{t_0}^{t_1} k_e(t)dt \right) \right\rangle . \end{aligned} \tag{47}$$

Although two transitions are involved, the correlation is still diagonal during each time interval. When $\tau_1 = 0$, this function gives access to the biexciton decay [Eq. (43)],

$$C_{2'1'}(\tau_2, 0) = C_{2'}(\tau_2) \, . \tag{48}$$

More generally, $C_{2'1'}(\tau_2, \tau_1)$ is sensitive to correlations between exciton and biexciton dynamics. These correlations are an important new feature in multilevel MUPPETS and are illustrated with examples in Sec. 2.4.2.

2.3.3 Off-diagonal correlation functions

In addition to the diagonal correlation functions just discussed, multilevel systems also have correlations involving relaxation between basis states during one of the time periods. These correlation functions involve off-diagonal elements of the rate matrix. For example, pathway (ii) in Fig. 2.3 has the correlation function

$$C_{1'1'}^{2'}(\tau_2,\tau_1) = \left\langle G_{1'}^{2'}(t_2,t_1) G_{1'}^{1'}(t_1,t_0) \right\rangle, \tag{49}$$

which involves relaxation from $|2']$ to $|1']$ during τ_2. The Appendix [see Eq. (A214)] shows that the off-diagonal time evolution can be calculated exactly once a dynamic model for the diagonal elements is specified:

$$G_{1'}^{2'}(t_2,t_1) = \int_{t_1}^{t_2} G_{1'}^{1'}(t_2,t') k_{1'}(t') G_{2'}^{2'}(t',t_1) dt' . \tag{50}$$

However, it is difficult to make general statements about the full correlation function from this exact expression.

Fortunately, the primed basis set makes the cross relaxation small when biexciton relaxation is faster than exciton relaxation. In this case, the relaxation of the standard basis state $|2]$ is biphasic: first $|2]$ decays to $|1]$, and then $|1]$ decays to $|0]$. In the primed basis, this decay is represented by a sum of $G_{2'}^{2'}(t_2,t_1)$ and $G_{1'}^{1'}(t_2,t_1)$. However, this sum contains a small error: the decay of $|1]$ does not start immediately as it does in $G_{1'}^{1'}(t_2,t_1)$; the start of its decay is delayed by the time needed for the biexciton to decay. This correction is isolated as the off-diagonal time evolution $G_{1'}^{2'}(t_2,t_1)$. If the decay of the exciton during the biexciton lifetime is small, the correction is small. The Appendix shows that in this limit, the off-diagonal time evolution can be approximated by

$$G_{1'}^{2'}(t_2,t_1) = G_{2'}^{2'}(t_2,t_1)\left(1 - G_{1'}^{1'}(t_2,t_1)\right). \tag{51}$$

The cross-relaxation correlation function cannot be calculated until the correlation between exciton and biexciton dynamics are specified. However, its properties can be illustrated with the case of uncorrelated dynamics. In that case, the 1D and 2D correlation cross-relaxation correlation functions can be expressed in terms of the diagonal correlation functions,

$$\begin{aligned} C_{1'}^{2'}(\tau_1) &= \left\langle G_{1'}^{2'}(t_2,t_1)\right\rangle \\ &= C_{2'}(\tau_1)\left(1 - C_{1'}(\tau_1)\right), \end{aligned} \tag{52}$$

and

$$C_{1'1'}^{2'}(\tau_2,\tau_1) = C_{2'}(\tau_2)\left(C_{1'}(\tau_1) - C_{1'1'}(\tau_1,\tau_2)\right). \tag{53}$$

Cross-relaxations are not normalizable: they are zero at the time origin. Their contribution to the signal must be judged not by their cross-section, as given in Fig. 3, but by their maximum size. The 2D function $C_{1'1'}^{2'}(\tau_2,\tau_1)$ is zero whenever $\tau_2 = 0$. Its maximum lies along $\tau_1 = 0$, where it is equal to the 1D cross-relaxation function,

$$C_{1'1'}^{2'}(\tau_2,0) = C_{1'}^{2'}(\tau_2). \tag{54}$$

It rises slowly in τ_2 with the exciton decay $C_{1'}(\tau_2)$, but is cut-off by the rapid biexciton decay $C_{2'}(\tau_2)$ [see Eq. (52) and Fig. 4(a)]. If the dynamics can be characterized by average rate constants, the maximum value of $C_{1'}^{2'}(\tau_2)$ is approximately k_e/k_b.

2.4 EXAMPLES OF NEW EFFECTS

2.4.1 Separating exciton and biexciton dynamics

This section will present calculations of 2D-MUPPETS results for several simple models of the dynamics. All the models are based on state scheme C in Fig. 2, where all pathways are active. The 1D correlation functions for all the examples will be the same:

$$C_{1'}(\tau_1) = \exp\left[-\left(\tau_1/\tau_0\right)^{1/2}\right] \tag{55}$$

for the exciton and

$$C_{2'}(\tau_1) = \exp\left[-\left(10\tau_1/\tau_0\right)^{1/2}\right] \tag{56}$$

for the biexciton. These two decays are similar,

$$C_{2'}(\tau_1) = C_{1'}(c\tau_1)\,, \tag{57}$$

with the biexciton decaying ten times faster ($c = 10$) than the exciton.

The decays are stretched exponentials in time and are shown in Fig. 4(a). The cross relaxation $C_{1'}^{2'}(\tau_1)$ in the uncorrelated limit [Eq. (52)] is also shown in Fig. 4(a). As expected, the large difference between exciton and biexciton decay times makes this term small.

In addition to the time-domain decays, it is useful to look at rate spectra. The rate spectrum $\hat{C}(y)$ of a correlation function $C(\tau)$ is defined implicitly by

$$C(\tau) = \int_{-\infty}^{\infty} \hat{C}(y) \exp\left(-\tau e^{y} / \tau_0\right) dy\,. \tag{58}$$

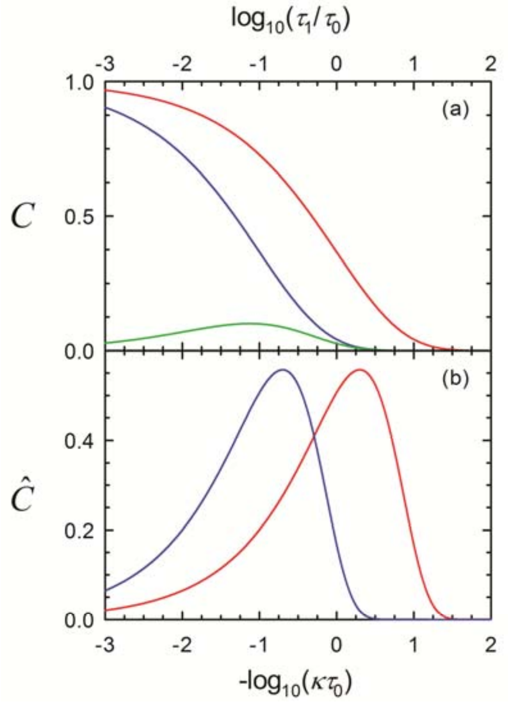

Figure 2.4. The 1D kinetics used in the example calculations (Figs. 5–7), which are identical for all the models. (a) Time decays: exciton decay $C_{1'}(\tau)$ [upper, red curve, Eq. (55)], biexciton decay $C_{2'}(\tau)$ [middle, blue curve, Eq. (56)], and cross-relaxation $C_{1'}^{2'}(\tau_1)$ [lowest, green curve, Eq. (52)]. (b) Rate spectra: Exciton spectrum $\hat{C}_{1'}(y)$ (rightmost, red curve) and biexciton spectrum $\hat{C}_{2'}(y)$ (leftmost, blue curve)with $y = \ln(\kappa\tau_0)$.

The rate spectrum is essentially the inverse Laplace transform of the time decay expressed on a logarithmic scale, $y = \ln(\kappa\tau_0)$, where κ is the Laplace rate. More detail on the properties and calculation of rate spectra can be found in Ref. 2. The rate spectrum $\hat{C}_{1'}(y)$ of the stretched exponential in Eq. (55) is shown in Fig. 4(b). Applying the transform in Eq. (58) twice, a 2D time function $C(\tau_2, \tau_1)$ can be expressed as a rate-correlation spectrum $\hat{C}(y_2, y_1)$.

The experimental signal in a 1D experiment is directly related to the 1D exciton correlation function,

$$A^{(1)}(\tau_1) = 2\sigma I^{(1)} A'^{(0)} C_{1'}(\tau_1) \,. \tag{59}$$

The other 1D correlation functions cannot be observed in a 1D experiment, but they can be accessed in a 2D experiment. The full 2D signal is

$$\begin{aligned} A^{(2)}(\tau_2,\tau_1) = 2\sigma\sigma' I^{(2)} A'^{(0)} \Big(& C_{1'1'}(\tau_2,\tau_1) - \tfrac{1}{2} C_{2'1'}(\tau_2,\tau_1) \\ & - \tfrac{1}{2} C_{1'1'}^{2'}(\tau_2,\tau_1) \Big) \,. \end{aligned} \tag{60}$$

Along the $\tau_2 = 0$ axis, the 2D experiment simply duplicates the information in the 1D experiment:

$$A^{(2)}(0,\tau_1) = \sigma\sigma' I^{(2)} A'^{(0)} C_{1'}(\tau_1) = \tfrac{1}{2} \sigma' I_2 A^{(1)}(\tau_1) \,. \tag{61}$$

Along the $\tau_1 = 0$ axis, the 2D absorbance reduces to a sum of the three 1D correlation functions,

$$A^{(2)}(\tau_2,0) = 2\sigma\sigma' I^{(2)} A'^{(0)} \Big(C_{1'}(\tau_2) - \tfrac{1}{2} C_{2'}(\tau_2) - \tfrac{1}{2} C_{2'}^{1'}(\tau_2) \Big) . \tag{62}$$

These two cuts through the 2D signal are shown in Fig. 5 as solid curves. Because they are related to 1D correlation functions, they contain no new information on rate heterogeneity or correlation. Nonetheless, they contain new information on the biexciton decay that is not available from 1D measurements.

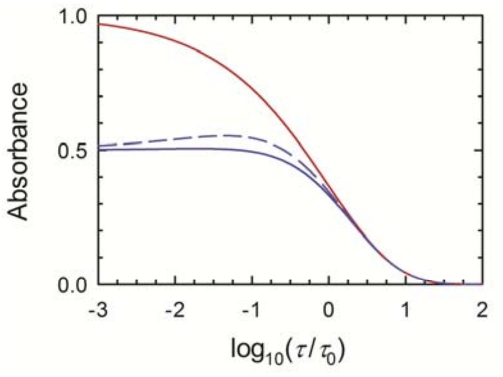

Figure 2.5. Two zero-time cuts through the 2D MUPPETS signal. Red (upper) curve: $2A^{(2)}(0, \tau_1)$, which is equivalent to the exciton decay measured in a 1D experiment. Blue (lower) solid curve: $A^{(2)}(\tau_2, 0)$, which has a negative biexciton signal superimposed on the positive exciton signal. The dashed blue curve neglects the cross-relaxation [Eq. (53)]. The curves are normalized to the same amplitude at long time, so the difference between these cuts measures the biexciton decay [Eq. (63)].

In a two-level system, these two cuts are identical.[11, 19, 21] Thus the asymmetry in τ_1 and τ_2 is diagnostic of a biexciton contribution to the signal. Because the two contributions have opposite signs, the cut along $\tau_1 = 0$ may not be monotonic: it can rise as the negative biexciton contribution decays. This feature is also a unique to a multilevel system. The effect is weak for the parameters chosen here, but it can persist under other conditions.[11,12] It is more clearly seen in the dashed blue curve in Fig. 5, which leaves out the effects of cross relaxation.

This feature gives MUPPETS a unique potential to separate exciton and biexciton dynamics. Subtracting the two zero-time cuts [Eqs. (61) and (62)] gives the biexciton decay:

$$\frac{2A^{(2)}(0,\tau_1)-A^{(2)}(\tau_2,0)}{\sigma\sigma' I^{(2)} A'^{(0)}} = C_{2'}(\tau_2)+C_{2'}^{1'}(\tau_2)\,. \tag{63}$$

The small cross-relaxation term can be approximated with Eq. (52) and removed.

In many systems, the exciton shift is too small to spectrally separate exciton and biexciton dynamics. If there is a significant difference in their decay rates, 1D experiments give a power-dependent change in kinetics that can be identified as the contribution of biexcitons. Unfortunately, a long lived photoproduct with a fast exciton decay has exactly the same properties and can be mistaken for a biexciton.[44] In a 2D MUPPETS experiment, a photoproduct with a fast exciton lifetime contributes to $C_{1'}(\tau)$ and is eliminated in Eq. (63). This experiment distinguishes between species that existed before the pulse sequence (photoproducts) and species created during the pulse sequence (biexcitons). This idea is illustrated in more detail by model III below (Sec. 2.4.3.c). It will also be demonstrated experimentally in future papers.[22, 23]

This mechanism fundamentally discriminates between exciton and biexciton signals. If a photoproduct is present and its biexciton decay differs from the biexciton decay of the primary species, the measured $C_{2'}(\tau)$ will contain a mixture of both signals. An extrapolation to zero average power is still needed to eliminate this possibility. The forthcoming papers will also explore the power dependence of the MUPPETS signal in more detail and demonstrate the necessary extrapolation.[22, 23]

The sign change between exciton and biexciton signals is dependent on having a net absorption from the exciton state (excited-state absorption minus stimulated emission) that is weaker than the absorption from the ground state. This condition is satisfied in most real excitonic systems.

2.4.2 Coherent versus incoherent excitons

Any discussion of excitonic systems faces a potential paradox. Any set of zero-order, two-level chromophores can be grouped to form a multilevel system. To avoid a paradox, all multiexciton effects must disappear in the absence of a suitable interaction between the zero-order chromophores. The number of zero-order chromophores to consider is non-trivial in many systems: How many electron–hole pairs in a semiconductor? How many molecules in a dye aggregate? How many “segments” in a conjugated polymer?

Firstly, one cannot define an excitonic system that is overly large. If M zero-order chromophores with an absorption cross-section σ are included, the ground-to-exciton cross-section is $M\sigma$, the exciton-to-biexciton cross-section is $(M-1)\sigma$, and so on. In the limit as M becomes large, Scheme A (Fig. 2) is reached as a limit. In this scheme, the pathways involving multiple excitons have zero amplitude (Fig. 3). The reason is that absorption saturation is lost as M becomes large. Without nonlinear absorption, there can be no signal in a multidimensional experiment.

Secondly, one must consider the nature of the interaction between chromophores. In spectral correlation spectroscopy, the interaction must perturb the zero-order spectroscopy of the system, either splitting the transitions or transferring absorption strength between exciton and biexciton transitions. This relatively strong coupling is sufficient, but not necessary, to create multiexciton effects in MUPPETS.

We focus on the more difficult case where the zero-order spectra and cross-sections are not perturbed and an exciton would not be seen in spectral measurements:

$$\left(\sigma_{D/T}\right)_{1'}^{0'}(\omega) = 2\left(\sigma_{D/T}\right)_{2'}^{1'}(\omega)\,. \tag{64}$$

This equation requires that both the integrated cross-sections and the cross-section at each frequency are not perturbed, that is, there is no coherent coupling. Even without spectral interactions, there can be an interaction that perturbs the rates, for example, one that causes exciton–exciton annihilation. This interaction constitutes an incoherent coupling.

This coupling expresses itself primarily through the cross-relaxation function, which we previously calculated in the limit of strong incoherent coupling, $k_b >> 2k_e$, Eq. (51). In the limit of no coupling, statistics cause the biexciton rate to be twice the exciton rate,

$$k_b(t) = 2k_e(t)\,, \tag{65}$$

or the biexciton decay to be the square of the exciton decay,

$$G_{2'}^{2'}(t_1,t_0) = \left(G_{1'}^{1'}(t_1,t_0)\right)^2 . \tag{66}$$

Putting this zero rate-coupling limit into Eq. (A217) gives

$$G_{1'}^{2'}(t_2,t_1) = G_{1'}^{1'}(t_2,t_1) - G_{2'}^{2'}(t_2,t_1)\,. \tag{67}$$

The relevant 2D cross-relaxation function [Eq. (47)] is then

$$C_{1'\ 1'}^{2'}(\tau_2,\tau_1) = C_{1'1'}(\tau_2,\tau_1) - C_{2'2'}(\tau_2,\tau_1)\,. \tag{68}$$

In the absence of spectral perturbations, the relative cross-sections for the three 2D pathways are those of Scheme C (Fig. 3). With Eq. (68), the cross-relaxation pathway (ii) partially cancels the exciton–exciton pathway (iii), but completely cancels the exciton–biexciton pathway (i). Thus, all multiexciton effects disappear from MUPPETS unless there is an incoherent coupling that violates Eq. (65). Conversely, any deviation from Eq. (65) creates excitonic effects that are detectable in MUPPETS. However, a coherent coupling that violates Eq. (64) is not required. Thus, a system may need to be treated as an incoherent exciton in MUPPETS, even when it does not need to be treated as a coherent exciton in spectral correlation spectroscopy.

The difference between incoherent and coherent excitons is one of degree, not of kind. Consider the interaction energy coupling the zero-order chromophores. The inverse of this energy gives an interaction time that describes the rate of energy transfer between the chromophores. To have a coherent coupling that is detectable in coherent spectroscopy, the interaction time must be on the order of or shorter than the dephasing time, i.e., there must be coherent energy transfer. If the interaction is weaker, it can still induce incoherent energy hopping that leads to exciton–exciton annihilation. So long as the annihilation time is on the order of or shorter than the population decay time, an incoherent coupling will perturb the rates and will be detected by MUPPETS. If the population decay time is longer than the dephasing time, a system may constitute an incoherent exciton, even when it is too weakly coupled to form a coherent exciton.

2.4.3 Measuring exciton−biexciton correlations

The full 2D-MUPPETS signal, $A^{(2)}(\tau_2, \tau_1)$ with both τ_1 and τ_2 varying, depends on correlations in the kinetics. The exciton−exciton correlation $C_{1'1'}(\tau_2, \tau_1)$ reports on whether the dispersion in $C_{1'}(\tau_1)$ is due to a homogeneous [Eq. (45)] or a heterogeneous [Eq. (46)] mechanism. This idea has been thoroughly discussed in two-level systems.[11, 14, 19-21] The new feature in excitonic systems is the exciton−biexciton function $C_{2'1'}(\tau_2, \tau_1)$, which reports on correlations between two different transitions. To illustrate the behavior of this function, we will calculate the 2D-MUPPETS signal for four limiting models: homogeneous or heterogeneous exciton kinetics combined with either correlated or uncorrelated exciton–biexciton kinetics.

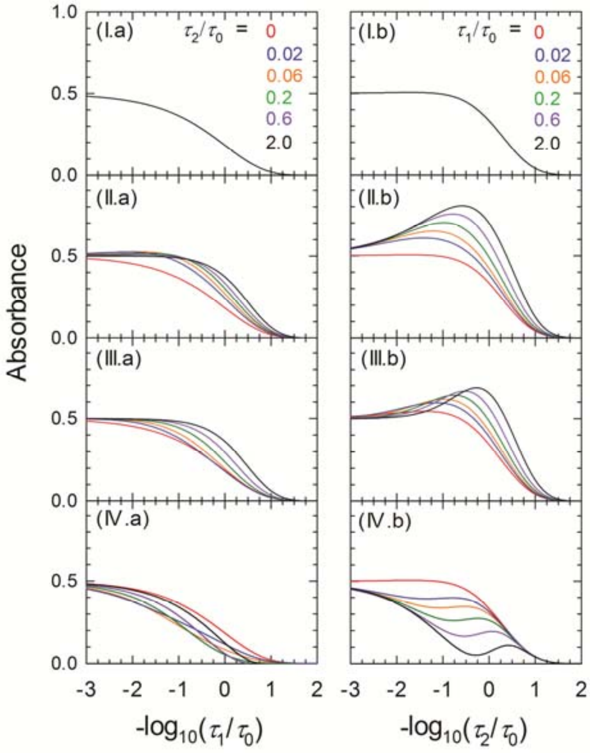

Figure 2.6. The total 2D-MUPPETS time decays $A^{(2)}(\tau_2, \tau_1)$ for models I (homogeneous exciton, uncorrelated biexciton), II (heterogeneous exciton, uncorrelated biexciton), III (heterogeneous exciton, uncorrelated biexciton) and IV (homogeneous exciton, correlated biexciton). (a) The signal versus τ_1 for various values of τ_2 normalized at $\tau_1 = 0$. In model I, all curves overlap. (b) The signal versus τ_2 for various values of τ_1 normalized at $\tau_2 = 0$. All models have the same 1D decays (Fig. 4).

The time-domain representation of the final signal for each model is shown in Fig. 6. As discussed in Sec. 2.4.1, the decays in τ_1 and in τ_2 are not symmetric, a characteristic of a multilevel system. All the models have identical 1D decays (Fig. 4), but the 2D decays in Fig. 6 are quite different. On an empirical basis, 2D MUPPETS can distinguish different levels of exciton heterogeneity and different levels of exciton−biexciton correlation.

A more rational discussion of the different results is possible using the 2D rate spectra of the total signal and the components contributing to it (Fig. 7). In two-level systems, the diagonal of a 2D rate spectrum is always the square of the 1D rate spectrum and is the same for all models.[11] The spectra also have reflection symmetry about the diagonal. In multilevel systems, these features remain in the exciton–exciton components [Fig. 7(I.a–III.a)] but are lost in the total spectra [Fig. 7(I.c–III.c)].

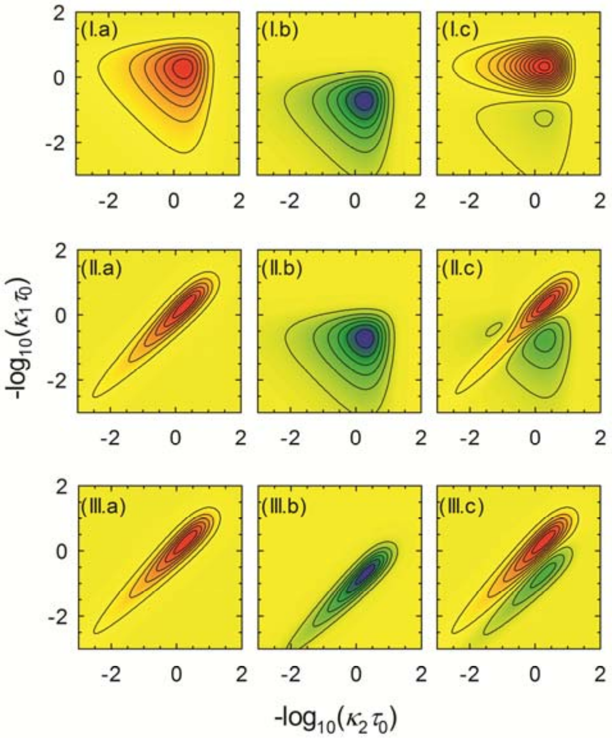

Figure 2.7. 2D-MUPPETS rate spectra for models I (homogeneous exciton, uncorrelated biexciton), II (heterogeneous exciton, uncorrelated biexciton) and III (heterogeneous exciton, uncorrelated biexciton). (a) The exciton−exciton component, $\hat{C}_{1'1'}(y_2, y_1)$, with $y = \log_{10}(\kappa\tau_0)$. (b) The negative of the exciton−biexciton component, $-\hat{C}_{2'1'}(y_2, y_1)$. (c) The total signal, $\hat{A}(y_2, y_1) \propto \hat{C}_{1'1'}(y_2, y_1) - \frac{1}{2}\hat{C}_{2'1'}(y_2, y_1) - \frac{1}{2}\hat{C}^{2'}_{1'1'}(y_2, y_1)$. Delta functions have been broadened by a Gaussian with a width of 0.3 decades. Contours are linear with red/orange positive, yellow zero, green/blue negative.

2.4.3.a Model I: Homogeneous exciton and uncorrelated biexciton

In model I, all the particles are identical, i.e., there is no heterogeneity. The exciton decay of any single chromophore is dispersed due to a complex relaxation mechanism, i.e. the dispersion is homogeneous. In this case, the exciton−exciton correlation function in time is given by Eq. (45). The corresponding rate spectrum,

$$\hat{C}_{1'1'}(y_2, y_1) = \hat{C}_{1'}(y_2)\hat{C}_{1'}(y_1), \tag{69}$$

is shown in Fig. 7(I.a). The amplitude along the diagonal is the square of the 1D exciton spectrum in Fig. 4(b).[11] In this model, the off-diagonal amplitude takes on its maximum value everywhere. If the decays were modeled with discrete rates instead of continuous distributions, the off-diagonal amplitude would appear as cross peaks linking rates lying on the diagonal.[11] The off-diagonal amplitude shows that the corresponding diagonal rates are components of a single, complex relaxation process: the diagonal rates "co-exist" on the same chromophore.

Model I additionally assumes that the exciton and biexciton relax by independent and unrelated mechanisms. Thus, the exciton and biexciton kinetics are uncorrelated:

$$C_{2'1'}(\tau_2, \tau_1) = C_{2'}(\tau_2)C_{1'}(\tau_1)\,. \tag{70}$$

The negative of the corresponding rate spectrum,

$$\hat{C}_{2'1'}(y_2, y_1) = \hat{C}_{2'}(y_2)\hat{C}_{1'}(y_1), \tag{71}$$

is shown in Fig. 7(I.b). The spectrum is no longer centered on the diagonal, but rather on a shifted, parallel line. The spectrum shows strong amplitude off this line, just as the exciton–exciton spectrum shows strong off-diagonal amplitude. Thus, rate homogeneity of a single transition [Eqs. (45) and (69)] is analogous to a lack of correlation in the rates of two transitions [Eqs. (70) and (71)]. In either case, knowing that a rate is observed on a given chromophore in one measurement does not give any additional information on whether a different rate will be observed on the same chromophore in a second measurement.

The identifying characteristic of fully homogeneous/uncorrelated kinetics is that the 2D signal is separable in the two time variables or in the two rate variables. This separability extends to the cross-relaxation [Eqs. (45) and (53)] and thus, to the total signal. In the time decays of Figs. 6(I.a) and 6(I.b), separability causes all the curves in either plot to overlap after normalization. In the rate spectra, it is this separability that leads to a maximal spread along the anti-diagonal direction.

Figure 7(I.c) shows the rate spectrum of the total signal, including the cross-relaxation. There is strong overlap of the exciton–exciton and exciton–biexciton components, but enough information remains to identify the important features of each component. A horizontal node is formed by cancellation between the exciton–exciton and exciton–biexciton components. The horizontal node reflects the separability of the total signal and, thus, is an identifying feature of a homogeneous and uncorrelated system.

2.4.3.b Model II: Heterogeneous exciton and uncorrelated biexciton

In model II, each chromophore has a simple, exponential exciton decay, i.e., there is no homogeneous dispersion. The dispersion of the ensemble decay [Eq. (55)] is only due to differences in the decay rates of different chromophores, i.e., the dispersion is due to heterogeneity. In this case, the exciton−exciton correlation function is given by Eq. (46). The corresponding rate-correlation spectrum,

$$\hat{C}_{1'1'}(y_2, y_1) = \hat{C}_{1'}(y_1)\delta(y_1 - y_2)\,, \tag{72}$$

is shown in Fig. 7(II.a). The diagonal amplitude is identical with that of model I [Fig. 7(I.a)]. However in model II, there is no off-diagonal amplitude. The lack of off-diagonal amplitude indicates that different rates do not "co-exist" on a single chromophore: each rate is associated with a different chromophore.

As with model I, model II assumes that the exciton and biexciton decay by independent mechanisms. In particular, the exciton heterogeneity has no effect on the biexciton decay. As a result, Eqs. (70) and (71) still hold for the biexciton−exciton correlation function, and Eq. (53) holds for the cross-relaxation. The biexciton−exciton spectrum [Fig. 7(II.b)] is unchanged from model I [Fig. 7(I.b)]. However, the total spectrum [Fig. 7(II.c)] is quite distinct from that of model I [Fig. 7(I.c)].

The corresponding results in the time domain can be interpreted by regarding one time period as a rate-based filter to select a subensemble whose decay is measured in the other time period. Figure 6(II.b) shows the decay in τ_2, which measures the sum of exciton and biexciton decays. As τ_1 increases, the first time period progressively removes chromophores with a fast exciton decay. The exciton component during τ_2 slows as τ_1 increases. However, the biexciton component is unaffected by filtering based on the exciton decay time. As these two components become separated in time, the signal rise due to biexciton decay becomes visibly distinct from the slower exciton decay.

Figure 6(II.a) shows the decay in τ_1, which measures only the exciton decay. When $\tau_2 = 0$, all chromophores are measured. As τ_2 increases, the second time period progressively selects for chromophores with well separated exciton and biexciton lifetimes, as these have less signal cancellation. With no correlation between exciton and biexciton lifetimes, these are the chromophores with a long exciton lifetime. Thus, the exciton decay in τ_1 slows as τ_2 increases.

2.4.3.c Model III: Heterogeneous exciton and correlated biexciton

We now introduce exciton–biexciton correlation. Whereas lack of correlation always produces the same result regardless of the mechanistic details, models with correlation require a more detailed specification of how the correlation is produced. Model III assumes that the exciton and biexciton decays of an individual chromophore are both exponential, that is,

$$G_{1'}^{1'}(t_1,t_0;\theta) = e^{-k_e(\theta)(t_1-t_0)} \tag{73}$$

and

$$G_{2'}^{2'}(t_1,t_0;\theta) = e^{-k_b(\theta)(t_1-t_0)} . \tag{74}$$

Dispersion in the ensemble decay is only due to heterogeneity. In Eqs. (73) and (74), the rate is constant in time, but varies with θ, a static or slow bath variable that varies from chromophore to chromophore. This variable has a probability distribution $D(\theta)$, giving the 1D correlation functions

$$C_{1'}(\tau) = \int D(\theta) e^{-k_e(\theta)\tau}\, d\theta \tag{75}$$

and

$$C_{2'}(\tau) = \int D(\theta) e^{-k_b(\theta)\tau}\, d\theta . \tag{76}$$

As in model II, Eqs. (46) and (72) give the heterogeneous exciton−exciton time decay and rate spectrum [Fig. 7(III.a)].

In model I, the exciton and biexciton rates depended on different, independent bath coordinates, $k_e(\theta_e)$ and $k_b(\theta_b)$, and so their dynamics are uncorrelated. In model III, correlation occurs because the exciton and biexciton rates depend on the same bath variable [Eqs. (73) and (74)]. The exact nature of the common dependence must also be specified. For purposes of illustration, we choose

$$k_b(\theta) = ck_e(\theta)\,, \tag{77}$$

which is consistent with the similarity of the exciton and biexciton decay shapes that we have already assumed [Eq. (57)]. The biexciton−exciton correlation function [Eq. (47)],

$$C_{2'1'}(\tau_2,\tau_1) = \int D(\theta) G_{2'}^{2'}(t_2,t_1;\theta) G_{1'}^{1'}(t_1,t_0;\theta)\, d\theta\,, \tag{78}$$

reduces to

$$C_{2'1'}(\tau_2,\tau_1) = C_{1'}(c\tau_2+\tau_1) = C_{2'}(\tau_2+\tau_1/c)\,. \tag{79}$$

When $c = 1$, this equation reduces to the exciton−exciton result for pure heterogeneity [Eq. (46)]. Thus, pure heterogeneity on a single transition is analogous to perfect correlation between two transitions. In a purely heterogeneous sample, one measurement of the exciton rate on a chromophore gives perfect knowledge of the biexciton rate that will be found in a subsequent measurement.

The corresponding exciton−biexciton rate spectrum,

$$\hat{C}_{2'1'}(y_2,y_1) = \hat{C}_{1'}(y_1)\delta(y_1 - y_2 + \ln c)\,, \tag{80}$$

is shown in Fig. 7(III.b). The spectrum traces out a curve in the y_2−y_1 plane. With the simple correlation defined by Eq. (77), the curve is a straight line. Others forms would generate more complex curves. In general, an experimental result in the form of a one-dimensional curve is diagnostic for correlated heterogeneity, and the form of the curve allows the form of the correlation to be inferred.

The total rate spectrum and time decay are shown in Fig. 7(III.c) and Fig. 6(III.a−b), respectively. These include the cross relaxation,

$$C_{1'1'}^{2'}(\tau_2,\tau_1) = C_{1'}(c\tau_2+\tau_1) - C_{1'}((c+1)\tau_2+\tau_1)\,, \tag{81}$$

which is calculated from Eqs. (49) and (51), and its rate spectrum,

$$\begin{aligned}\hat{C}_{1'1'}^{2'}(y_2,y_1) = \hat{C}_{1'}(y_1)\big[&\delta(y_1-y_2+\ln c)\\ &-\delta(y_1-y_2+\ln(c+1))\big] \quad .\end{aligned} \tag{82}$$

In this figure, the node of the rate spectrum lies parallel to the diagonal, reflecting the simple linear form of Eq. (77). More generally, the node will reflect the shape of the exciton–biexciton correlation function and, thus, the form of the correlation.

The interpretation of the time decays is similar to that for model II. In Fig. 6(III.b), as τ_1 increases, chromophores with fast relaxing excitons are eliminated from the measurement. In this model, the remaining chromophores have both a slower exciton and a slower biexciton decay. Both the rise and fall of the signal are delayed as τ_1 increases. Figure 6(III.a) shows the converse effect. As τ_2 increases, only chromophores with slow decays (either exciton or biexciton) reach the detection phase of the experiment. The exciton decay of the selected chromophores is measured during τ_1 and slows as the selection criterion becomes stricter.

2.4.3.d Model IV: Homogeneous exciton and correlated biexciton

Model I considered the case of purely homogeneous dispersion in the exciton and biexciton decays. More precisely, each chromophore had a time dependent rate $k_e(t)$ and $k_b(t)$ for the exciton and biexciton, respectively. Underlying this time-dependence is a bath variable $\varphi(t)$ that is relaxing to a new value in the excited state. In model I, the exciton and biexciton rates depend on different, independent bath coordinates, $k_e(\varphi_e(t))$ and $k_b(\varphi_b(t))$, and so their dynamics were uncorrelated. Model IV makes the same basic assumptions,

$$C_{1'}(\tau_1) = G_{1'}^{1'}(t_1, t_0; \varphi) = \exp\left(-\int_{t_0}^{t_1} k_e(\varphi(t))dt \right) \tag{83}$$

and

$$C_{2'}(\tau_1) = G_{2'}^{2'}(t_1, t_0; \varphi) = \exp\left(-\int_{t_0}^{t_1} k_b(\varphi(t))dt \right), \tag{84}$$

but assumes that the exciton and biexciton decays depend on the same bath property, and so are perfectly correlated.

In the absence of heterogeneity, the exciton−exciton correlation function is the same as in model I [Eqs. (45) and (69)]. The biexciton−exciton correlation function is calculated without ensemble averaging, i.e., from

$$C_{2'1'}(\tau_2, \tau_1) = G_{2'}^{2'}(t_2, t_1)G_{1'}^{1'}(t_1, t_0), \tag{85}$$

but more information on the dynamics of $\varphi(t)$ is needed. We make the simple assumption that the dynamics of $\varphi(t)$ are the same in the exciton and biexciton state. In this case,

$$\begin{aligned} C_{2'1'}(\tau_2, \tau_1) &= \frac{G_{2'}^{2'}(t_2, t_0)G_{1'}^{1'}(t_1, t_0)}{G_{2'}^{2'}(t_1, t_0)} \\ &= \frac{C_{2'}(\tau_2 + \tau_1)C_{1'}(\tau_1)}{C_{2'}(\tau_1)} \quad . \end{aligned} \tag{86}$$

This result can be interpreted by writing it as

$$C_{2'1'}(\tau_2,\tau_1)=\left(1+Z(\tau_2,\tau_1)\right)C_{2'}(\tau_2)C_{1'}(\tau_1)\,. \tag{87}$$

with

$$Z(\tau_2,\tau_1)=\frac{C_{2'}(\tau_2+\tau_1)}{C_{2'}(\tau_2)C_{2'}(\tau_1)}-1\,. \tag{88}$$

The function $Z(\tau_2, \tau_1)$ measures the rate dispersion of $C_{2'}(\tau)$. When $C_{2'}(\tau)$ is an exponential, $Z(\tau_2, \tau_1) = 0$ everywhere. When $C_{2'}(\tau)$ is not exponential, $Z(\tau_2, \tau_1)$ is still zero along the $\tau_1 = 0$ and $\tau_2 = 0$ edges of its domain, but it is nonzero in the middle: positive if the rate slows with time, and negative if the rate increases with time. Thus, Eq. (87) has the maximum deviation from the uncorrelated result [Eq. (45)] allowed by the dispersion of $C_{2'}(\tau)$. For the our model functions, this deviation is a positive one for large values of τ_1 and τ_2. Under certain conditions, this deviation can give a signal that rises with delay in some regions, for example in Fig. 6(IV.b). Rate spectra for this model are difficult to calculate and are not easy to interpret and so are not presented.

2.5 THERMAL SIGNALS IN MULTILEVEL SYSTEMS

1. General formalism

Heterodyned experiments are not only sensitive to resonant absorption from the solute; they are also sensitive to index-of-refraction changes in the solvent due to the heat released by non-radiative decay. In 1D, these effects are called thermal gratings.[24-26] (The total thermal response can be separated into a pure thermal and an acoustic component, but that distinction will not be needed here.) In Ref. [18], we showed how to incorporate thermal effects into pathway calculations of multidimensional experiments. Here that treatment is extended to multilevel systems.

The system states must be expanded to include not only the electronic state of the solute P, but also the energy density of the solvent ε, that is, the state must have the form $|P\ \varepsilon]$. The energy density is measured at the same (suppressed) k-vector as the electronic state. The response to the solvent energy is linear, so $|P\ \varepsilon_1] + |P\ \varepsilon_2] = |P\ \varepsilon_1{+}\varepsilon_2]$. It will be convenient to shift from ε, the heat per volume of solvent, to n_ε, the number of photons of energy converted to heat per solute molecule,

$$n_\varepsilon = \frac{\varepsilon}{\hbar\omega\rho}\,. \tag{89}$$

An important result of Ref. [18] is that in a multidimensional experiment, only the thermal signal formed by the last excitation is detectable. Thus, the expanded states are only needed at the end of the pathways (see Fig. 8).

The generalized absorption due to thermal effects $A_\varepsilon^{(N)}(\tau_N,\ldots,\tau_1)$ adds to the resonant absorption $A^{(N)}(\tau_N,\ldots,\tau_1)$ [Eq. (9)] and can be expressed in an analogous form,

$$\begin{aligned} A_\varepsilon^{(N)}(\tau_N,\ldots,\tau_1) = (-1)^N \rho L I^{(N)} &[\boldsymbol{I}\,|\,\boldsymbol{\sigma}_{D\varepsilon} \\ &\times\int_{t_{N-1}}^{t_N} C_\varepsilon(t_N-t')\frac{d}{dt'}\mathbf{G}_\varepsilon(t',t_{N-1})\,dt' \\ &\times\ldots\boldsymbol{\sigma}_T\mathbf{G}(t_1,t_0)\boldsymbol{\sigma}_T\,|\,\boldsymbol{eq}] \end{aligned} \quad . \tag{90}$$

The thermal detection cross-section operator $\boldsymbol{\sigma}_{D_\varepsilon}$ can be expressed in terms of $\mathbf{n}_\varepsilon$, the operator that measures the value of n_ε,

$$\boldsymbol{\sigma}_{D\varepsilon} = i\sigma''_\varepsilon\mathbf{n}_\varepsilon\,. \tag{91}$$

Because the thermal response is a change in the index-of-refraction, the operator is imaginary. Its magnitude is

$$\sigma''_{\varepsilon} = \frac{\omega}{c}\left(1+\frac{1}{n_s^2}\right)\left(\frac{-dn_s}{d\rho_s}\right)\left(\frac{d\rho_s}{d\varepsilon_s}\right)\hbar\omega\,, \tag{92}$$

where n_s is the solvent index-of-refraction, and ρ_s is the solvent density. This quantity has the units of a cross-section and is normally real and positive. The time-evolution operator for the electronic state $\mathbf{G}(t',t)$ is expanded to $\mathbf{G}_{\varepsilon}(t',t)$, the time-evolution operator of the combined electronic–thermal state, for the last time period.

The detection is not of the energy itself, but of the resulting change in index-of-refraction. In Eq. (90), the energy deposition is convolved with $C_{\varepsilon}(\tau)$, the time-evolution of thermal energy into an index-of-refraction change. Sophisticated expressions for $C_{\varepsilon}(\tau)$ valid over a wide time range are available.[25, 45-48] For purposes of illustration over short times,

$$C_{\varepsilon}(\tau) = 1 - \cos(2\tau / \Gamma) \tag{93}$$

is an adequate expression.[18] This thermal correlation function is zero when $\tau = 0$ and reaches a maximum of two at the half the acoustic period Γ due to interference between the slowly decaying pure thermal response and the more rapidly oscillating acoustic response.

The convolution in Eq. (90) can be removed, if the decay of the electronic state is much faster than the acoustic period. If the decay is not complete within the acoustic period, but only times $\lesssim \Gamma/2$ are treated, this approximation can be pushed farther. The fraction that decays before Γ/4 (halfway to the maximum) is treated as decaying instantaneously, and the fraction that decays after Γ/4 is treated as never decaying. This approximation is rough when the solute relaxation has a single timescale, but becomes more reasonable when the decay is highly dispersed in time. In this approximation,

$$\begin{aligned} A_{\varepsilon}^{(N)}(\tau_N,\ldots,\tau_1) = (-1)^N \rho L I^{(N)} & [\boldsymbol{I}\,|\,\boldsymbol{\sigma}_{D\varepsilon} C_{\varepsilon}(\tau_N) \\ & \times \mathbf{G}_{\varepsilon}(\Gamma/4+t_{N-1},t_{N-1})\ldots \\ & \times \boldsymbol{\sigma}_T \mathbf{G}(t_1,t_0)\boldsymbol{\sigma}_T\,|\,\boldsymbol{eq}] \qquad . \end{aligned} \tag{94}$$

The primed basis set for electronic states can be introduced for the thermal pathways, as they were for resonant pathways in Sec. 2.2.2. The thermal absorption is then written [compare to Eq. (24)]

$$\begin{aligned} \frac{A_{\varepsilon}^{(N)}\;(\tau_N,\ldots,\tau_1)}{A'^{(0)}} = I^{(N)} & \left(\sigma_{\varepsilon}\right)^{0'p,\;\ldots,\;l',j'}_{\qquad m'0,\ldots,k'} \\ & \times \left(C_{\varepsilon}\right)^{m'0,\ldots,k',1'}_{0'p,\ldots,l',\,j'}(\tau_N,\ldots,\tau_1) . \end{aligned} \tag{95}$$

The final two indices are expanded to include the thermal variables. The total thermal cross-section is given by [compare to Eq. (25)]

$$\left(\sigma_{\varepsilon}\right)^{n'p,\;\ldots,\;l',j'}_{\qquad m'0,\ldots,k'} = (-1)^N \left(\sigma_{D\varepsilon}\right)^{n'p} \left(\sigma_T\right)^{l'}_{m'0} \cdots \left(\sigma_T\right)^{j'}_{k'} . \tag{96}$$

The full operator **σ**$_{D\varepsilon}$ has been reduce by one dimension and converted to a vector as in Eq. (22),

$$[\sigma_{D\varepsilon}| = \frac{\left(\sigma_T\right)^{0'}_{1'}}{\mathrm{Re}\left(\sigma_D\right)^{0'}_{0'}} [0'p\,|\,\boldsymbol{\sigma}_{D\varepsilon} , \tag{97}$$

with the result that

$$\left(\sigma_{D\varepsilon}\right)^{n'p} = i\sqrt{2}\,\delta_{n'0'}\sigma''_{\varepsilon} p . \tag{98}$$

Because $\boldsymbol{\sigma}_{D\varepsilon}$ is diagonal in the electronic state, only the $n' = 0$ elements are nonzero. The multidimensional correlation function in Eq. (95), which corresponds to the one in Eq. (14), is

$$\begin{aligned}\left(C_{\varepsilon}\right)^{m'0,\ldots,i'}_{0'p,\ldots,j'}(\tau_N,\ldots,\tau_1) &= C_{\varepsilon}(\tau_N)\\ &\times\left\langle \left(G_{\varepsilon}\right)^{m'0}_{0'p}(\Gamma/4+t_{N-1},t_{N-1})\ldots G^{i'}_{j'}(t_1,t_0)\right\rangle. \qquad (99)\end{aligned}$$

The time evolution in the last time period is now governed by the thermal response, rather than by solute dynamics.

2.5.1 Results for excitonic systems

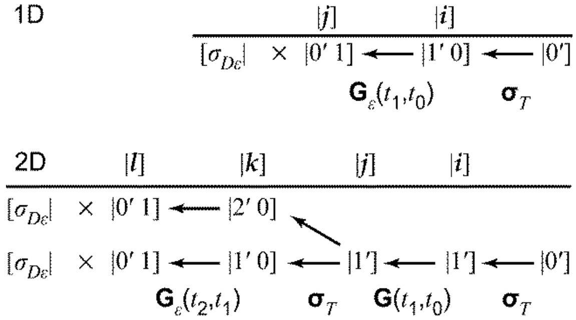

Figure 2.8. Pathways for the calculation of thermal signals in one-dimensional (1D) and two-dimensional (2D) experiments [see Fig. 3]. The final two states of the pathways are expanded to $|P\ n_\varepsilon]$ to show both P, the electronic state, and n_ε, the number of quanta of thermal energy deposited in the solvent.

In an excitonic system, the number of pathways is severely limited. As with the electronic signal, the primed basis set yields the minimum number of pathways. Figure 8 shows the allowed pathways for $N = 1$ and $N = 2$. Only two elements of $\mathbf{G}_\varepsilon(t', t)$ are needed. In calculating them, we allow nonradiative decay that leads to long lived, high energy states ("trap" states) without the immediate release of heat. The fractional yield of heat for the biexciton-to-exciton and exciton-to-ground transitions are Q_2 and Q_1 respectively. The required matrix elements are then

$$\begin{aligned} \left(G_\varepsilon\right)_{0'1}^{1'0}(t',t) &= \frac{Q_1}{\sqrt{2}}\left(1-G_{1'}^{1'}(t',t)\right) \\ \left(G_\varepsilon\right)_{0'1}^{2'0}(t',t) &= \frac{Q_2}{\sqrt{2}}\left(1-G_{2'}^{2'}(t',t)\right)+\frac{Q_1}{\sqrt{2}}G_{1'}^{2'}(t',t)\,. \end{aligned} \tag{100}$$

In the primed basis set when the cross relaxation is small, each thermal pathway is dominated by the relaxation of a single electronic transition.

Combining Eqs. (95)–(100) with the pathways in Fig. 8 yields expressions for the thermal signals,

$$A_\varepsilon^{(1)}(\tau_1) = A'^{(0)} I^{(1)}\left(-i\sigma''_\varepsilon\right) C_\varepsilon(\tau_1) Q_1\left(1-C_{1'}(\Gamma/4)\right) \tag{101}$$

and

$$\begin{aligned} A_\varepsilon^{(2)}(\tau_2,\tau_1) = {} & A'^{(0)} I^{(2)}\left(-i\sigma''_\varepsilon\right)\left(2\sigma'\right) C_\varepsilon(\tau_2) \\ & \times\Big\{\left(Q_1-\tfrac{1}{2}Q_2\right)C_{1'}(\tau_1)-Q_1 C_{1'1'}(\Gamma/4,\tau_1) \\ & +\tfrac{1}{2}\Big[Q_2 C_{2'1'}(\Gamma/4,\tau_1)-Q_1 C_{1'1'}^{2'}(\Gamma/4,\tau_1)\Big]\Big\} \end{aligned} \quad . \tag{102}$$

The results for the different models in Fig. 2 differ in only minor ways; model C has been used for specificity. The 1D result is consistent with previous work.[24-26] The 2D result is new. It allows the thermal effects to be calculated from the correlation functions already discussed in Sec. 2.4. The thermal cross-section in the 2D expression can be obtained from 1D experiments. The only new information in the 2D thermal signal is the quantum yield of heat for the biexciton decay. Thus, 2D experiments have the potential to measure this quantity.

2.6 CONCLUSIONS

This paper has laid the theoretical foundation for MUPPETS in multilevel systems, especially excitonic systems. The calculations were simplified by introducing a nonorthogonal basis set. By using population conservation, the number of states to be considered was reduced by one. In an excitonic system, the number of pathways and correlation functions are reduced further. An unavoidable complication of multilevel systems is cross-relaxation between basis states. However, suitable approximations were found in the limits of either strong or weak exciton−exciton interaction. Methods for calculating thermal effects in multilevel systems were also presented.

Using these methods, the new information available from MUPPETS was demonstrated. MUPPETS was shown to be very sensitive to chromophore interactions. First, it was shown that much weaker interactions are needed to observe kinetic effects, that is, to form an incoherent exciton, than are needed to observe spectral effects, that is, to form a coherent exciton. In an incoherent exciton, chromophores interact by incoherent energy hopping followed by exciton−exciton annihilation. Secondly, it was shown that MUPPETS is a sensitive method for detecting incoherent exciton formation. Any asymmetry in the decays along the two time axes is a sign of an incoherent exciton. The difference between these decays is a direct route to the biexciton decay rate and, thus, to the strength of exciton−exciton interactions. Exciton−exciton annihilation can also be measured by power-dependent 1D experiments, but these measurements can be confounded by the build-up of long-lived photoproducts with short exciton lifetimes. MUPPETS is immune to this problem.

Away from the time axes, MUPPETS offers additional information for systems with rate dispersion. Both exciton rate heterogeneity and correlations between exciton and biexciton dynamics are available. Example calculations suggest that there is sufficient information to allow a unique separation of these two effects in most cases. Rate heterogeneity is a concept that has been explored in previous MUPPETS studies of two-level system; the concept of correlated rates between two transitions is a new one. When the rates of two transitions are correlated, the MUPPETS results are similar to those for heterogeneous rates on a single transition. Correlation indicates that the relaxation mechanisms of the two transitions are linked. Correlation is possible whether the individual relaxations are heterogeneous or homogeneous. In the heterogeneous case, individual particles relax either faster or slower than average for both transitions. In the homogeneous case, the relaxations of both transitions depend on the relaxation of a common bath mode.

The practicality of these ideas will be demonstrated in a future paper.[22, 23] The results in this paper provide a basis for both a qualitative and quantitative interpretation of those results.

CHAPTER 3 RATE DISPERSION IN THE BIEXCITON DECAY OF CDSE/ZNS NANOPARTICLES FROM MULTIPLE POPULATION-PERIOD TRANSIENT SPECTROSCOPY

The lifetime of a biexciton is important in many optoelectronic applications of semiconductor nanostructures.[49-51] Early on, Auger recombination was identified as a likely decay mechanism.[43, 52] Properties of the core were seen as primary in controlling the rate. As a one-step relaxation, it should have an exponential decay on a single particle, and as a core-based mechanism, it should have a relatively uniform rate from particle to particle. Thus, the ensemble biexciton decay has often been assumed to be exponential. Observations of nonexponential decay are easily attributed to additional contributions from higher excitons or photoproducts. In this communication, a six-pulse, multidimensional spectroscopy is used to separate the biexciton decay from other potential contributions. The biexciton decay is found to be highly dispersed, i.e., nonexponential, and the form of the rate dispersion is accurately measured.

In many experiments on semiconductor nanoparticles, excitons, biexcitons and higher excitons are created simultaneously. Isolating the biexciton contribution is not simple. The separation between exciton and biexciton transitions is small, making their spectral resolution difficult.[53] Decomposing the fluence dependence is complicated by saturation combined with spatial variation of the light intensity within the sample. Because of these problems, the identification of biexcitons and the quantification of their properties has often relied on the decomposition of kinetic traces into exponential components.[43, 44, 52, 54, 55] Slow, fluence-independent components are identified as excitons and fast, fluence-dependent components are identified as multiexcitons. The explicit assumption of exponential decay has been used to decompose the faster, fluence-dependent component into bi-, tri- and higher excitons.[52, 54] This approach has been widely used to study the biexciton decay mechanism[43] and to identify multiple exciton generation from single photons.[44, 55]

However, recent investigations make the form of the biexciton decay less certain and change it into an important experimental question. Challenges to the Auger mechanism have been raised,[56-58] opening the possibility of a multistep mechanism and/or mechanisms with greater particle-to-particle variation. Even within the Auger model, an important role for the surface is being recognized.[59] Bawendi and coworkers have argued that surface heterogeneity can translate into a distribution of biexciton decay rates.[60] Single-particle experiments have found particle-to-particle variation in the biexciton quantum yields that support this idea.[60, 61]

It has also been appreciated that long lived, but reversible, photoproducts can mimic biexcitons in a kinetic analysis.[44, 51, 62] Various experiments; single-particle blinking,[50, 63] transient absorption,[64] and photobleaching;[65] suggest the existence of one or more such photoproducts with a low quantum yield of emission, i.e., a fast exciton lifetime. A charged exciton is a leading candidate for such a photoproduct, but the topic is still unresolved. The photostationary concentration of a photoproduct scales with the excitation fluence, as the biexciton concentration does, and the photoproduct has a fast decay, as the biexciton does. If such a photoproduct contaminates a measurement, a multiexponential decay could be falsely attributed to the biexciton.

We use multiple population-period transient spectroscopy (MUPPETS) to measure the form of the biexciton decay in CdSe/ZnS core–shell nanoparticles free from these complications. MUPPETS is a two-dimensional form of ultrafast kinetics: two excitation pulses are separated by a time t_1, and the change in absorbance due to both pulses $A^{(2)}(t_2, t_1)$ is measured after an additional time t_2.[21] The phase-matching condition creates a double difference between the four possibilities of absorption or no absorption from each of the two excitations. The resulting signal isolates the effects due to an interaction between the two excitations. To create the required phase-matching condition, each of the excitations and the final measurement consist of two simultaneous pulses entering the sample from different directions. Thus, the experiment uses a total of six pulses and measures an incoherent component of the $\chi^{(5)}$ response of the sample.

Previously, MUPPETS has been used in systems with only two electronic levels to measure heterogeneity in the rate of the electronic decay.[21] A recent theoretical analysis has revealed a new feature of MUPPETS in multilevel systems—the ability to discriminate between biexcitons and photoproduct excitons.[66] In pump–probe and other one dimensional experiments, the signals from excitons and biexcitons have the same sign, but in MUPPETS they have opposite signs. Starting from the ground state, the first excitation always creates an exciton and reduces the band-edge absorption by approximately one-half. The second excitation has two possibilities. In one pathway, a biexciton is created, reducing the band-edge absorption to zero. In our sign convention, this increased bleach is negative. In the other pathway, the second excitation again creates excitons from ground-state particles, also bleaching the total absorption. However, due to the initial depletion of the ground state by the first pulse, the second pulse has a reduced effect. The effect unique to combining the two excitations is a smaller bleach, which has a positive signal in our sign convention.

Consider a sample with normal particles, which have a slow exciton and a fast biexciton decay, and a fluence-dependent, steady-state concentration of a photoproduct, in which both exciton and biexciton decays are fast. In the low fluence limit, a $\chi^{(3)}$ pump–probe experiment measures only the slow exciton decay of the normal particles. The first-order fluence dependence is a $\chi^{(5)}$ term that contains the fast biexciton decay of the normal particles and the fast exciton decay of the photoproduct, both with the same sign. As a $\chi^{(5)}$ experiment, MUPPETS contains all these contributions, even in the low fluence limit. However, the normal and photoproduct excitons both give a positive signal, whereas the normal biexciton gives a negative signal. This sign change allows the normal biexciton to be distinguished from a potential photoproduct.

Huxter and Scholes previously used a related $\chi^{(5)}$ experiment to study biexciton dynamics,[67] but this communication is the first to demonstrate and exploit the sign difference of exciton and biexciton signals. The separation of exciton and biexciton signals requires only the $t_1 = 0$ cut through the MUPPETS data. The additional information available from the full two-dimensional data set will be analyzed in Reference.[23]

The samples were commercial (NN-Labs) CdSe/ZnS core–shell nanoparticles in toluene with an OD of 0.4 in the 1 mm sample cuvette at the band-edge absorption peak of 520 nm. To reduce the concentration of photoproducts, the sample was flowed through the cuvette with a peristaltic pump and was kept under a nitrogen atmosphere. Excitation fluences are reported as the energy per pulse at the sample in an approximately 200 μm diameter spot size. All pulses wavelengths (527 nm) were near the band edge. Pulse widths were approximately 300 fs, but results are only reported after 1 ps, when fine structure relaxation is complete.[68] The details of the instrument are reported elsewhere.[21]

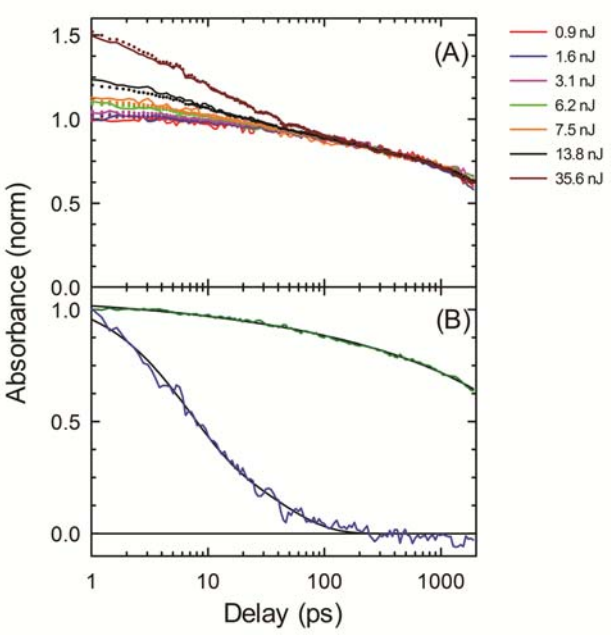

Figure 3.1. Fluence-dependent, band-edge pump–probe results. (A) Solid: Decays at various pulse energies normalized to match at long times. (An additional four energies are shown in Figure 5 in the Supporting Information.) Dots: Data reconstructed from the results in (B). (B) Linear regression at each time point reduces the data of (A) to two components: a low-fluence limit (intercepts, green) and a linear, fluence-dependent component (slopes, blue). The fluence-dependent component is fit to two exponentials (black). Other fits are shown in Figure 4 in the Supporting Information. The fit to the fluence-independent component (black) shows substantial rate dispersion in the exciton as well.[23]

Fluence dependent pump–probe experiments are reported in Figure 3.1A. This method is conventional for measuring biexciton yields and dynamics.[43] The data have been normalized at long times, when only the exciton remains. The early, fluence-dependent decay component may be due to biexcitons or photoproducts. Higher multiexcitons also create absorbance at the band edge, although the mechanism is not well understood.[52, 54] With excitation at the band edge, we hope to avoid creating higher excitons in the first place. The underlying fluence-independent component is assigned to the exciton. The exciton has a strong radiative decay component near 20 ns, but also has decay components throughout the picosecond time range.[55] The origin of rate dispersion in the exciton decay is discussed in Reference.[23]

To avoid any assumptions about the form of either the exciton or biexciton decay, the data have been analyzed by linear regression at each time point. The intercepts (green curve, Figure 3.1B) form the fluence-independent (exciton) decay; the slopes (blue curve, Figure 3.1B) form the fluence-dependent (biexciton/photoproduct) decay. The linearity of the fluence dependence was verified by reconstructing all 11 of the original data sets from these two components (dots, Figure 3.1A) and verifying that there is no systematic deviation.

The fluence-dependent component is distinctly nonexponential. This dispersion could be attributed to inadvertent creation of a triexciton. A three-fold ratio the biexciton and triexciton rates has been reported.[54] This ratio is roughly consistent with the data, although the use of band-edge excitation and the linearity of the fluence dependence both argue against this interpretation. Alternatively, the dispersion could be attributed to accumulation of a photoproduct. The decay rate of the most likely photoproduct, a charged particle, is predicted to have a four-fold ratio with the biexciton rate.[69] Again, this ratio is roughly consistent with the data, but the use of a flowing sample argues against this interpretation. Finally, the dispersion could be inherent to the biexciton itself, despite the lack of a mechanistic justification.

The difficulties in interpreting the pump–probe result are resolved by the MUPPETS data shown in Figure 3.2. The MUPPETS data have been recorded as a function of fluence and extrapolated to the low fluence limit as the pump–probe data were.[23] The magnitude of the complex signal at $t_1 = 0$ is given as the red curve. This data is the sum of a positive exciton decay and a negative biexciton decay. As the negative biexciton contribution decays, the net signal rises. This rise in the signal confirms of the theoretical prediction in Reference [66] of opposite signs for the exciton and biexciton signals. The initial value of 0.5 is consistent with the biexciton absorption cross section being one-half the exciton cross section,[23] as predicted by simple, one-electron models.[43]

The biexciton decay is isolated by matching fluence-independent (exciton) data from the pump–probe experiment (green, Figure 3.2A) at long times and subtracting the MUPPETS data from it. The result is the red curve in Figure 3.2B. Because this result is derived from low fluence limiting data, it is free of higher multiexcitons. It is compared to the fluence-dependent decay from pump–probe measurements, which may contain contributions from a photoproduct. No modeling or fitting of the data is involved in this comparison.

The biexciton decay found from MUPPETS is identical to the fluence-dependent component of pump–probe measurement. This agreement is direct evidence that the precautions taken to eliminate other contributions to the pump–probe–probe experiment have been sufficient and that the rate dispersion is intrinsic to the biexciton decay. The degree of rate dispersion is large enough that it must be accounted for in the kinetic separation of multiexciton decays. It also demands a revision or extension of the biexciton decay mechanism that can account for the dispersion.

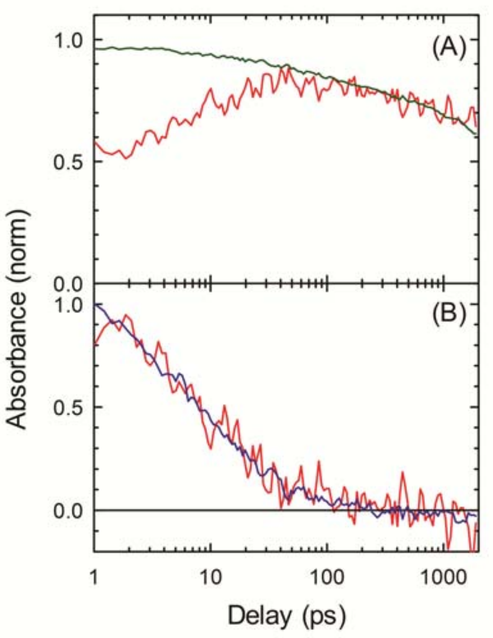

Figure 3.2. (A) Magnitude of the MUPPETS data versus t_2 at $t_1 = 0$ (red) and the fluence-independent component from pump–probe measurements (green, Figure 3.1B). (B) The difference between the curves in (A) gives the biexciton decay (red). It is identical to the fluence-dependent component of the pump–probe measurement (Figure 3.1B, blue).

Quantifying the rate dispersion depends on the mechanism assumed. The dispersion could be due to (1) a multistep relaxation of the biexciton, (2) a relaxation in the environment (e.g., movement of surface species) in response to the creation of the exciton or biexciton that causes the decay rate to slow as a function of time, or (3) a distribution of rates among the particles. A biexponential fit (Figure 3.1B), which is consistent with mechanism (1), gives a 7-fold ratio of rates. Assuming a time dependent rate, which is consistent with mechanism (2), gives a 25% drop in rate in 40 ps. A fit to a continuous distribution of rates, which is consistent with mechanism (3), gives a distribution with a five-fold range of rates at the half-width of the distribution (Figure 3.3**)**. A stretched exponential, which is often used to describe complex dynamics, gives a stretching parameter of β =0.5. Regardless of the description used, the rate dispersion is substantial. (More detail on fits are given in the Supporting Information, SI.)

The biexciton decay rate is known to depend on the particle radius,[43] but the hypothesis that simple size heterogeneity is responsible can be rejected. A 5-fold variation in rate would require a 1.7-fold variation in radius. This variation would also cause a range of 160 nm in the band-edge position,[70] which is not observed spectroscopically. Thus, mechanism (3) requires surface heterogeneity that affects the biexciton decay.

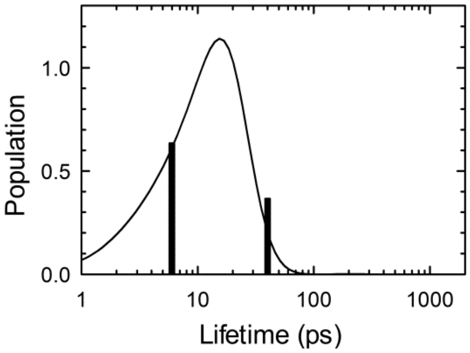

Figure 3.3. Lifetime distributions of the biexciton decay. The bars represent the biexponential fit. The solid curve is a continuous distribution from a maximum entropy fit. For other possible fits, see SI.

Nair, et al. have recently shown that single particle (SP) photon-correlation measurements yield the ratio of biexciton to exciton quantum yields.[60] Using this method, Park et al. reported a four-fold spread in biexciton quantum yields from particle to particle, but in a rather different system—CdSe with a thick CdS shell.[61] Nair et al.'s measurement on CdSe/CdZnS nanoparticles, also showed particle-to-particle variation in the biexciton quantum yields, but with less than a factor of two variation.[60] These results suggest that heterogeneity accounts for part of the rate dispersion seen here, but might not account for all of it.

Several differences between SP measurements and MUPPETS may account for the apparent difference in results. First, SP measurements average over ~100 s of data collection time.[60] If a heterogeneity fluctuates during this time, it will be seen by MUPPETS, but not by SP measurements. Second, a homogeneous source of rate dispersion, such as mechanisms (1) or (2), would not be evident in the SP quantum yield. Thirdly, although both techniques seek the limit of low peak powers, the average powers differ by three orders-of-magnitude: 30 W/cm^2 on a static sample for SP measurements, 0.030 W/cm^2 on a flowing sample for MUPPETS measurements. Thus, the issues presented by photoproducts can be quite different in the two experiments.

The results in this work confirm the recent theoretical treatment of MUPPETS in a general excitonic system[66] and indicate the potential for similar applications of MUPPETS to many other such systems. The biexciton decays measured here is analogous to exciton–exciton annihilation in conjugated polymers, quantum wells, dye aggregates, and photosynthetic systems. MUPPETS has the potential to contribute to understanding exciton transport and exciton–exciton interactions in all such systems.

CHAPTER 4 MULTIPLE POPULATION-PERIOD TRANSIENT SPECTROSCOPY OF CDSE/ZNS NANOPARTICLES. I. EXCITON AND BIEXCITON DYNAMICS

4.1 INTRODUCTION

The nonradiative decay of semiconductor nanoparticles is complicated. For example, the kinetics often have a strongly nonexponential (dispersed) shape. Much of the complexity in these kinetics is due to the important role of surface states. These states have no direct spectral signature, but are observable only through their strong effect on the kinetics of the bright states. MUPPETS (multiple population-period transient spectroscopy) is a new method that separates contributions to kinetics, not using spectral properties, but using the kinetics themselves to define the components.[11, 13-15, 18-22, 66] To separate these components, two time periods are used, i.e., it is a two-dimensional (2D) measurement, in contrast to more conventional pump–probe and transient-grating measurements, which are one-dimensional (1D). Different species are “labeled” by their kinetics during the first period and are then measured separately during the second period. Because kinetics are the main window into surface states, MUPPETS has the potential to add several new types of information about these states in nanoparticles.

In its first uses, MUPPETS was applied to systems that could be modeled as two levels.[11, 13, 14, 19-21] In those cases, it distinguished between rate dispersion due to heterogeneity between chromophores, i.e., heterogeneous dispersion, and rate dispersion due to a complex mechanism present on every chromophore, i.e., homogeneous dispersion. However, the band-edge states in CdSe/ZnS nanoparticles form an inherently multilevel system. This paper is the first full report of MUPPETS applied to such a multilevel system. An initial letter highlighted one important result that required only the magnitude of the $\tau_1 = 0$ slice of the full 2D MUPPETS trace—the existence of strong rate dispersion in the biexciton decay.[22] With the addition of new transient-grating data, both the magnitude and phase of the MUPPETS data are treated here. In addition, data in the full τ_1–τ_2 plane are analyzed for the first time.

The interpretation of this paper's data is dependent on a recent extension of the theory of MUPPETS to multilevel, excitonic systems.[66] That theory predicts four important results are obtainable from MUPPETS: (1) it can report on heterogeneity in the exciton decay, (2) it can separate biexciton dynamics from interfering exciton signals, (3) it can detect connections between the exciton and biexciton decay mechanisms, and (4) it can measure the yield of long-lived trap states. The experiments will be analyzed for all four phenomena. In addition, the potential for three experimental interferences will be tested: (5) thermal effects, which are responsible for (4) if properly analyzed, but can distort the results if not properly accounted for, (6) reversible photoproducts of the CdSe/ZnS nanoparticles, which a number of experiments suggest accumulate under typical experimental conditions,[44, 49-51, 62-64, 71-74] and (7) higher multiexcitons, which have properties similar, but not identical, to those of biexcitons.[43, 52-54, 75-78]

To deal with this complex set of phenomena, this paper is divided into two parts. Chapter 4 deals with the basic 1D and MUPPETS spectroscopy of the nanoparticles. It yields conclusions about the exciton and biexciton dynamics (issues 1–3 and 6). Chapter 5 deals with additional thermal and fluence-induced phenomena.[79] They must be understood to avoid misinterpreting the data, but go beyond the core MUPPETS theory. New theory for the fluence dependence of MUPPETS signals is presented and used to verify that a three-level model of the band-edge is sufficient (issue 7). Chapter 5 will also show that thermal effects have not distorted the conclusions of this paper (issue 4), but that current experimental methods are not stable enough to detect biexciton trap yields in this system (issue 5).

MUPPETS is an extension of transient-grating spectroscopy[24-26, 41, 46, 80] to six pulses. The pulses are grouped into simultaneous pairs: two excitation pairs (1 and 2) and one detection pair (3). Each pulse in a pair (*a* or *b*) enters the sample from a different direction (Figure 4.1). The phase-matching condition selects signal resulting from exactly one electric-field interaction with each pulse. Thus, there are two periods of time evolution, τ_1 and τ_2. The same is true in 2D coherent spectroscopy,[31, 41, 81, 82] which has also been applied to semiconductor nanoparticles.[37, 83-92] However in MUPPETS, the two periods are spent in population states, not coherent states. Nevertheless, MUPPETS can be schematically represented by ladder diagrams reminiscent of those used in coherence spectroscopy (Figure 4.2). These diagrams are an intuitive summary of results that are more rigorously derived in ref [66].

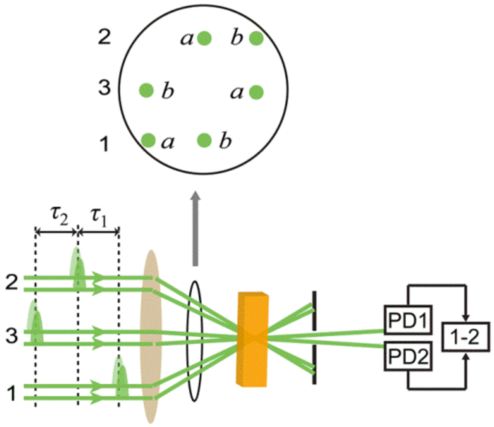

Figure 4.1. Schematic representation of the pulse timing and directions in MUPPETS. Six pulses are grouped into three pairs (1–3). The pulses (green) in each pair (*a* and *b*) are simultaneous in time, but enter the sample (orange) from different directions to meet the phase-matching condition. The time between the two excitation pairs (1 and 2) is the first evolution period τ_1; the time between the second excitation pair (2) and the detection pair (3) is the second evolution period τ_2. Two detectors (PD1 and PD2) are used for differential heterodyne detection.[15]

The nanoparticle is represented by three states with equal spacing: ground (0), exciton (1) and biexciton (2) states. On the left of each diagram in Figure 4.2, the population is in the ground state and is represented by a filled circle. This population gives the $\chi^{(1)}$ response of the system, i.e., the static absorption spectrum. The first pair of pulses (1*a* and 1*b*; solid, red arrows) creates excitons (filled circle) and depletes the ground state (open circle). These circles represent only the first-order perturbative change due to the excitation and predicts the $\chi^{(3)}$ response of the sample, i.e., an absorption bleach. During the first evolution period τ_1, excitons decay back to the ground state at a rate k_e (black, wavy arrow).

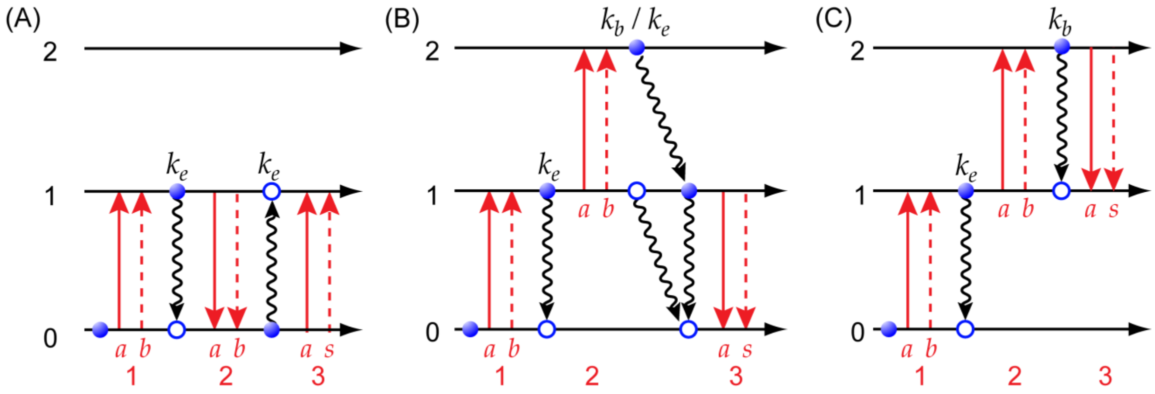

Figure 4.2. Ladder diagrams for MUPPETS in CdSe/ZnS nanoparticles, which can be modeled as a three-level system. Each pulse causes one electric-field interaction (red arrows), and time runs from left to right. Each pair consist of a bra (solid) or ket (dashed) interaction, either in the order shown or reversed. Population changes at each order of interaction are shown as filled (excess) and unfilled (deficit) blue circles. The populations decay (black, wavy arrow) at the rates ke for the exciton and kb for the biexciton. The emitted signal field 3s is heterodyned with pulse 3b. (A) Exciton–exciton pathway. (B) Cross-relaxation pathway. (C) Exciton–biexciton pathway.

The second pair of pulses can have different effects, which are represented in the three diagrams in Figure 4.2. In diagram A, the second pair (2*a* and 2*b*) also acts on the ground-to-exciton transition, but the net effect is to reverse the populations, such that the depletion is now in the excited state, and the excess population is in the ground state. These population changes represent the second-order response of the sample in perturbation theory, i.e., the difference between the two excitations acting in concert and the effect of the two acting independently. The depletion of the ground state by the first pair reduces the bleach induced by the second pair. Thus, the two pairs acting together leaves more population in the ground state and transfers less to the excited state relative to the two pairs acting independently. The $\chi^{(5)}$ response comes from probing this difference.

During the second evolution period τ_2, the population difference again decays at a rate k_e. At the end of this period, a detection pulse (3*a*) is diffracted into a signal field (3*s*, dashed, red arrow). In our experiments, the signal field is heterodyned with the second pulse of the detection pair (3*b*). (In practice, both pulses of the pair are detected, and diffraction in both directions is accounted for.[15] This differential heterodyne detection eliminates artifacts due to propagating the local oscillator through a sample undergoing a time dependent absorption change.)

The dynamics of pathway A are essentially the same as those of a two-level system and have been discussed and demonstrated in several previous studies.[11, 13, 14, 19-21] This pathway detects rate heterogeneity within the sample. For a subensemble of rapidly relaxing particles, the population difference disappears when τ_1 exceeds its lifetime, and this subensemble will not contribute to the final signal. In contrast, subensembles with lifetimes longer than τ_1 will survive until the second excitation. Varying τ_2 measures k_e of this subensemble. A complete measurement of signal versus τ_1 and τ_2 yields the separated dynamics of every kinetic subensemble in the sample or, conversely, reveals the absence of such subensembles. This decomposition is possible even if the kinetics of the individual subensembles are not exponential. Such homogeneous rate dispersion within a subensemble can be caused by a multistep decay mechanism or by relaxation of the environment around the excited state.

In CdSe/ZnS nanoparticles, the radiative contribution to k_e is approximately 20 ns,[93] nearly negligible on the timescale of our experiments, which extends from 1 ps to 2 ns. In an earlier study,[20] we looked at core-only particles, where k_e is dominated by rapid trapping of the conduction-band electron.[94, 95] (That study was confined to times after the biexciton decay, so the particles could be treated as two-level systems.) In the current CdSe/ZnS particles, the shell suppresses this mechanism and enhances the emission quantum yield.[96, 97] Nonetheless, a significant decay of the transient-absorption signal still occurs in less than a nanosecond.[55] This decay could be due to a subset of particles with passivation defects. Pathway A should detect the decay of these particles as a separate kinetic subensemble. Alternatively, one could hypothesize that surface relaxation in response to formation of the exciton is affecting the relaxation kinetics. Such a mechanism would cause homogeneous rate dispersion.

The pathway in Figure 4.2C is a new feature of a multilevel system. The second excitation pair (2*a* and 2*b*) creates a population difference on the exciton–biexciton transition. The exciton population is reduced, and the biexciton is populated. This population difference decays during the second evolution period τ_2 at the biexciton decay rate k_b. (The formalism of ref [66] shifts the subsequent decay across the ground–exciton transition into diagram A, so it does not need to be considered explicitly.)

The third pathway, shown in Figure 4.2B, represents a cross-relaxation from the biexciton transition to the exciton transition during τ_2. Simply summing an exciton decay and a biexciton decay causes a small error. The excitons that are formed from biexciton decay do not begin their decay at $\tau_2 = 0$; their decay should start at approximately the biexciton lifetime. The cross-relaxation pathway is a correction for this error. Its size is approximately proportional to k_e/k_b; it is small when the biexciton decays much faster than the exciton.

In both diagrams A and C, the surviving population is detected as an absorption change resulting from the depletion of one state and the filling of another. The exciton–exciton pathway in Figure 4.2A has an induced absorption due to increased population in the ground state and depletion of the upper state, whereas the exciton–biexciton pathway in Figure 4.2C has an absorption bleach due to increased population in the exciton state and depletion of the biexciton state. Thus, pathways A and C produce signals of opposite sign.

This sign change is useful in distinguishing between the biexciton decay of a normal particle and the exciton decay of a photoproduct. A common way to distinguish between the biexciton and exciton decay of a normal particle is to rely on the much faster decay of the biexciton. However, several experiments—transient absorption,[44, 49, 51, 62, 64, 71] single-particle blinking,[50, 63, 72] and photobleaching[73, 74]—suggest that CdSe nanoparticles have one or more reversible photoproducts with a low quantum yield, and thus, a short lifetime. The spectral shift between the normal exciton and the biexciton is small,[53, 75, 76] and the spectrum of the photoproduct is uncertain. Thus, spectral resolution of the species is difficult. Both the biexciton and a photoproduct have a concentration that scales with the excitation fluence, and so they cannot be distinguished on that basis either.

In our earlier letter, the sign difference between MUPPETS pathways A and C was used to distinguish between these two species.[22] A biexciton decay with a more than five-fold range of rates was observed. For the reasons just discussed, the possibility that the dispersion was an artifact due to a mixed signal from the biexciton and a photoproduct exciton was excluded. Existing theories for biexciton relaxation do not have an obvious means to account for the observed dispersion.

That letter neglected a number of potential complicating factors that are addressed here. Section 4.2 describes the data collection and analysis, including our method for extracting low-fluence limits from complex data. This extrapolation is needed to exclude any contamination of the biexciton signal by higher excitons. Section 4.2 also describes the calibration of the absolute phases of our measurements, which are needed for modeling complex data. Section 4.3 combines the previously reported pump–probe data with new transient-grating data to build a complete model for the 1D kinetics of our sample, including the phases of the exciton and biexciton transitions.

In section 4.1, this model is compared to the $\tau_1 = 0$ MUPPETS data. The phase of MUPPPETS decay varies with time, which is shown to be consistent with the 1D data. The only adjustable factor is the ratio of ground-to-exciton and exciton-to-biexciton cross-sections. This ratio is found to be exactly the value predicted by the generally accepted uncorrelated-electron model. This section demonstrates the self-consistency of our measurements and provides confidence for more advanced analysis.

Section 4.2 revisits the separation of exciton and biexciton dynamics by combining 1D and MUPPET measurements. In contrast to our previous report,[22] which used only signal magnitudes, this analysis uses the full, complex data. In addition, the contribution from cross-relaxation, which was neglected before, is considered here. Fortunately, adding these features does not change our previous conclusions.

Our previous letter[22] used and section 4.4 of this paper uses only the $\tau_1 = 0$ cut through the 2D MUPPETS data. Section 4.5 analyzes MUPPETS data in the full τ_1–τ_2

plane. The pathway in Figure 4.2C is sensitive to correlations between the dynamics of the exciton and the biexciton decay. The first evolution period τ_1 filters the molecules based on their exciton decay rate; the second evolution period τ_2 measures the biexciton decay of the subensemble surviving this filter. If the decay mechanisms of the exciton and biexciton are fully independent, no correlation exists, and the value of τ_1 will have no effect on the decay with τ_2. Correlations can be created by a feature common to both decay mechanisms, whether those mechanisms are heterogeneous or homogenous. For example, if a surface defect on a subset of particles accelerates both exciton and biexciton decay, there will be correlated, heterogeneous kinetics. Alternatively, if there is a surface relaxation of the excited particle that affects both the exciton and biexciton, there will be correlated homogeneous kinetics. Reference [66] has a more in-depth discussion of the nature of rate correlations.

The full MUPPETS data is also sensitive to heterogeneity in the exciton decay. The data set is compared to several models to show that it should have enough sensitivity to resolve both effects. We find no correlation between the exciton and biexciton decays, which is in line with expectations, but also find no heterogeneity of the exciton decay, which is unexpected. Section 4.6 discusses these findings.

4.2 MEASURING COMPLEX ABSORBANCES

The apparatus used to generate the pulse configuration of Figure 4.1 has been describe in detail in other publications.[18, 21] Briefly, ultrafast pulses at 527 nm were generated by summing the output of a white-light-seeded optical parametric amplifier with 800 nm pulses from a 1 kHz amplified Ti:sapphire laser. Pulse energies are reported as the energy in one excitation pulse at the sample. The beam diameter in the sample was approximately 200 µm. All pulses had equal energies, except in the 2D experiments, where the probe pair was attenuated by a factor of ten. The same apparatus was used for pump–probe, 1D-transient-grating and 2D-MUPPETS measurements by blocking and unblocking the appropriate beams.[21] The pulse was dispersion broadened to ~300 fs at the sample. To avoid the complications of fast intraband relaxation, results are not reported below 1 ps. No effort has been made to improve or correct for the pulsewidth. Differential detection is used to eliminate the bleaching signal from the chopped beam (1*a*).[15]

The sample consisted of CdSe nanoparticles with a ZnS shell and octadecylamine surfactant (NN-Labs) dissolved in toluene. The particles had a well-resolved band-edge peak at 520 ± 10 nm (4.2 nm diameter) [Figure C1 in the Appendix C]. The concentration was adjusted so the absorbance at this peak was OD = 0.4 ($A'^{(0)} = 0.9$) in the 1 mm sample cuvette. To minimize the role of photoproducts, the sample was flowed through the cuvette with a peristaltic pump. The sample was kept under a dry, N_2 atmosphere.

All measurements made here; pump–probe, transient-grating and MUPPETS; are heterodyned measurements and are reported as a generalized, base-*e* absorbance $A^{(N)}$:[18]

$$A^{(N)} = \frac{(-1)^N}{\pi} \int_0^{2\pi} e^{-i\Phi} \left[\frac{-\delta I_{\mathrm{lo}}(\Phi)}{\left(I_{\mathrm{lo}} I_{\mathrm{pr}}\right)^{1/2}} \right] d\Phi \qquad (103)$$

The number of excitations is N: $N = 2$ for MUPPETS, $N = 1$ for pump–probe and transient-grating experiments, and $N = 0$ for static absorbance. The change in the local-oscillator energy I_{lo} due to interaction with the probe pulse of energy I_{pr} is δI_{lo}. The phase difference between the local oscillator and the probe is Φ. In general, this absorbance is complex, with the real part representing energy loss (absorption) and the imaginary part representing phase delay (index-of-refraction). The results will usually be given as the magnitude and phase of the absorbance. If the phase has a weak time dependence, the magnitude tracks changes in population, while the phase reflects changes in the spectral shape. This generalized absorbance reduces to the static, base-*e* absorbance when $N = 0$. Pump–probe experiments measure the real part of the $N = 1$ absorbance $A'^{(1)}(\tau_1)$.

Complex signals are susceptible to misinterpretation if data are collected at only one or two phases.[18] Analyzing such data requires the phase of the signal to be time independent, which is not generally true. Here, a complete phase dependence is collected by "phase cycling" Φ through a full 360° (Figure 4.3A). A Fourier analysis yields real, imaginary and DC components (Figure 4.3B).[18] The DC component consists of artifacts (primarily unbalanced bleaching of the probe beams[21]) and is discarded. The real and imaginary parts give the correct magnitude and relative phase versus time, but

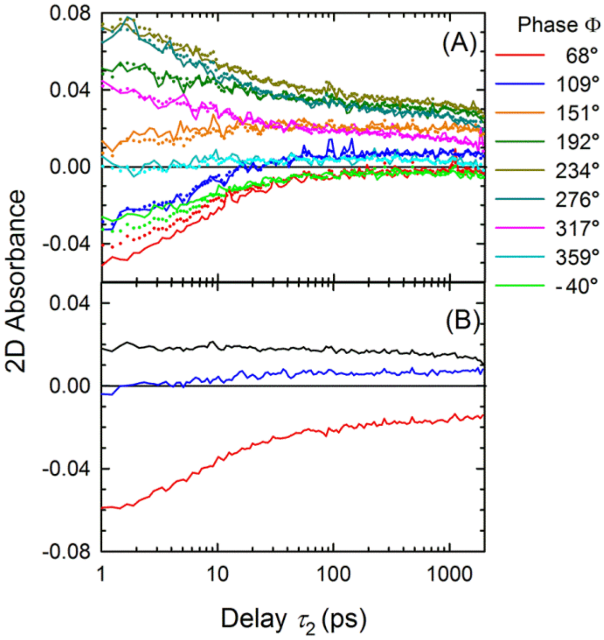

Figure 4.3. Extracting a complex absorbance from a phase-dependent signal. (A) MUPPETS absorbance versus phase Φ, $A^{(2)}(\tau_2, 0; \Phi)/A'^{(0)}$, for 11.7 nJ pulses with $\tau_1 = 0$ (solid). (B) Fourier decomposition of the data in (A) yields cosine (red), sine (blue) and DC (black) components.[18] Reconstructing the data in (A) from the components in (B) gives the dots shown in (A). The cosine and sine components must be rotated to the correct absolute phase to obtain the real and imaginary parts of the absorbance (see Figure 4.8A—B). Also see Figure C2 in the Appendix C.

the entire phase trace is shifted by an arbitrary constant. The size of the signal ($|A^{(2)}(0, 0)|/A'^{(0)} = 0.06$) in this example suggests that approximately 6% of the particles contribute effectively to the MUPPETS signal at this fluence, i.e., 6% interact with all six fields. (See Figure A in the Appendix C for a similar example of transient-grating data.)

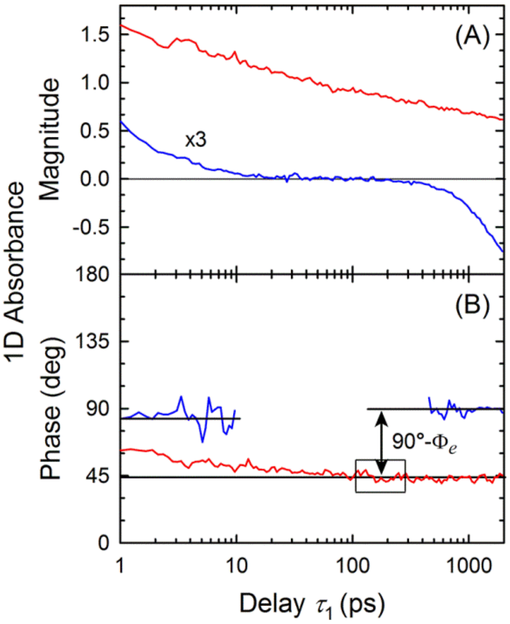

Figure 4.4. Calibration of the absolute phase with an external standard. The transient-grating signals $A^{(1)}(\tau_1)$ of azulene in toluene (blue) and CdSe/ZnS in toluene (red) were measured contemporaneously and with the same excitation energy (10.6 nJ/pulse): (A) magnitudes (azulene magnified three times) and (B) phases. The azulene phase at late times is due to a purely nonresonant thermal effect and has a known phase of 90°. (The phase at early times is fortuitously near 90°.) The absolute phase for all CdSe measurements in the 100–300 ps range, $\Phi_e = 44°$, was determined from this measurement by the phase difference shown in black. The magnitudes are used in chapter 5 to measure the thermal cross-section (see Figure 5.7).

Knowing the absolute phase of the signal is important for comparing pump−probe and heterodyned signals and for detecting thermal-grating contributions to the signal. A small correction to the differential-detection signal also requires knowledge of the absolute phase.[15] (The value of this phase is not easy to predict or interpret. It measures the size of the nonresonant response of the transition, which is an integral of absorbance changes over a broad frequency range.) The phase was calibrated by comparing CdSe measurements with an external standard, azulene in toluene, measured on the same day (Figure 4.4). The excited state of azulene decays nonradiatively within a few picoseconds. The released heat causes a thermal grating to develop,[48, 98] and its signal builds to a maximum near the end of the scan.

The azulene signal was assumed to be a purely nonresonant (90°) thermal grating after 300 ps. [The signal during the first few picoseconds is also nearly nonresonant (83°) at this wavelength because of cancellation of the absorption bleach by excited-state absorption.[99]] The absolute phase of the contemporaneous CdSe measurement is then known. The data presented below will show that during the time before 100 ps, both excitons and biexcitons are present. After 300 ps, the potential for a thermal contribution must be considered. Between 100 and 300 ps, only the exciton contributes to the signal, and its phase is constant. Thus, the measured phase of CdSe in this range, $\Phi_e = 44°$, was transferred to all other CdSe measurements. A correction for a small difference in sensitivity to real and imaginary signals was then applied.[15] All phase measurements in this paper are on this absolute scale.

Pump−probe measurement of nanoparticles are known to be sensitive to the excitation fluence at short times,[52, 54, 55, 100, 101] and all of our data show the same sensitivity. To characterize the fluence dependence, we made measurements over a range of low to moderate fluences *I*. Similar pump–probe data are typically normalized to the same size at long times. We extended this procedure by normalizing our complex decays at an intermediate time τ_I:

$$\overline{A}^{(1)}(\tau_1;I) = \frac{A^{(1)}(\tau_1;I)}{A^{(1)}(\tau_I;I)} e^{i\Phi_e} C_{1'}(\tau_I) \qquad (104)$$

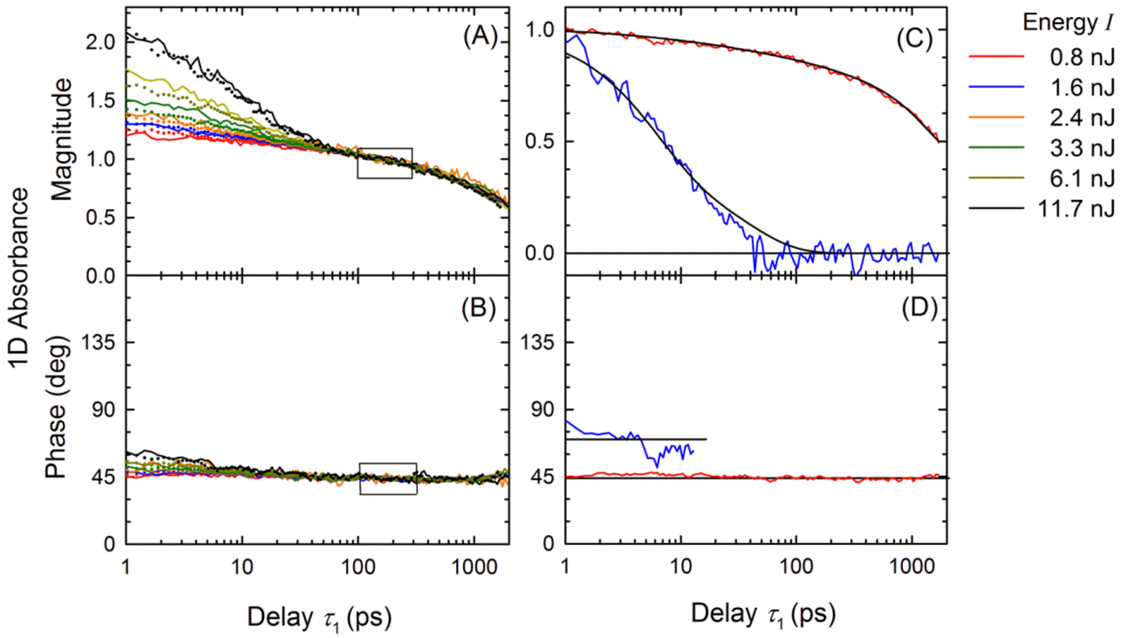

Figure 4.5. Normalization of heterodyned results versus fluence (left) and their decomposition into low-fluence and fluence-induced components (right) illustrated using transient-grating results. (A–B) Solid curves: The absorbances at various pump energies I have been matched in magnitude and phase at intermediate times (boxes, eq 104) to give $\overline{A}^{(1)}(\tau_1;I)$. Dots: Values reconstructed from the reduced results in (C–D). (C–D) Linear regression at each delay time reduces the data in (A–B) to two components: a low-fluence component $A_0^{(1)}(\tau_1)$ (red) and a fluence-induced component $A_1^{(1)}(\tau_1)$ (blue). Black: Fits to eqs 107 and 108 in (C) and to Φe = 44° and Φ12 = 67° in (D). A similar method is used for the MUPPETS data (Figure 4.8).

and

$$\overline{A}^{(2)}(\tau_2,\tau_1)=\frac{A^{(2)}(\tau_2,\tau_1)}{A^{(2)}(\tau_I,\tau_1)}e^{i\Phi_e}C_{1'1'}(\tau_I,\tau_1) \tag{105}$$

Because thermal signals can contribute at long times (see chapter 5), the region for normalization was chosen to be τ_I = 100–300 ps. As discussed above, only the exciton contributes to the signal in this region. The first terms in eqs 104 and 105 match the magnitudes and phases of the scans at τ_I. The complex exponential rotates the phase to its absolute value using the value of Φ_e found in Figure 4.4. The normalized correlation functions that describe the material relaxation, $C_{1'}(\tau_1)$ and $C_{1'1'}(\tau_2, \tau_1)$, are described more completely later in the paper. Their values at τ_I renormalize the signals to one at time zero. (The final renormalization with these factors, as shown in the figures, is only possible after $C_{1'}(\tau_1)$ and $C_{1'1'}(\tau_1, \tau_1)$ have been fit.) This procedure normalizes the scans to the same number of ground-to-exciton transitions. It corrects for saturation of the ground-to-exciton transition and depletion of the exciton by additional excitation to the biexciton. An example of this normalization is shown in Figure 4.5A–B.

Separate Linear regression of the real and imaginary components of the normalized data yield intercepts and slopes. We will call the intercepts, $A_0^{(1)}(\tau_1)$ and $A_0^{(2)}(\tau_2, \tau_1)$, the low-fluence components. Although they contribute to the signals at all fluences, they represents the extrapolated shape of the decay at zero fluence. We will call the slopes, $A_1^{(1)}(\tau_1)$ and $A_1^{(2)}(\tau_2, \tau_1)$, the fluence-induced components. They represent the processes that give rise to the fluence dependence of the total signal. (See sections 2.2 and 2.3 of chapter 5 for more detail.) An example using transient-grating results is shown in Figure 4.5. (Also see Figure 4.8 below.) To check the validity of the linear regression, the original data scans were regenerated from $A_0^{(1)}(\tau_1)$ and $A_1^{(1)}(\tau_1)$. The results are shown as dots in Figure 4.5A–B. Deviations were typically dominated by small errors in the excitation energy of an entire scan. Deviations systematic with excitation energy due to higher-order saturation terms were not detected.

4.3 1D KINETICS

4.3.1 Pump–Probe Results.

Transient-absorption measurements of the band-edge in CdSe/ZnS core–shell nanoparticles have been reported several times in the past.[64, 94, 100] Fluence-induced measurements on our samples were reported in ref [22] and are repeated in Figure 4.6. The results at various pulse energies (Figure 4.6A) are decomposed into a low-fluence component and a linear fluence-induced component (Figure 4.6B). The decomposition is by linear regression as describe in section 4.2, so there are no assumptions about the forms of the two decays. The moderate amplitude decay dispersed over the subnanosecond range is a common feature of both transient absorption and photoluminescence at low fluence.[55, 64, 94, 101, 102] The change in the decay over the first 100 ps with increasing fluence has also been seen previously with either technique and either with[55] or without[52, 54, 55, 100, 101] a ZnS shell.

These data can be interpreted using the simple, standard model for the CdSe nanoparticle band edge shown in Figure 4.7A.[43] The ground state 0 is excited to a doubly degenerate exciton level 1. The complex transition cross-section to an individual exciton state is σ_{01}, so the total absorption to the doubly degenerate level is $2\sigma_{01}$. Relaxation within the exciton fine structure (including additional dark states) is fast relative to our time range,[68, 91] so the exciton can be regarded as a single kinetic level. However, this relaxation greatly reduces the emission cross-section,[43] so stimulated emission from the exciton and biexciton will be neglected. The exciton can be further excited to a biexciton state 2 with a transition cross-section σ_{12}. Because absorption can only come from a single initial state, the net absorption cross-section from the exciton is σ_{12}. In the uncorrelated-electron model, the state-to-state cross sections are equal: $\sigma_{01} = \sigma_{12}$. Thus, the band-edge absorption is reduced by approximately one-half when the exciton is excited and is eliminated entirely when the biexciton is formed. In CdSe, the biexciton-to-triexciton transition requires more energy than these transitions do. With band-edge excitation, higher excitons should not be formed.

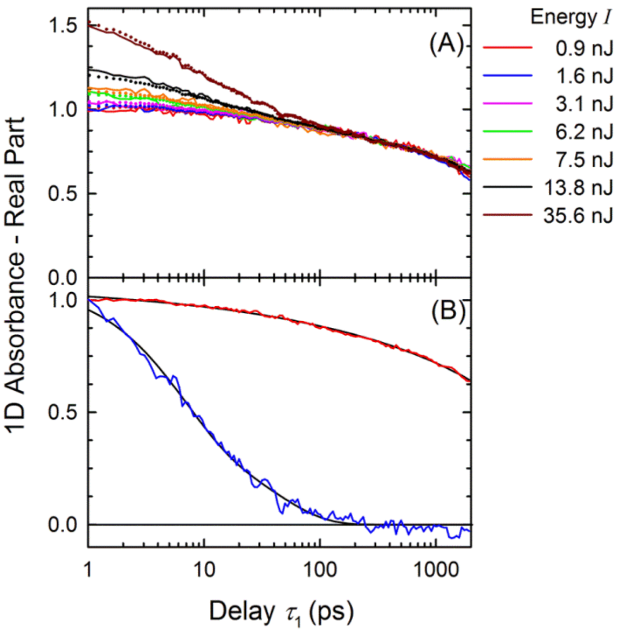

Figure 4.6. Decomposition of pump–probe results versus pulse energy I into low-fluence and fluence-induced components. (A) Solid curves: The normalized absorbance $\overline{A}'^{(1)}(\tau_1; I)$ at various pulse energies. An additional four energies are not shown to improve clarity (see ref [22]). Dots: Values reconstructed from the reduced components in (B). (B) The low-fluence $A_0'^{(1)}(\tau_1)$ (red) and fluence-induced $A_1'^{(1)}(\tau_1)$ (blue) components of the data in (A). Black: Fits to eqs 106 and 107. (Adapted from ref [22].)

The dynamics of this model are described by two primary correlation functions: $C_{1'}(\tau)$, which describes the decay of the exciton to the ground state, and $C_{2'}(\tau)$, which describes the decay of the biexciton. (The primes indicate a change of basis state so the functions refer to population differences.[66] Thus, $C_{2'}(\tau)$ include the decay of a biexciton to an exciton, but not the subsequent decay of the product exciton to the ground state.)

The low-fluence component of the pump–probe data $A_0'^{(1)}(\tau_1)$ (Figure 4.6B) is assigned to the exciton decay. For modeling purposes, an empirical fit was made to

$$A_0'^{(1)}(\tau_1) = C_{1'}(\tau_1) = \left\{0.635\exp\left[-\left(\tau_1/4.9\text{ ns}\right)^{0.31}\right] + 0.365\right\} \times\exp\left(-\tau_1/20\text{ ns}\right) \tag{106}$$

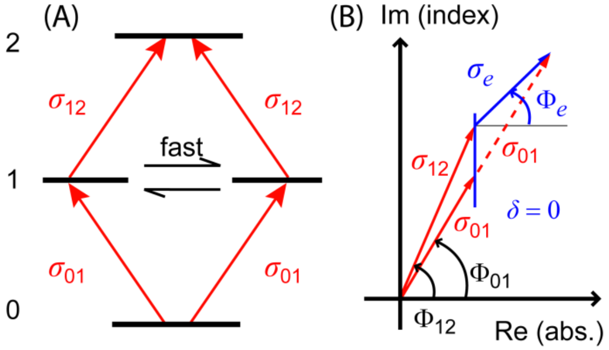

Figure 4.7. The complex cross-sections for the CdSe/ZnS model. (A) The exciton state 1 is doubly degenerate with rapid equilibration. Two complex absorption cross-sections (red), σ_{01} and σ_{12}, apply to the ground-to-exciton (0-to-1) and exciton-to-biexciton (1-to-2) transitions, respectively. (B) The cross-sections (red) represented on the complex plane are converted to practical parameters (blue). The ratio of real parts of the cross sections is measured by δ (eq 110). The phases of the two transitions are Φ_{01} and Φ_{12}. The phase Φ_{01} is not directly observed. Instead, the population in the exciton state is detected at the phase Φ_e (eq 111). The combined 1D and MUPPETS data are fit to $\delta = 0$ ($\sigma'_{01} = \sigma'_{12}$), $\Phi_{12} = 67°$, and $\Phi_e = 44°$ ($\Phi_{01} = 59°$).

The final factor represents the radiative decay; the factor in curly brackets is the nonradiative decay.

The fluence-induced component in Figure 4.6B is also distinctly nonexponential. It has been fit to a biexponential:

$$A_1'^{(1)}(\tau_1) = 0.635\exp\left(-\tau_1/6\text{ ps}\right) + 0.365\exp\left(-\tau_1/40\text{ ps}\right) \tag{107}$$

It is equally consistent to assume a continuous distribution of decay times. For example, a rate spectrum shows a five-fold variation of rates at the half-width.[22]

These fits highlight the issues that will be addressed in this paper. The first is the origin of the highly dispersed, nonradiative decay at low fluence (eq 106). CdSe nanoparticles without a shell have a low quantum yield and substantial subnanosecond, nonradiative decay,[20, 64, 94, 95, 103, 104] which is attributed to trapping of the excited electron at the unpassivated surface.[94, 95] This decay is highly dispersed, and MUPPETS measurements showed that the rate dispersion is due to particle-to-particle variation in the electron-trapping rate.[20]

The nonradiative decay is distinctly different with a ZnS shell, which acts to passivate surface traps. Both hole and electron trapping rates are greatly reduced, increasing the quantum yield of luminescence. Nonetheless, a significant drop in signal (40% in the observed time range, 63% extrapolated from the fit in eq 106), dispersed over the 1 ps to 2 ns time range, still occurs (Figure 4.6). A similar drop in luminescence intensity is seen, even in well prepared, high quantum-yield samples.[55] This drop could be assigned to electron trapping to residual passivation defects. The form of the fit used in eq 106—a stretched exponential plus a constant—is arbitrary, but it is consistent with a subensemble of well passivated, high quantum-yield dots represented by the constant along with a set of lower quantum-yield dots with a broad distribution of nonradiative relaxation rates due to a variety of passivation defects. In this case, the rate dispersion is heterogeneous. Alternatively, the dispersion may be due to relaxation of the particle or its surface in response to creating the exciton. In this scenario, the dispersion is homogeneous. MUPPETS measurements in section 4.5 will determine if the exciton decay is homogeneous or heterogeneous.

The second issue is the cause of the dispersion in the fluence-induced component (eq 107). This decay has conventionally been assigned to Auger relaxation of biexcitons.[43, 52, 54, 69] However, this mechanism, in its basic form, predicts an exponential decay. In previous measurements, rate dispersion has been attributed to the creation of higher excitons with faster relaxation rates.[52, 54] In fact, the presumption of exponential decay has been used isolate the biexciton signal.[52, 54] Following this reasoning, the 40 ps component of $A_1'^{(1)}(\tau_1)$ is the biexciton decay, and the 6 ps component is a triexciton decay. However, unlike many previous experiments, we use band-edge excitation. Because the band edge is completely bleached upon forming a biexciton, we do not expected to create higher excitons. This expectation will be confirmed by the MUPPETS measurements, both at low fluence in section 4.1 below and at high fluence in section 2.4 of chapter 5.

More recently, it has been recognized that a long-lived photoproduct with a fast exciton lifetime, for example, a charged nanoparticle, could also contribute to this signal.[44, 51, 62] The fit in eq 107 is also consistent with the hypothesis that the dispersed decay is due to a combination of two exponential decays, one from the biexciton and another from a photoproduct. In a letter using initial data, we claimed that comparing MUPPETS and pump-probe data excluded this idea.[22] The more detailed discussion of the full data set in section 4.2 confirms that claim.

The third issue is whether the two decays in Figure 4.6B are both dispersed for the same reason. This type of kinetic correlation can be detected by the MUPPETS measurements presented in section 4.5. The simplest possibility is that there are two types of particle: one responsible for the fast component of both eqs 106 and 107; the other responsible for both slow components. The fits in eqs 106 and 107 were chosen to allow consideration of this simple type of correlation; each has two components with equal amplitudes. Neither fit is unique, and the components of these fits should not be assumed to represent distinct physical processes without further evidence.

4.3.2 Transient-Grating Results.

One-dimensional transient-grating measurements on the same sample are shown in Figure 4.5. (Also see Figure C2 in the Appendix C.) Unlike the previously reported pump–probe results,[22] these new transient-grating measurements give a complex absorbance. The real part should be identical to the pump−probe measurements. The addition of the imaginary part allows the phase of the absorbance to be measured, which will be important for interpreting the complex MUPPETS data. The imaginary part of the absorbance may also contain thermal effects, which are not present in pump–probe measurements. That possibility will be ignored until chapter 5.[79]

The phase of the transient-grating data is time-dependent, and both the magnitude and phase vary with fluence (Figure 4.5A–B). After these data are decomposed into low-fluence and fluence-induced components (Figure 4.5C–D), the phase of each component is constant with time. The apparent dependence on time and fluence in the original data is only due to the changing ratio of these two components as they decay at different rates. The constant phases in Figure 4.5D suggest that the decomposition is cleanly separating two distinct processes.

The magnitude of the low-fluence component (Figure 4.5C) is fit by

$$\left|A_0^{(1)}(\tau_1)\right| = \left\{0.635\exp\left[-\left(\tau_1/1.9\text{ ns}\right)^{0.54}\right]+0.365\right\} \times\exp\left(-\tau_1/20\text{ ns}\right) \tag{108}$$

The magnitude of the fluence-induced component $\left|A_1^{(1)}(\tau_1)\right|$ is well matched by the fit to the fluence-induced pump–probe data (eq 107, Figure 4.5C).

Many ways to represent complex signals have been used since transient-grating spectroscopy was developed.[24-26, 41, 46, 80] We find that complex absorbances and cross-sections are intuitive and extend well to higher dimensions.[18] The CdSe/ZnS model is characterized by two complex cross-sections, σ_{01} and σ_{12} (Figure 4.7A). For fitting experimental data, it is useful to introduce a practical set of four real quantities. Two are simply the phase Φ_{12} and real part σ'_{12} of the exciton-to-biexciton cross-section σ_{12}

$$\sigma_{12} = \frac{\sigma'_{12}}{\cos\Phi_{12}}e^{i\Phi_{12}} \tag{109}$$

In the uncorrelated-electron model, $\sigma'_{01} = \sigma'_{12}$. (The imaginary parts are strongly influenced by transitions away from the band-edge and are more difficult to predict.) Thus, we introduce δ

$$\delta = 1-\frac{\sigma'_{12}}{\sigma'_{01}} \tag{110}$$

which measures the deviation from this model, as the third fitting parameter. The ground-to-exciton cross-section σ_{01} never appears by itself in the fitting. Population of the exciton always causes a combination of a bleach of this transition along with increased absorption on the exciton-to-biexciton transition. Thus, we define an exciton cross-section σ_e by

$$\sigma_e = 2\sigma_{01} - \sigma_{12} = |\sigma_e| e^{i\Phi_e} \tag{111}$$

The phase of this cross-section Φ_e is the fourth and final fitting parameter. The relationship between these quantities is illustrated in Figure 4.7B.

A theoretical analysis of the fluence dependence of the complex absorbance in chapter 5 yields the following expressions in terms of these parameters:[79]

$$A_0^{(1)}(\tau_1) = e^{i\Phi_e} C_{1'}(\tau_1) \tag{112}$$

and

$$A_1^{(1)}(\tau_1) = e^{i\Phi_{12}} C_{2'}(\tau_1) + e^{i\Phi_e} \frac{\cos\Phi_{12}}{\cos\Phi_e} \frac{1+\delta}{1-\delta} C_{1'}^{2'}(\tau_1) \tag{113}$$

Taking the real parts of these equations serves to interpret the pump–probe data (eqs 106 and 107). Although the biexciton decay $C_{2'}(\tau_1)$ is detected with the phase of the exciton-to-biexciton transition Φ_{12}, the exciton decay $C_{1'}(\tau_1)$ is not detected at the phase of the ground-to-exciton transition Φ_{01}. As anticipated above, it is detected at Φ_e defined in eq 111. The cross-relaxation function $C_{1'}^{2'}(\tau_1)$ represents the process shown in Figure 4.2B.[66] It accounts for a delay in the decay of excitons that are created by the decay of biexcitons and is expected to be small (see section 4.5 and Figure 4.9 below).

To interpret the MUPPETS data, complete models for the cross-sections and 1D kinetics are needed. Initial models are developed by neglecting various potential complications, including cross-relaxation, thermal effects and photoproducts. As the data is analyzed, each of these effects will be shown to be minor, so no further refinement will be needed. Equation 112 shows that the phase of $A_0^{(1)}(\tau_1)$ (Figure 4.5D) is $\Phi_e = 44°$.

Neglecting cross-relaxation, eq 113 shows that the phase of $A_1^{(1)}(\tau_1)$ (Figure 4.5D) is $\Phi_{12} = 67°$. Determining the value of δ requires $\tau_1 = 0$ MUPPETS data (section 4.1). Again neglecting cross-relaxation in eq 113, the fit in eq 107 is used for the biexciton decay $C_{2'}(\tau_1)$. With a time-independent phase, eqs 106 and 108 should be identical and both should represent the exciton decay. Section 4.3 in chapter 5 discusses this discrepancy. For the current model, eq 106 is used for $C_{1'}(\tau_1)$.

4.4 ANALYSIS OF COMPLEX MUPPETS DATA

In our earlier letter, the phase of the MUPPETS signal was not considered.[22] With the addition of the transient-grating data and the full model of the complex 1D signal from section 4.3, an analysis of the complex MUPPETS signal will be carried out in this section. The effects of cross relaxation will also be considered. Two issues are primary and are dealt with in two subsections. In subsection 4.1, the MUPPETS signal, including its time-dependent phase, is shown to be consistent with the 1D data. The fitting will yield the ratio of cross-sections for the exciton and biexciton transitions. In the earlier letter, the difference between the MUPPETS magnitude and the real pump–probe signal was presented as a measure of the biexciton decay.[22] In subsection 4.2, the difference of complex 1D and 2D signals is taken to obtain the complex biexciton signal. Both topics require only the $\tau_1 = 0$ cut through the MUPPETS data. The full τ_1–τ_2 dependent data are discussed in section 4.5.

4.4.1 Measuring Exciton and Biexciton Cross-Sections.

A key result from the theoretical analysis of MUPPETS in excitonic systems is that exciton–exciton (Figure 4.2A) and exciton–biexciton (Figure 4.2B) pathways have opposite signs.[66] Because the biexciton decay is faster than the exciton decay, the total signal along τ_2 should initially rise as the negative biexciton signal decays.

Experimental MUPPETS data with $\tau_1 = 0$ are shown in Figure 4.8. The raw, phase-cycled data are reduced to a complex signal (Figure 4.3). The results for different excitation fluences have been normalized according to eq 105 and are shown in Figure 4.8A–B. There is a strong fluence dependence to the shape of the signals, with the predicted rise of the signal seen only at the lowest fluences. This behavior will be explained in section 5.2 of chapter 5.[79] For now, we focus on the low-fluence limit. Because the signal-to-noise ratio deteriorates as this limit is approached, it is particularly important to extrapolate to zero fluence. Results are shown in Figure 4.8C–D (red). The measured decay with the lowest fluence is similar to the extrapolated low-fluence signal $A_0^{(2)}(\tau_2, 0)$. This component has a delayed maximum in the magnitude, as expected, but it also has a time-dependent phase that must be explained.

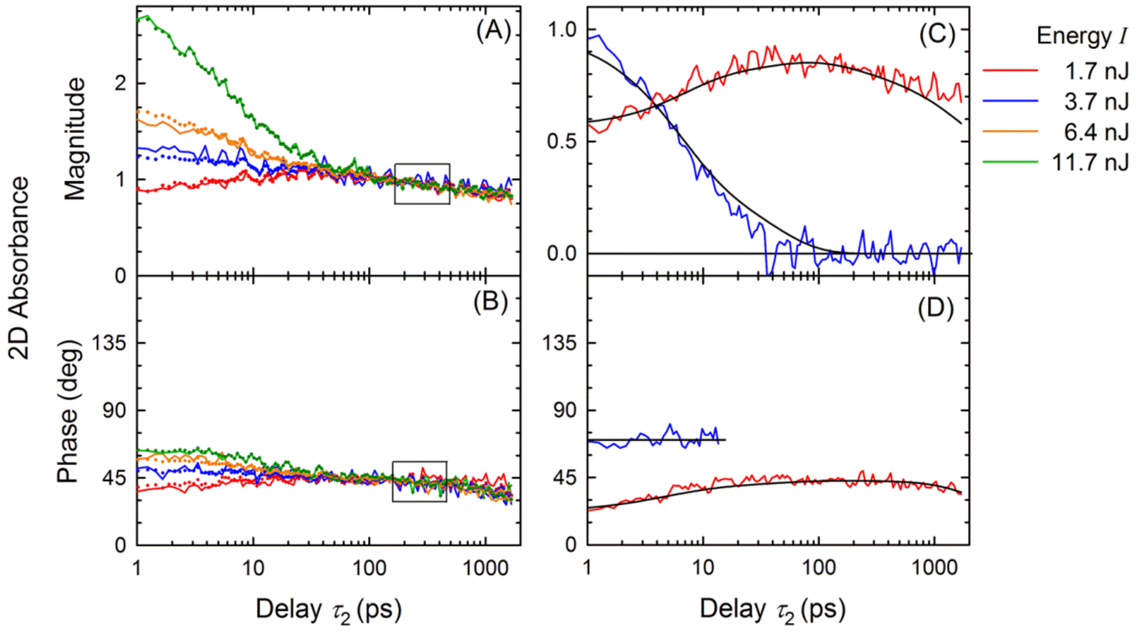

Figure 4.8. MUPPETS $\tau_1 = 0$ results. Decomposition of the signal versus pulse energy I (left) into low-fluence and fluence-induced components (right). (A–B) Solid curves: The normalized absorbance $\bar{A}^{(2)}(\tau_2,0;I)$ at various pump energies. Dots: Values reconstructed from the reduced results in (C–D). (C–D) The low-fluence $A_0^{(2)}(\tau_2,0)$ (red) and fluence-induced $A_1^{(2)}(\tau_2,0)$ (blue) components of the data in (A–B). Black: Fits to eq 114 and to eq II.168 with δ = 0.

Unlike 1D measurements, the biexciton contribution is intrinsic to MUPPETS, even in the low-fluence limit. Moreover in this limit, the ratio of these two contributions is fixed by the cross-sections of the chromophore. The theoretical expression for the complex, low-fluence MUPPETS absorbance with $\tau_1 = 0$ is

$$\begin{aligned} A_0^{(2)}(\tau_2,0) = {} & e^{i\Phi_e} C_{1'}(\tau_2) - \tfrac{1}{2} e^{i\Phi_e}(1-\delta) C_{1'}^{2'}(\tau_2) \\ & - \tfrac{1}{2} e^{i\Phi_{12}} \frac{\cos\Phi_e}{\cos\Phi_{12}} \frac{(1-\delta)^2}{1+\delta} C_{2'}(\tau_2) \end{aligned} \tag{114}$$

The results of ref [66] have been adapted to the CdSe system defined in Figure 4.7. The exciton $C_{1'}(\tau_2)$ and biexciton $C_{2'}(\tau_2)$ contributions dominate the signal. In the simplest case of $\sigma_{01} = \sigma_{12}$ ($\delta = 1$ and $\Phi_e = \Phi_{12}$), the biexciton contribution is exactly one-half the exciton signal. However, the 1D spectroscopy has already indicated that these phases are unequal, so a more detailed approach is needed.

The $\tau_1 = 0$ cut of the MUPPETS data is almost entirely determined by quantities measured by 1D experiments. Most of the quantities in eq 114 have already been found in section 4.3: Φ_e, $C_{1'}(\tau_2)$, Φ_{12}, and $C_{2'}(\tau_2)$. The only undetermined quantity is δ. A fit to eq 114 with $\delta = 0$ is shown in Figure 4.8C–D (red). The cross-relaxation $C_{1'}^{2'}(\tau_2)$ is small, but has been included (see eq 120 below). This value correctly reproduces the size of the peak in the magnitude. It simultaneously reproduces the time dependence of the phase. The phases of the individual transitions are constant; the time dependence of the total signal is due to the changing ratio of the different pathways in Figure 4.2. The consistency of the 1D and MUPPETS results increases our confidence in both the theory and the data. Knowing that $\delta = 0$, i.e., $\sigma'_{01} = \sigma'_{12}$ (eq 110), the previously known values of Φ_{12} and Φ_e allow us to calculate that $\Phi_{01} = 59°$ (see Figure 4.7).

A zero value for δ is predicted by the uncorrelated-electron model, which has been widely used to interpret results in CdSe nanoparticles.[43] However, Franceschetti and Zhang have suggested that electron correlation causes strong deviations in the cross-sections that can lead to misinterpretations of fluence-induced data.[105] They calculated $\delta = 1/3$ at 300 K. It should be noted that there is a small, but non-negligible, shift between the ground–to–exciton and exciton–to–biexciton transitions. Our pulses have a wide bandwidth (see Figure C1 in the Appendix C), but any failure to cover both transitions equally would introduce a systematic error in our measurement of δ, which is defined by spectrally integrated cross-sections. We have also neglected any simulated emission from either the exciton or biexciton. Detailed calculations including stimulated emission (unpublished) show no new effects other than to perturb the effective cross-sections and, thus, to alter the measured value of δ. However, stimulated emission is known to be small and red-shifted from the band edge.[49, 71] Even recognizing these limitations, our results do not support a strong electron-correlation effect on the cross-sections. Overall, the agreement between 1D measurements and MUPPETS at $\tau_1 = 0$ paves the way for analysis of the full MUPPETS data in sec 4.5.

4.4.2 Separating Biexcitons from Long-Lived Photoproducts.

We also need to consider the possibility that the excitation produces not only excitons and biexcitons, but also creates a long-lived, reversible photoproduct that builds up a steady-state population in the sample. The exciton lifetime of the photoproduct is assumed to be short and, thus, easily confused with the biexciton lifetime of the normal particles. Two possibilities are a concern. The first is that the photoproduct is produced at high fluences, similar to those needed to create the biexciton, and as a result, the photoproduct will contribute to the fluence-induced components of our signals. The second possibility is that the photoproduct accumulates even at low fluences, so that our nominally low-fluence components still contain a photoproduct contribution. To model both possibilities, the total exciton decay $C_{1'}(\tau)$ is written as sum of contributions from the normal species $C_{1',n}(\tau)$ and the photoproduct $C_{1',p}(\tau)$

$$C_{1'}(\tau) = C_{1',n}(\tau) + \left(\alpha + I\sigma'_p\right)C_{1',p}(\tau) \tag{114}$$

The fraction of photoproduct at low fluence is α. The fluence-induced increase in photoproduct concentration is given by σ'_p, an effective cross-section, and I, the average excitation fluence. The photoproduct concentration is always taken to be small enough to be treated perturbatively.

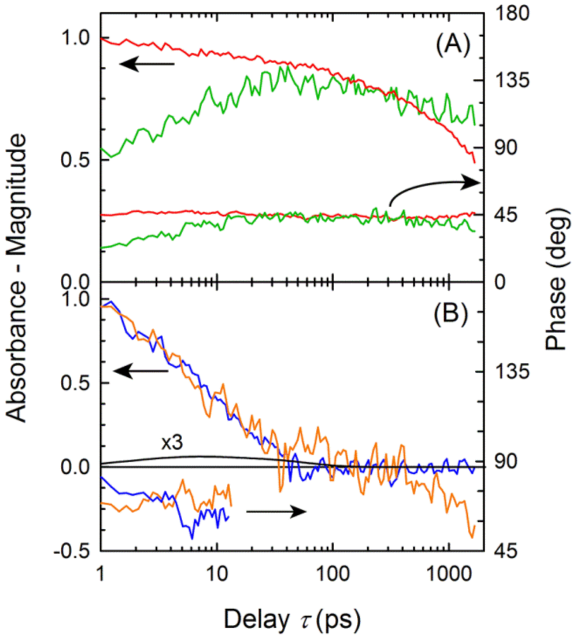

Figure 4.9. Deriving the biexciton signal. The low-fluence, $\tau_1 = 0$ MUPPETS signal $A_0^{(2)}(\tau,0)$ [(A) green, from Figure 4.8C–D] is subtracted from the low-fluence transient-grating signal $A_0^{(1)}(\tau)$ [(A) red, from Figure 4.5C–D] to yield the biexciton signal $A_b(\tau)$ [(B) orange] (see eq 115). The biexciton signal is compared to the fluence-induced transient-grating signal $A_1^{(1)}(\tau)$ [(B) blue, from Figure 4.5C–D] to show that a fast relaxing photoproduct is not present (eq 118). The calculated cross-relaxation term $C_{1'}^{2'}(\tau)$ (eq 120, black, magnified three times) is negligible.

Because the biexciton and exciton signals have opposite signs in MUPPETS, ref [22] argued that the difference of the real pump–probe signal and the MUPPETS magnitude would eliminate exciton signals (including photoproduct excitons) and leave only the biexciton decay. Here, we more precisely define a “biexciton” signal $A_b(\tau)$ as the difference of complex absorbances

$$A_b(\tau) = 2\frac{\cos\Phi_{12}}{\cos\Phi_e}\frac{1+\delta}{(1-\delta)^2}\left(A_0^{(1)}(\tau) - A_0^{(2)}(\tau,0)\right) \tag{115}$$

The 1D and 2D low-fluence absorbances were originally normalized to the exciton populations as described by eq 104 and 105; the constants in eq 115 renormalize the biexciton signal to one at time zero. Experimental results using the transient-grating data for $A_0^{(1)}(\tau)$ are shown in Figure 4.9.

The theoretical expression for the biexciton signal is derived by putting eq 114 into the original expression for the absorbance, normalizing according to eqs 104 and 105, analyzing the fluence dependence and subtracting according to eq 115 to give

$$A_b(\tau) = e^{i\Phi_{12}}C_{2'}(\tau) + e^{i\Phi_e}\frac{\cos\Phi_{12}}{\cos\Phi_e}\frac{1+\delta}{1-\delta}C_{1'}^{2'}(\tau) \tag{116}$$

The fluence-induced photoproduct has been removed by taking the low-fluence limit, and the low-fluence photoproduct has been eliminated in the subtraction. Thus, the argument of ref [22] continues to hold for complex signals, but the presence of a small cross-relaxation term should also be taken into account.

Reference [22] also argued that the biexciton signal derived from MUPPETS $A_b(\tau)$ and the fluence-induced component of 1D measurements $A_1^{(1)}(\tau)$ should differ only due to the effects of a photoproduct. Re-evaluating eq 113 using eq 114 gives

$$\begin{aligned} A_1^{(1)}(\tau) = e^{i\Phi_{12}}C_{2'}(\tau) + e^{i\Phi_e}\frac{\cos\Phi_{12}}{\cos\Phi_e}\frac{1+\delta}{1-\delta} \\ \times\left(C_{1'}^{2'}(\tau) + \frac{\sigma'_p}{4\sigma'_{12}}C_{1',p}(\tau)\right) \end{aligned} \tag{117}$$

As expected, this signal contains both contributions from the biexciton decay of normal particles $C_{2',n}(\tau_1)$ and from the exciton decay of the photoproduct $C_{1',p}(\tau_1)$. Comparing eqs 116 and 117 shows that the difference between the biexciton signal and the fluence-induced 1D signal is only due to the presence of a photoproduct

$$A_1^{(1)}(\tau) = A_b(\tau) + e^{i\Phi_e} \frac{\sigma'_p}{4\sigma'_{12}} \frac{\cos\Phi_{12}}{\cos\Phi_e} \frac{1+\delta}{1-\delta} C_{1',p}(\tau) \qquad (118)$$

This conclusion holds even when cross-relaxation is included.

The experimental comparison of $A_b(\tau)$ and $A_1^{(1)}(\tau)$ is shown in Figure 4.9B. The decays before 300 ps are identical, in both magnitude and phase. The long time portion of the decays are discussed in chapter 5, section 4.3. We neglect the unlikely possibility that the biexciton and photoproduct decay shapes are indistinguishable and conclude that there is no detectable photoproduct under our experimental conditions.

This discussion has assumed that the normal and photoproduct biexciton decays are the same. If the photoproduct is created at high intensity, its biexciton decay would only appear in processes of higher order than those that are included in $A_b(\tau)$ and $A_1^{(1)}(\tau)$. Section 4.4 of chapter 5 will analyze the fluence-induced MUPPETS signal, which is of the correct order, but will find no evidence for a new species. A photoproduct created at low fluence would contribute to $C_{2'}(\tau)$ in both eqs 116 and 117. In this case and neglecting cross-relaxation, the biexciton signal would be

$$A_b(\tau) = e^{i\Phi_{12}} \left(C_{2',n}(\tau) + \alpha C_{2'p}(\tau) \right) \qquad (119)$$

Under the same conditions, the exciton decay would also consist of two parts $C_{1'}(\tau) = C_{1',n}(\tau) + \alpha C_{1',p}(\tau)$, in other words, the exciton decay would be heterogeneous. This possibility is tested in section 4.5, and is not supported by the data. Once again, we conclude that a photoproduct is not affecting our results and is not causing the rate dispersion observed in the biexciton decay.

The role of the cross-relaxation term in eq 116 also needs to be addressed. A general argument can be made that this term is small whenever the exciton lifetime is much longer than the biexciton lifetime. However in our system, the exciton decay is spread over multiple timescales. Some decay occurs even before the biexciton has fully decayed (Figures 4.5 and 4.6). A more quantitative calculation of the size of $C_{1'}^{2'}(\tau)$ for this particular situation is needed.

We previously showed that the cross-relaxation $C_{1'}^{2'}(\tau)$ can be calculated once $C_{1'}(\tau_2)$ and $C_{2'}(\tau_2)$ are known.[66] When $C_{1'}^{2'}(\tau)$ is small and the exciton and biexciton dynamics are uncorrelated, it can be approximated by

$$C_{1'}^{2'}(\tau) = C_{2'}(\tau)\left(1 - C_{1'}(\tau)\right) \tag{120}$$

The calculated curve is shown in Figure 4.9B. Its magnitude is quite small, and $A_b(\tau_2)$ can be taken to be the biexciton decay. In systems where it is larger, eq 120 can be used to correct measurements of the biexciton decay.

Overall, this section has shown that the analysis of ref [22] was simplified by the use of real data and neglect of cross-relaxation. However, those simplifications have no significant effects in this system. In other systems, the more complete analysis presented here may be important. Reference [22] reported eq 107 as one possible fit to the biexciton decay, along with several alternatives. Those fits do not need to be altered as a result of the current re-analysis.

4.5 EXCITON HETEROGENEITY AND EXCITON–BIEXCITON CORRELATION

Section 4.4 considered only the $\tau_1 = 0$ cut through the MUPPETS data, which can be expressed entirely in terms of 1D correlation functions. The full expression for the MUPPETS signal as a function of both τ_1 and τ_2 is[66]

$$\begin{aligned} A_0^{(2)}(\tau_2,\tau_1) = e^{i\Phi_e} C_{1'1'}(\tau_2,\tau_1) - \tfrac{1}{2}\Big[e^{i\Phi_e}\left(1-\delta\right) C_{1'1'}^{2'}(\tau_2,\tau_1) \\ + e^{i\Phi_{12}} \frac{\cos\Phi_e}{\cos\Phi_{12}} \frac{\left(1-\delta\right)^2}{1+\delta} C_{2'1'}(\tau_2,\tau_1) \Big] \end{aligned} \tag{121}$$

Photoproducts are neglected here and in the remainder of the paper. Equation 121 contains three 2D correlation functions corresponding to the three pathways in Figure 4.2: the exciton–exciton correlation function $C_{1'1'}(\tau_2, \tau_1)$ (pathway A), the cross-relaxation function $C_{1'1'}^{2'}(\tau_2,\tau_1)$ (pathway B), and the exciton–biexciton correlation function $C_{2'1'}(\tau_2, \tau_1)$ (pathway C). The precise definitions and detailed discussions of each of these functions can be found in ref [66].

The exciton–exciton correlation $C_{1'1'}(\tau_2, \tau_1)$ is sensitive to whether rate dispersion in the exciton decay is heterogeneous or homogeneous. This correlation function appears in both excitonic and two-level systems. Its behavior in two-level systems has been demonstrated in several previous papers.[11, 13, 14, 19-21] If the sample is heterogeneous, and the exciton decay rate for a given particle is above (below) average during the first interval, the rate will also be above (below) average during the second interval. One can show that the result is

$$C_{1'1'}(\tau_2, \tau_1) = C_{1'}(\tau_2 + \tau_1) \tag{122}$$

On the other hand, if the sample is homogeneous, knowing the exciton decay during the first interval gives no new knowledge about the decay during the second interval, with the result that

$$C_{1'1'}(\tau_2, \tau_1) = C_{1'}(\tau_2) C_{1'}(\tau_1) \tag{123}$$

Thus, there is a qualitative difference between these two cases.

In the current system, the exciton has a pronounced rate dispersion. Almost all the decay observed in our time range is faster than the main radiative decay, and the decay within our time range fits a stretched exponential (eq 106 and Figure 4.6B). This early decay has been attributed to a subset of particles with defective surface passivation.[55] Single-particle experiments often identify particles in various nonfluorescent states, which presumably have fast nonradiative decay.[50, 63, 72] Thus, one can hypothesize that the decay is dispersed because the sample is heterogeneous and that eq 122 will apply to our data.

The exciton–biexciton correlation function $C_{2'1'}(\tau_2, \tau_1)$ is unique to excitonic systems and has not been measured before. Our recent theoretical paper discussed this function in detail.[66] It determines whether knowing the exciton decay rate of a particle, which is measured in the first time interval, predicts the biexciton rate, which is measured in the second. Such a correlation implies a shared feature in the relaxation mechanisms of both the exciton and biexciton. On the other hand, if the exciton and biexciton relax through independent mechanisms, the exciton and biexciton decays are uncorrelated, and

$$C_{2'1'}(\tau_2,\tau_1) = C_{2'}(\tau_2)C_{1'}(\tau_1) \tag{124}$$

In our system, fast exciton decay is usually attributed to trapping of the conduction electron at a surface defect,[20, 94, 106] whereas the biexciton decay is attributed to Auger recombination.[43, 52, 54, 69] Originally, these mechanisms were viewed as unconnected, and no exciton–biexciton correlation would be expected. More recently, it has been suggested that the surface has a significant role in Auger recombination.[59, 107] If the surface defects that trap electrons also facilitate Auger recombination, the exciton and biexciton decays could be correlated.

The 2D cross-relaxation function $C_{1'1'}^{2'}(\tau_2,\tau_1)$ also varies with the nature of the correlation.[66] Formulas are given in the SI and are used in the calculations below. However, it is always small and does not affect the interpretation of the results.

At this point, we can identify one case that is particularly easy to analyze—homogeneous exciton decay and no exciton–biexciton correlation. In this case, the decay in τ_2 is separable from the decay in τ_1 for both $C_{1'1'}(\tau_2, \tau_1)$ and $C_{2'1'}(\tau_2, \tau_1)$ (eqs 123 and 124). The separability also extends to the cross-relaxation function $C_{1'1'}^{2'}(\tau_2,\tau_1)$.[66] Thus,

$$\begin{aligned}A_0^{(2)}(\tau_2,\tau_1) = C_{1'}(\tau_1)\Big\{ & e^{i\Phi_e}C_{1'}(\tau_2) - \tfrac{1}{2}\Big[e^{i\Phi_e}\left(1-\delta\right)C_{1'}^{2'}(\tau_2) \\ & + e^{i\Phi_{12}}\frac{\cos\Phi_e}{\cos\Phi_{12}}\frac{\left(1-\delta\right)^2}{1+\delta}C_{2'}(\tau_2)\Big]\Big\}\end{aligned} \tag{125}$$

As a result, different cuts of the full signal at fixed τ_1 should have the same shape.

Our data are tested for this condition in Figure 4.10. Both magnitude and phase for all values of τ_1 overlap within the experimental noise. Thus, the model of a homogeneous exciton decay and an uncorrelated biexciton decay is sufficient to explain our data.

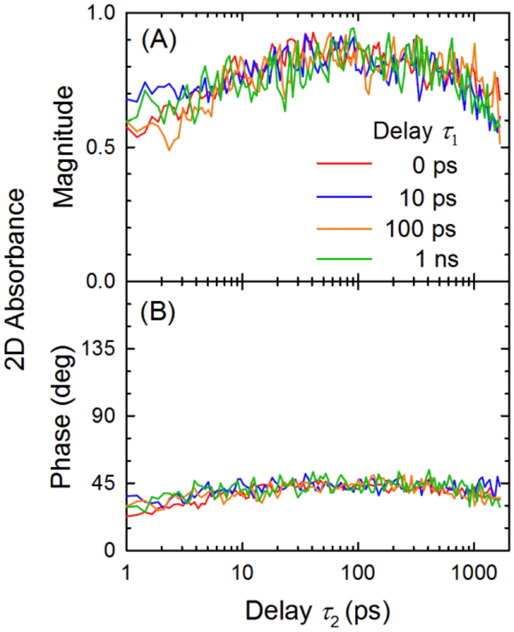

Figure 4.10. 2D MUPPETS results at various values of the first delay τ_1: (A) magnitude and (B) phase. The low-fluence component $A_0^{(2)}(\tau_2, \tau_1)$ has been extracted from the signal versus pump energy (see Figure 4.8). The curves have been normalized to show the lack of a shape change as τ_1 increases.

However, we also need to ask about the sensitivity of the results: Do alternative models change the predictions enough to be detected above the experimental noise? Figure 4.11 addresses this question. The magnitudes of the data are compared to four models combining the choices of purely homogeneous or purely inhomogeneous exciton decay with biexciton decays fully correlated or fully uncorrelated with the exciton. In each case, the model for the 1D correlation functions developed in section 4.3 have been used. When the 1D results are combined with each of the four sets of dynamical assumptions, an independent prediction of the MUPPETS signal can be made. Only the amplitude of the experimental data is scaled in the comparison.

Model one combines a homogeneous exciton decay (eq 123) and an uncorrelated biexciton decay (eq 124) to generate the full signal (eq 117). This is the model that was tested in Figure 4.10. It produces the red curves in Figure 4.11, and as expected, it fits the data well for all values of τ_1.

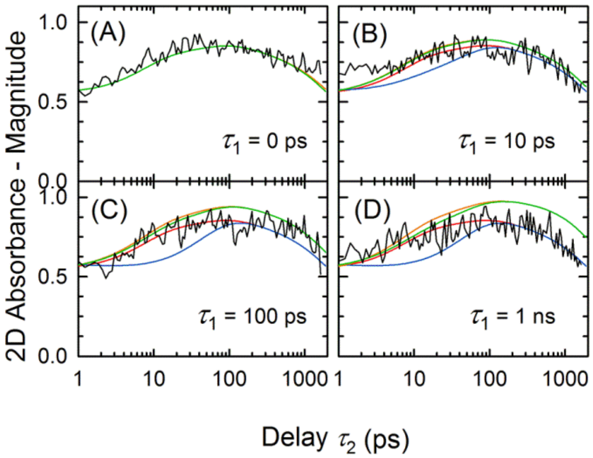

Figure 4.11. Measured low-fluence MUPPETS magnitudes $\left|A_0^{(2)}(\tau_2,\tau_1)\right|$ (black) compared to four models for the dynamics at (A) τ_1 = 0 ps, (B) τ_1 = 10 ps, (C) τ_1 = 100 ps, and (D) τ_1 = 1 ns. Red: Homogeneous exciton decay and no exciton–biexciton correlation. Blue: Homogeneous exciton decay and full exciton–biexciton correlation. Orange: Heterogeneous exciton decay and no exciton–biexciton correlation. Green: Heterogeneous exciton decay and full exciton–biexciton decay correlation.

Model two has a heterogeneous exciton decay (eq 122), while keeping the uncorrelated biexciton (eq 124). It gives the orange curves in Figure 4.11. The effect of the first time interval is to remove particles with a fast relaxing exciton from the measurement. During the second time interval, the exciton decay of the remaining particles lacks the early decay components. Because the biexciton decay is uncorrelated with the exciton, it is unchanged. The net result is that the peak in the signal that results from competition between positive exciton and negative biexciton decays becomes larger and is delayed. The effect is small for short values of τ_1, but for the larger values, the effect clearly falls outside the experimental noise.

The third and fourth models include exciton–biexciton correlation. Additional assumptions are needed to describe this correlation. In model three, the ensemble is assumed to have two subensembles, *a* and *b*, corresponding to the two terms in the fits of eqs 106 and 107. Thus, the 1D correlation functions are sums of two terms

$$C_{1'}(\tau) = aC_{1'a}(\tau) + bC_{1'b}(\tau) \tag{126}$$

and

$$C_{2'}(\tau) = aC_{2'a}(\tau) + bC_{2'b}(\tau) \tag{127}$$

with $a = 0.635$ and $b = 0.365$. In subensemble *a*, both the exciton and the biexciton decay rapidly, whereas in subensemble *b*, both decays are slow. With this model, the exciton and biexciton rates are fully correlated, and

$$\begin{aligned} C_{2'1'}(\tau_2,\tau_1) = \Big(& a^2 C_{2'a}(\tau_2)C_{1'a}(\tau_1) + abC_{2'a}(\tau_2)C_{1'b}(\tau_1) \\ & + abC_{2'b}(\tau_2)C_{1'b}(\tau_1) + b^2 C_{2'b}(\tau_2)C_{1'b}(\tau_1)\Big) \\ & \div \left(a^2 + 2ab + b^2\right) \end{aligned} \tag{128}$$

Subensemble *a* has a stretched-exponential exciton correlation function $C_{1'a}(\tau_1)$. In model three, the exciton decay is heterogeneous, so eq 122 still holds. However, all particles have the same biexciton decay $C_{2'a}(\tau_1)$.

The total signal for model three is given in Figure 4.11 as the green curves. It is only slightly different from model two, which lacks the exciton–biexciton correlation (orange curves). The maximum effect of the correlation occurs when τ_1 is between the exciton lifetimes of the two subspecies, in this case, between 4.9 and 20 ns. Thus, our time range is not well suited to measuring this correlation in the case of a heterogeneous exciton decay.

Fortunately, neither model based on a heterogeneous exciton decay matches the data well. Thus, the exciton rate dispersion must be homogeneous. This implies that the creation of the exciton initiates some relaxation in the local environment. The relaxation of the environment then causes a time-dependent rate of exciton decay.

Model four retains the homogeneous dispersion of the exciton (eq 123), but assumes that the exciton and biexciton decays are correlated though a common dependence on the environment. We also assume that the environment relaxes in the same way in both the exciton and biexciton states. With these assumptions,[66]

$$C_{2'1'}(\tau_2,\tau_1) = \frac{C_{2'}(\tau_2+\tau_1)C_{1'}(\tau_1)}{C_{2'}(\tau_1)} \tag{129}$$

In our system, the instantaneous biexciton rate changes over a narrow range of times, and the instantaneous exciton rate changes only slightly over that range. Thus, this model requires that the biexciton rate be much more sensitive to the environment than the exciton rate is.

The MUPPETS results are compared to model four in Figure 4.11 (blue curves). The effect on the biexciton portion of the decay is quite dramatic and inconsistent with the data. Thus, the model with a homogeneous exciton decay and an uncorrelated biexciton decay is the only one that matches the data.

Although the data do favor model one, better data could make a stronger case. Greater discrimination between the models could come from reducing the experimental noise, but just as important is increasing the experimental time range. Figure 4.11 gives an example of the general conclusion that there is no discrimination when $\tau_1 = 0$, and the level of discrimination increases as τ_1 increases. The important parameter is the ratio of noise to the difference between models. Because the signal has not fully decayed in our experiments, increasing τ_1 further would increase that difference with little increase in noise. Ideally, the experimental time range should cover all the relevant decay times, i.e., another one to two orders-of-magnitude longer in this system. The current limitation is the use of optical delay lines, which become increasing difficult to align as they become longer. Pulse timing based on electronics would allow access to the longer delays needed to more fully exploit the MUPPETS experiment.

4.6 SUMMARY AND CONCLUSIONS

A complete MUPPETS data set on an excitonic system has been analyzed for the first time. Accomplishing this analysis required progress in several directions. The first was systematizing the treatment of complex data. MUPPETS data is inherently complex, and complex transient-grating data was collected to assist in the analysis. An external standard was used to determine the absolute phase of the absorbances. Expressions for both transient-grating and MUPPETS data in terms of practical parameters allowed systematic fitting of the complex data and transfer of parameters between the two experiments. Assumptions that the solute absorbance is real or that all transitions have the same phase or magnitude were avoided and clearly do not apply to this system.

A second direction was making a detailed comparison of 2D and 1D data. Along the $\tau_1 = 0$ cut, the MUPPETS data should be almost entirely determined by quantities measurable by 1D methods. Using the heterodyned transient-grating data, the MUPPETS results, including its time-dependent phase, were explained. The only adjustable parameter was the ratio of ground-to-exciton and exciton-to-biexciton absorption cross-sections. The fit value is exactly what is expected from an uncorrelated-electron model, which is widely used for CdSe nanoparticles.[43] Overall, this fit verifies the theory and execution of the MUPPETS experiment and shows that the simple spectroscopic model used here captures all relevant species and transitions.

The complex $\tau_1 = 0$ data provide a more rigorous test of the conclusions of our earlier letter.[22] We confirmed the original conclusion that the biexciton decay is highly disperse. This finding challenges existing theories for the biexciton decay and the standard methods of extracting biexciton decays from fluence-induced experiments. Biexciton decay has been explained by extending the theory of Auger recombination in bulk semiconductors to nanoparticles.[43, 52, 54, 69] This theory predicts a single exponential decay, in contrast to the dispersed decay found here. Previously, dispersed decays were attributed solely to the involvement of higher excitons. In fact, the assumption of exponential decay has been used to decompose such data into components due to different numbers of excitons.[52, 54] Photoproducts have also been implicated as mimicking biexciton decay.[44, 62] The concerted analysis of fluence-induced transient-grating and MUPPETS data has shown that the observed dispersion is not due to higher excitons or photoproducts, but rather is inherent to the biexciton decay. This finding joins several recent challenges to the existing theory of decay by Auger recombination.[56-58] The ability of the surface to modify the biexciton decay has been documented and may provide a route to resolving the current discrepancies.[59, 107]

Reference [66] showed that MUPPETS in excitonic systems should involve a cross-relaxation term (Figure 4.2B) in addition to pure exciton and biexciton dynamics. This paper showed that it is experimentally feasible to gather sufficient information to calculate these terms and included them in a quantitative analysis. In the current system, these terms are quite small.

Going beyond the $\tau_1 = 0$ cut provided information on dispersion in the exciton decay and correlations between the exciton and biexciton decays. The extent of nonradiative decay is large: 40% within 2 ns was observed directly, and 64% was extrapolated from fitting. The nonradiative component is highly dispersed; it fits a stretched exponential with $\beta = 0.3$. Similar results have been seen by others.[55, 64, 94, 102] The most obvious interpretation is that the surface passivation is still incomplete. Thus, the decay should be heterogeneous due to particle-to-particle variation in the number and activity of the remaining passivation defects. Surprisingly, the MUPPETS measurements contradict this explanation. They find a homogeneous relaxation, that is, one driven by a relaxation initiated by the creation of the exciton.

Given this conclusion, we can speculate about the mechanism. There are various charged species at the surface of the particle: lattice defects, charged surfactants, and counterions. Thermal fluctuations in the properties of nanoparticles seen in single-particle measurements suggest that at least some of these species are mobile and therefore polarizable.[50, 63, 72] The exciton is also more polarizable than the ground state. Upon excitation, the exciton and surface should relax to a mutually polarized state. The Stokes shift of the exciton is small, so the resulting change in transition energies must be small.[43] However, the polarized exciton would also have a reduced electron–hole overlap, which would reduce the absorption cross-section. Thus, surface polarization would cause a loss of signal, but not population decay. Both a large signal decay and a high quantum yield would occur. This mechanism provides at least one physically plausible explanation for the MUPPETS result.

The biexciton decay was found to have substantial dispersion, but to be uncorrelated with the exciton decay. The fact that the biexciton decay is much faster than the exciton already suggests a different decay process, so the lack of correlation is not surprising. Current ideas about biexciton decay are focused on Auger recombination, but with an influence from the surface.[59, 107] Thus, the dispersion in the biexciton could reflect surface heterogeneity. The MUPPETS experiments discussed here do not directly comment on the heterogeneity of the biexciton decay. (The possibility of addressing this question is discussed in chapter 5.[79]) However, a homogeneous exciton relaxation and a heterogeneous biexciton decay would be consistent with the lack of correlation found by MUPPETS.

Overall, the data in this paper have shown the features of MUPPETS in excitonic systems that were predicted in ref [66]. Chapter 5 of this paper[79] will discuss potential interferences that are encountered in real experiments, but that go beyond the basic theory of MUPPETS, as developed in ref [66] and used here. It will confirm that the conclusions of this paper are sound, even when these effects are considered.

CHAPTER 5 MULTIPLE POPULATION-PERIOD TRANSIENT SPECTROSCOPY OF CDSE/ZNS NANOPARTICLES. II. EFFECTS OF HIGH FLUENCE AND SOLVENT HEATING

5.1 INTRODUCTION

In chapter 4 of this paper,[108] the dynamics of excitons and biexcitons in CdSe/ZnS core–shell nanoparticles were analyzed with multiple population-period transient spectroscopy (MUPPETS). MUPPETS is a form of two-dimensional (2D) kinetics, i.e., it contains two, variable time intervals. In systems with complicated kinetics, MUPPETS provides information about the heterogeneity of the system and the connections between the relaxation of different transitions. MUPPETS is a six-pulse experiment, and as a result, the core theory for MUPPETS focuses on the $\chi^{(5)}$ response of the chromophores.[16, 17, 21, 66] This theory was used in chapter 4. However in real experiments, other processes must be considered, in particular, higher order responses of the chromophores and the thermal response of the solvent. This part of the paper presents new methods for analyzing these secondary effects and applies them to the data presented in chapter 4.

Chapter 4 confirmed the prediction that the MUPPETS signal has a negative biexciton component in the low-fluence limit. However, this feature was rapidly lost with modest fluence increases and was replaced with a similar positive feature. One concern is that another, unexpected species is involved, such as a photoproduct or higher exciton, with unforeseen effects on the nominally low fluence data.

This problem is addressed by extending the calculation of the signal to include $\chi^{(7)}$ "saturation" terms. We show how the Hilbert-space pathway formalism[16, 17] for calculating MUPPETS can be extended to include these processes. The calculation readily explains all the observed fluence effects. Concerns about unknown species are alleviated, and the conditions needed to avoid saturation are quantified.

Solvent thermal effects in MUPPETS are an extension of the thermal gratings and thermal lenses seen in lower order experiments.[109-112] The relaxation of the excited state of a solute typically heats the surrounding solvent. The resulting change in index-of-refraction of the solvent can be detected optically by diffraction or deflection of the probe beam. The size of this signal from the solvent is often similar to the change in solute absorption. We have observed strong thermal effects in MUPPETS experiments in other systems.[18] Detailed theory and experimental data showing thermal effects in MUPPETS with two-level chromophores have been reported before,[18, 19] and the basic theory for thermal effects in excitonic systems has been presented recently.[66] In general, thermal effects present a hazard if they are not correctly separated from the resonant signals.

On the other hand, in one-dimensional (1D) experiments, thermal effects have been useful in measuring the heat released in chemical processes, which is otherwise spectroscopically unobservable.[45, 48, 113-115] In a similar manner, thermal effects in MUPPETS might yield information on trap states—long-lived, optically dark states that do not release heat to the solvent. In CdSe nanoparticles, such traps are sometimes invoked as the final state for exciton and biexciton relaxation.

A particular example is the biexciton signal measured in chapter 4 of this paper (Figure 4.9B).[108] It shows an unexplained signal recurrence at long times that is qualitatively consistent with a thermal effect. Does this signal isolate the biexciton thermal effect as it isolates the biexciton resonant effect? Does the size of the signal provide a measure of the yield of trap states?

Answering these questions requires an independent calibration of the expected size of the thermal effects. We will show that it is possible to use an external standard to determine the ratio of thermal to resonant signal sizes. The calibration shows that the thermal effects should be small in this system and do not affect the conclusions of chapter 4. Unfortunately, their small size also makes them comparable to systematic errors in the data. In the experiments, it is difficult to draw firm conclusions about the yield of trap states.

In general, the additional analysis in this part of the paper will not change any of the conclusions about the dynamics of excitons or biexcitons drawn in chapter 4. However, it provides the theory for secondary processes in MUPPETS experiments and a practical example of how to control for them.

5.2 FLUENCE-INDUCED SIGNALS

We introduced a Hilbert-space pathway method for treating incoherent experiments with *N* time dimensions, including 2D-MUPPETS experiments.[16, 17, 21, 66] This method has been used previously only to calculate the low-fluence limit of these experiments. This section shows how this approach can be extended to include the first-order fluence dependence, both in the case of a general *N*-dimensional experiment and in the specific case of 2D-MUPPETS on an excitonic system. Section 5.2.1 summarizes the method and notation in the low-fluence case. Section 5.2.2 introduces fluence-induced calculations and illustrates their use in the more familiar case of 1D measurements. New results for 2D-MUPPETS are produced in section 5.2.3. They are then compared to the experimental data of chapter 4 in section 5.2.4.

5.2.1 Standard Pathway Method.

The method associates every incoherent state (quantum-mechanical population state) with a vector $|P]$ in a Hilbert-space. (The analogy with quantum Hilbert-space vectors $|\psi\rangle$ is intentional and well-defined.[16]) The signal is calculated as the generalized, complex absorbance of the (N+1)th pulse-pair $A^{(N)}$ (eq. 103). It is found by taking the product of the detection cross-section vector $[\sigma_D|$ with the final-state vector $|f^{(N)}]$

$$A^{(N)} = (-1)^N \rho L[\sigma_D \,|\, f^{(N)}] \tag{130}$$

The density of chromophores is ρ, the length of the sample is L. Because the states represent the entire sample, not a single molecule, an ensemble average is implied by the vector product.

The final state is created from the initial, equilibrium state $|eq]$ by N optical transitions alternating with periods of free time evolution. In MUPPETS, each excitation is created by a pair of pulses, each pulse contributing one electric-field interaction. The nth optical excitation at time t_n is represented by the transition operator $\mathbf{T}_n$, and the evolution between transitions is represented by the operator $\mathbf{G}(t_{n+1}, t_n)$. The operator $\mathbf{G}(t_{n+1}, t_n)$ refers to the dynamics of a single chromophore. For nonexponential decays, it depends on the time from the first excitation t_n, as well as the time interval, $\tau_n = t_n - t_{n-1}$. Thus, the signal is calculated from

$$\begin{aligned} A^{(N)}(\tau_N,\ldots,\tau_1) = (-1)^N \rho L\, [\sigma_D \,|\, &\mathbf{G}(t_N, t_{N-1})\mathbf{T}_N \\ &\times \ldots \mathbf{G}(t_1, t_0)\mathbf{T}_1 \,|\, eq] \end{aligned} \tag{131}$$

In a system without significant polarization effects, and in an experiment in which only one pulse combination is well phase-matched, the transition operator $\mathbf{T}_n$ is a simple product of I_n, the geometric-mean fluence of the nth pulse-pair, and the optical transition cross-section operator $\boldsymbol{\sigma}_T$

$$\mathbf{T}_n = I_n \boldsymbol{\sigma}_T \tag{132}$$

For simplicity, all the excitation pulses will be assumed to have the same fluence. Both the transition cross-section operator $\boldsymbol{\sigma}_T$ and the detection cross-section vector $[\sigma_D|$ are constructed from a model of the system's spectroscopy (e.g., Figure 4.7A), but the two are not identical.

Pathways are generated by selecting a basis set and using it to enumerate all possible intermediate states in eq 131. Our model of the electronic states of CdSe nanoparticles (Figure 4.7A) defines three states: the ground state |0], the exciton |1] and the biexciton |2]. (The fast relaxing fine structure within the exciton and biexciton states are incorporated into an effective optical-transition cross-section operator $\boldsymbol{\sigma}_T$ for the system.[17]) The number of pathways in the calculation can be minimize by switching to a basis set with strong selection rules on $\boldsymbol{\sigma}_T$ and $\mathbf{G}$. For an excitonic system the best basis set is nonorthogonal: $|0'] = |0]$, $|1'] = (|1]-|0])/\sqrt{2}$ and $|2'] = (|2]-|1])/\sqrt{2}$.[66]

The notation is more compact if the matrix elements of an operator $\mathbf{O}$ are written

$$O_j^i = [j|\mathbf{O}|i] \tag{133}$$

and those of a vector $|P]$ are written

$$P_i = [i|P] \tag{134}$$

or

$$P^i = [P|i] \tag{135}$$

(Because a nonorthogonal basis set is used, bras and superscripts are not equivalent to kets and subscripts.[42]) Starting with eq 132 and inserting complete sets of states between all the operators in eq 131 yields

$$\begin{aligned} A^{(N)} &= (-1)^N \rho L I^N (\sigma_D)^n G_n^m(t_N, t_{N-1}) (\sigma_T)_m^l \\ &\quad \times \ldots G_j^i(t_1, t_0) (\sigma_T)_i^{eq} \end{aligned} \tag{136}$$

The convention of summation over repeated indices is used.[42] Each term in the implied sum is one pathway.

Collecting all the time-evolution terms and averaging them over the ensemble creates an N-dimensional correlation function

$$C_{n,\ldots,j}^{m,\ldots,i}(\tau_N,\ldots,\tau_1) = G_n^m(t_N,t_{N-1})\ldots G_j^i(t_1,t_0) \tag{137}$$

Equation 136 becomes

$$\frac{A^{(N)}(\tau_N,\ldots,\tau_1)}{A'^{(0)}} = (-1)^N I^N \left[(\sigma_D)^n (\sigma_T)_m^l \cdots (\sigma_T)_k^j \right] \times C_{n,\ldots,j}^{m,\ldots,1'}(\tau_N,\ldots,\tau_1) \tag{138}$$

where the static absorbance of the sample is $A'^{(0)} = \rho L(\sigma_T)_{1'}^{0'}$. We have used the facts that at equilibrium, all the molecules are in the ground state, $|0'] = |eq]$, and that the first intermediate state i is always $|1']$ when the exciton basis set is used.[66] Each pathway in eq 138 consists of a correlation function and a weight represented by the term in square brackets.

The application of this general formalism to the specific cases of 1D and 2D experiments, $A^{(1)}(\tau_1)$ and $A^{(2)}(\tau_2,\tau_1)$ respectively, in the CdSe system is illustrated in Figures 5.1 and 5.2. The low-fluence contributions, $A_{\mathrm{A}}^{(1)}(\tau_1)$ and $A_{\mathrm{A}}^{(2)}(\tau_2,\tau_1)$, are due to the pathways in Figures 5.1A and 5.2A. The relevant sequence of operators from the expressions

$$A_{\mathrm{A}}^{(1)}(\tau_1) = -\rho L\,[\sigma_D\,|\,\mathbf{G}(t_1,t_0)\mathbf{T}_1\,|\,0'] \tag{139}$$

and

$$A_{\mathrm{A}}^{(2)}(\tau_2,\tau_1) = \rho L\,[\sigma_D\,|\,\mathbf{G}(t_2,t_1)\mathbf{T}_2\mathbf{G}(t_1,t_0)\mathbf{T}_1\,|\,0'] \tag{140}$$

(cf. eq 131) are given on the top of each panel. Immediately below are labels for the intermediate states used to define the pathways in the expressions

$$\frac{A_{\mathrm{A}}^{(1)}(\tau_1)}{A'^{(0)}} = -I\left(\sigma_D\right)^j C_j^{1'}(\tau_1), \qquad (141)$$

and

$$\frac{A_{\mathrm{A}}^{(2)}(\tau_2,\tau_1)}{A'^{(0)}} = I^2\left(\sigma_D\right)^l \left(\sigma_T\right)_k^j C_{l,j}^{k,1'}(\tau_2,\tau_1), \qquad (142)$$

(cf. eq 138).

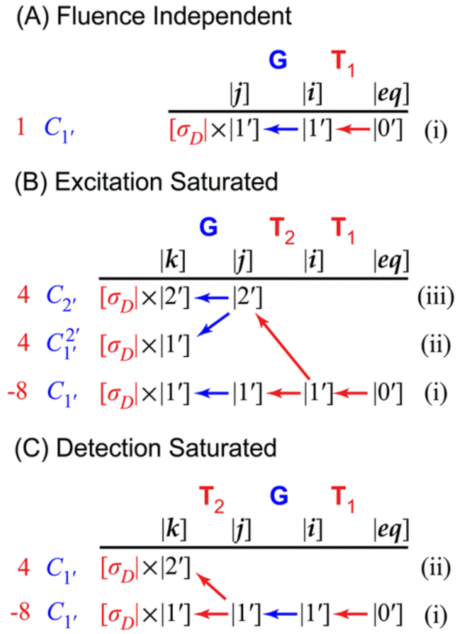

Figure 5.1. Pathways used to calculate the resonant signal in 1D (pump–probe and transient-grating) experiments, including the fluence dependence. The population states $|P]$ are transformed by a sequence of optical transitions (red), which are governed by the operator **T**, and free evolution in time (blue), which is governed by the operator **G**. The final state is measured by taking the product of the final state with the detection vector $[\sigma_D|$. On the far left, each pathway is labeled with its relative weight, which is determined by the product of transition and detection matrix elements (red). The relative weights are shown here for the simple case $\sigma_{01} = \sigma_{12} = 1$. On the near left, each pathway is labeled by its correlation function C_x, which is determined by the product of time-evolution matrix elements (blue). (A) Pathways with no fluence dependence. (B) Pathways with fluence dependence due to two interactions with the excitation pulses. (C) Pathways with fluence dependence due to two interactions with the detection pulses.

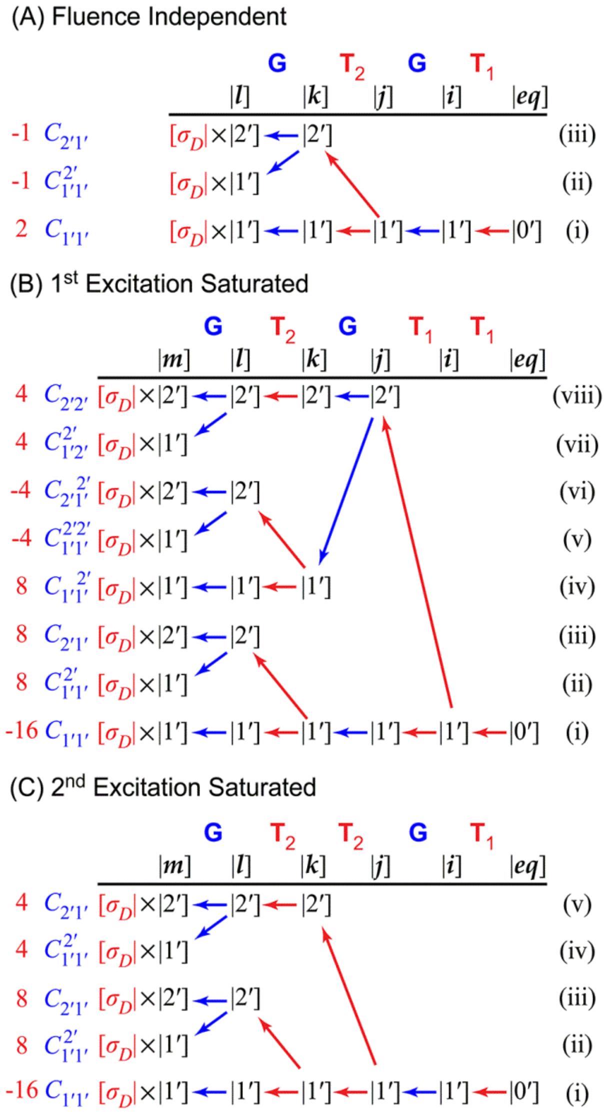

Figure 5.2. Pathways used to calculate the of the resonant signal in 2D (MUPPETS) experiments, including the fluence dependence. The format is explained in the caption to Figure 5.1. (A) Pathways with no fluence dependence. (B) Pathways with fluence dependence due to saturation of the excitation pulses. (C) Pathways with fluence dependence due to saturation of the detection pulses.

Non-zero pathways contributing to these sums are listed below the solid lines. The basis set has been chosen to impose strong selection rules to limit the number of pathways.[66] The only allowed transition out of the initial state |0′] is to |1′], and its cross-section is included in $A'^{(0)}$. Subsequent transitions in the CdSe system are governed by[66]

$$\left(\sigma_T\right)^i_j = \begin{pmatrix} -\sigma'_{12} & \sigma'_{12} \\ 0 & -2\sigma'_{01} \end{pmatrix} \tag{143}$$

The initial state |0′] never appears as an intermediate state. As a result, eq 143 (and eq 144 below) are written in the reduced basis set {|1′], |2′]}. Time-evolution never takes a state to one with a higher index. For 1D measurements, these restrictions leave only one pathway (Figure 5.1A). In 2D measurements, they leaves three pathways (Figure 5.2A), which are described more loosely by the ladder diagrams in Figure 4.2.

The correlation function for each pathway is constructed from the time-evolution steps of each pathway (eq 137). These are given on the left-hand sides of Figures 5.1 and 5.2. The weight for each pathway (bracketed term in eq 138) is given on the far left of Figures 5.1 and 5.2. Their calculation requires the detection cross-section vector for the CdSe system,[66]

$$\left(\sigma_D\right)^i = -\begin{pmatrix} \sigma_{12} & \sigma_e \end{pmatrix} \tag{144}$$

with

$$\sigma_e = 2\sigma_{01} - \sigma_{12} \tag{145}$$

The figures gives only the simple case of $\sigma_{01} = \sigma_{12} = \sigma$. The full expressions without this simplification are

$$\frac{A^{(1)}_{\mathrm{A}}(\tau_1)}{A'^{(0)}} = I\sigma_e C_{1'}(\tau_1) \tag{146}$$

and

$$\frac{A_{\mathrm{A}}^{(2)}(\tau_2,\tau_1)}{A'^{(0)}} = I^2\Big[\sigma_e\left(2\sigma'_{01}\right)C_{1'1'}(\tau_2,\tau_1) \\ -\sigma_e\sigma'_{12}C_{1'\,1'}^{2'}(\tau_2,\tau_1)-\sigma_{12}\sigma'_{12}C_{2'1'}(\tau_2,\tau_1)\Big] \tag{147}$$

For simplicity, a repeated subscript and superscript on a correlation function are only written once, e.g., $C_{1'}^{1'} = C_{1'}$. After normalization (eqs I.104 and I.105) and rewriting the complex cross sections in terms of practical fitting parameters, these equations give the expressions for the low-fluence, 1D and 2D absorbances used in chapter 4 (eqs I.112 and I.121, respectively).[108]

5.2.2 Calculating 1D Fluence-Induced Signals.

The extension of the pathway calculations to fluence-induced signals is illustrated for 1D experiments in Figure 5.1B. Two interactions occur with the excitation pulse pair, giving the additional absorbance

$$A_{\mathrm{B}}^{(1)}(\tau_1) = -\rho L\,[\sigma_D\,|\,\mathbf{G}(\tau_1,0)\mathbf{T}_1\mathbf{T}_1\,|\,0'] \tag{148}$$

(cf. eq 139). The double interaction is treated as a sequence of incoherent transitions. This approach is appropriate when the excitation pulses are substantially longer than the dephasing time of the transition. In this case, pathways with a population state as an intermediate dominate. For very short excitation pulses, a single operator including two-quantum coherences would need to be derived from first principles.[17]

Expanding into pathways over intermediate states gives

$$\frac{A_{\mathrm{B}}^{(1)}(\tau_1)}{A'^{(0)}} = -\varepsilon_2 I^2\left(\sigma_D\right)^k\left(\sigma_T\right)_j^{1'}C_k^j(\tau_1) \tag{149}$$

(cf. eq 141). The allowed pathways in this sum are enumerated in Figure 5.1B, as are the corresponding correlation functions.

The term ε_2 is included in eq 149 to account for the degeneracy in the phase-matching conditions associated with a double interaction. The phase-matching condition for the low-fluence term is

$$\left(\vec{k}_{1a} - \vec{k}_{1b}\right) + \left(\vec{k}_{2a} - \vec{k}_{2b}\right) = 0 \tag{150}$$

where $\vec{k}_{xy}$ is the *k*-vector for pulse $y \in \{a, b\}$ of the *x*th pulse-pair. By assumption, the experiment is designed to allow one and only one phase-matched combination of pulses. The double degeneracy from multiplying this equation by minus one is already included in the definition of the cross-section. Thus there is no degeneracy for the low-fluence experiment.

However, the phase-matching condition for the pathways in Figure 5.1B is

$$\left(\vec{k}_{1a} - \vec{k}_{1b}\right) + \left(\vec{k}_{1a} - \vec{k}_{1a}\right) + \left(\vec{k}_{2a} - \vec{k}_{2b}\right) = 0 \tag{151}$$

There is a two-fold degeneracy from swapping the first and second terms in parentheses and another two-fold degeneracy from transforming *a* to *b* in the second set of parentheses. Thus, the total degeneracy for a double interaction of **T** is $\varepsilon_2 = 4$. This degeneracy is included in the pathway weights listed in Figures 5.1 and 5.2.

Using the cross-sections from our system (eqs 143 and 144) in eq 149 gives the total absorbance due to a double interaction with the excitation pulse,

$$\begin{aligned}\frac{A_{\mathrm{B}}^{(1)}(\tau_1)}{A'^{(0)}} = -4I^2\Big[&\sigma_e\left(2\sigma'_{01}\right)C_{1'}(\tau_1) - \sigma_e\sigma'_{12}C_{1'}^{2'}(\tau_1) \\ &-\sigma_{12}\sigma'_{12}C_{2'}(\tau_1)\Big]\end{aligned} \tag{152}$$

The effects are as expected. The first term represents saturation of the ground-to-exciton transition. The third term is due to the creation of biexcitons. The second term is the cross-relaxation term needed to correct the decay of excitons derived from biexcitons relative to the decay of directly created excitons.

We also consider a double interaction with the probe pulse-pair in Figure 5.1C. An optical transition between states $\mathbf{T}_2$ occurs immediately before the detection of the final state, giving a contribution to the absorption of

$$A_{\mathrm{C}}^{(1)}(\tau_1) = -\rho L\,[\sigma_D \,|\, \mathbf{T}_2 \mathbf{G}(\tau_1, 0) \mathbf{T}_1 \,|\, eq] \tag{153}$$

(cf. eq 139). When this equation is expanded into pathways, the general expression is

$$\frac{A_{\mathrm{C}}^{(1)}(\tau_1)}{A'^{(0)}} = -\varepsilon_2 I^2 \left(\sigma_D\right)^k \left(\sigma_T\right)_k^j C_j^{1'}(\tau_2, \tau_1) \tag{154}$$

There are only two nonzero pathways, as shown in Figure 5.1C. For the CdSe system (eqs 143 and 144), these pathways give

$$\frac{A_{\mathrm{C}}^{(1)}(\tau_1)}{A'^{(0)}} = -4I^2 \left[\sigma_e \left(2\sigma'_{01}\right) - \sigma_{12}\sigma'_{12}\right] C_{1'}(\tau_1) \tag{155}$$

(cf. eq 141). Biexcitons are created too late to contribute to the dynamics; they only alter the effective cross-section of the exciton dynamics. The net effect is to suppress the signal from the excitons.

In many 1D experiments, the probe fluence is attenuated relative to the excitation fluence. Equations 152 and 155 show that the saturation effects of the probe and excitation are quite similar in size. If the excitation is attenuated sufficiently to avoid fluence effects, there is no fundamental need to attenuate the probe further than the excitation. In our 1D experiments, the excitation and probe had the same fluences.

chapter 4 of the paper normalized data at different fluences and extracted low-fluence and fluence-induced components, $A_0^{(1)}(\tau_1)$ and $A_1^{(1)}(\tau_1)$, respectively. To calculate these quantities, all sources of signal, $A_{\mathrm{A}}^{(1)}(\tau_1)$, $A_{\mathrm{B}}^{(1)}(\tau_1)$, and $A_{\mathrm{C}}^{(1)}(\tau_1)$, must be added and the result normalized according to eq. 104 to give $\overline{A}^{(1)}(\tau_1)$. This quantity is truncated to first order in I and then divided into low-fluence and fluence-induced components

$$\overline{A}^{(1)}(\tau_1) = A_0^{(1)}(\tau_1) + 4I\sigma'_{12}\frac{|\sigma_{12}|}{|\sigma_e|}A_1^{(1)}(\tau_1) \tag{156}$$

The low-fluence component $A_0^{(1)}(\tau_1)$ is simply related to $A_{\mathrm{A}}^{(1)}(\tau_1)$, giving eq 112. The result is the same as a calculation without fluence-induced terms. All the terms containing the exciton decay are removed by the normalization, leaving the fluence-induced component

$$A_1^{(1)}(\tau_1) = e^{i\Phi_{12}}\left(C_{2'}(\tau_1) + \frac{\sigma_e}{\sigma_{12}}C_{1'}^{2'}(\tau_1)\right) \tag{157}$$

with only biexciton decay $C_{2'}(\tau_1)$ and cross-relaxation $C_{1'}^{2'}(\tau_1)$ terms. Rewriting the cross-sections in terms of practical parameters gives eq 113. Although the phenomena involved in the fluence-induced 1D experiments are familiar, we are not aware of a previous derivation that includes the complex cross-sections and phase effects needed to describe a heterodyned transient-grating experiment.

5.2.3 Calculating 2D Fluence-Induced Signals.

The fluence-dependence of the MUPPETS signal is calculated using the same approach used in section 5.2.2. There are three places where an extra interaction can create additional absorbances: during the first excitation,

$$A_{\mathrm{B}}^{(2)}(\tau_2,\tau_1) = \rho L\,[\sigma_D\,|\,\mathbf{G}(t_2,t_1)\mathbf{T}_2\mathbf{G}(t_1,t_0)\mathbf{T}_1\mathbf{T}_1\,|\,0'] \tag{158}$$

during the second excitation,

$$A_{\mathrm{C}}^{(2)}(\tau_2,\tau_1) = \rho L\,[\sigma_D\,|\,\mathbf{G}(t_2,t_1)\mathbf{T}_2\mathbf{T}_2\mathbf{G}(t_1,t_0)\mathbf{T}_1\,|\,0'] \tag{159}$$

or during the detection

$$A_{\mathrm{D}}^{(2)}(\tau_2,\tau_1) = \rho L\,[\sigma_D\,|\,\mathbf{T}_3\mathbf{G}(t_2,t_1)\mathbf{T}_2\mathbf{G}(t_1,t_0)\mathbf{T}_1\,|\,0'] \tag{160}$$

(cf. eq 140). In our MUPPETS experiments, the probe pulse was attenuated by a factor of ten, primarily to simplify the current calculations by making $A_{\mathrm{D}}^{(2)}(\tau_2,\tau_1)$ small. Thus, we will drop $A_{\mathrm{D}}^{(2)}(\tau_2,\tau_1)$ for the remainder of the paper, although it can be treated with similar methods.

When the other two processes are expanded in pathways, we get

$$\frac{A_{\mathrm{B}}^{(2)}(\tau_2,\tau_1)}{A'^{(0)}} = \varepsilon_2 I^3 \left(\sigma_D\right)^m \left(\sigma_T\right)_l^k \left(\sigma_T\right)_j^{1'} C_{m,k}^{l,\,j}(\tau_2,\tau_1) \tag{161}$$

and

$$\frac{A_{\mathrm{C}}^{(2)}(\tau_2,\tau_1)}{A'^{(0)}} = \varepsilon_2 I^3 \left(\sigma_D\right)^m \left(\sigma_T\right)_l^k \left(\sigma_T\right)_k^j C_{m,j}^{l,\,1'}(\tau_2,\tau_1) \tag{162}$$

(cf. eq 142). The allowed pathways are illustrated in Figure 5.2B–C. The *k*-vector degeneracies are still those for pairs of interactions, i.e., $\varepsilon_2 = 4$.

The full results are quite complicated, with eight pathways for $A_{\mathrm{B}}^{(2)}(\tau_2,\tau_1)$ and five for $A_{\mathrm{C}}^{(2)}(\tau_2,\tau_1)$. However, chapter 4 of the paper has already shown that cross-relaxation in our system is negligibly small. Thus, we drop all pathways whose correlation function contains a $G_{1'}^{2'}$ term. Only three pathways remain for $A_{\mathrm{B}}^{(2)}(\tau_2,\tau_1)$ (i, iii and viii) and for $A_{\mathrm{C}}^{(2)}(\tau_2,\tau_1)$ (i, iii and v). They evaluate to

$$\begin{aligned}\frac{A_{\mathrm{B}}^{(2)}(\tau_2,\tau_1)}{A'^{(0)}} = -4I^3\Big[&\sigma_e\left(2\sigma'_{01}\right)^2 C_{1'1'}(\tau_2,\tau_1)\\ &-\sigma_{12}\sigma'_{12}\left(2\sigma'_{01}\right)C_{2'1'}(\tau_2,\tau_1)\\ &-\sigma_{12}\left(\sigma'_{12}\right)^2 C_{2'2'}(\tau_2,\tau_1)\Big]\end{aligned} \tag{163}$$

and

$$
\begin{aligned}
\frac{A_{\mathrm{C}}^{(2)}(\tau_2,\tau_1)}{A'^{(0)}} = -4I^3\Big[&\sigma_e\left(2\sigma'_{01}\right)^2 C_{1'1'}(\tau_2,\tau_1) \\
&-\sigma_{12}\sigma'_{12}\left(2\sigma'_{01}\right)C_{2'1'}(\tau_2,\tau_1) \\
&-\sigma_{12}\left(\sigma'_{12}\right)^2 C_{2'1'}(\tau_2,\tau_1)\Big]
\end{aligned}
\qquad (164)
$$

The first pair of terms in eqs 163 and 164 are the same. They have the same shape as the low-fluence signal (eq 147 with cross-relaxation neglected), but the opposite sign. These terms represent simple saturation of the signal size without a change in shape. The last terms of both eqs 163 and 164 are due to the creation of extra biexcitons at high fluence. In particular, eq 163 contains a biexciton–biexciton correlation function $C_{2'2'}(\tau_2, \tau_1)$ that has not appear previously.

For comparison to the experimental data, $A_{\mathrm{A}}^{(2)}(\tau_2,\tau_1)$, $A_{\mathrm{B}}^{(2)}(\tau_2,\tau_1)$, and $A_{\mathrm{C}}^{(2)}(\tau_2,\tau_1)$ (eqs 147, 163, and 164) are summed and normalized to the exciton–exciton decay (eq. 105) to give $\overline{A}^{(2)}(\tau_2,\tau_1)$. This expression is expanded in powers of I and truncated at first order to give

$$
\begin{aligned}
\overline{A}^{(2)}(\tau_2,\tau_1) = {} & A_0^{(2)}(\tau_2,\tau_1) \\
& +4I\sigma'_{12}\frac{\left|\sigma_{12}\right|\sigma'_{12}}{\left|\sigma_e\right|\sigma'_{01}} A_1^{(2)}(\tau_2,\tau_1)
\end{aligned}
\qquad (165)
$$

The expression for the low-fluence component $A_0^{(2)}(\tau_2,\tau_1)$ has already been used to analyze data in chapter 4 (eq 121) and is no different than if the fluence dependent terms had been neglected from the start. The normalization removes all the simple, size-reducing contributions to the fluence-induced component $A_1^{(2)}(\tau_2,\tau_1)$ and leaves only the last, shape-changing terms in eqs 163 and 164:

$$
A_1^{(2)}(\tau_2,\tau_1) = \tfrac{1}{2}e^{i\Phi_{12}}\Big(C_{2'2'}(\tau_2,\tau_1) + C_{2'1'}(\tau_2,\tau_1)\Big) \qquad (166)
$$

5.2.4 Analyzing 2D Fluence-Induced Data.

The MUPPETS data has a strong fluence dependence that changes the early, rising signal into a decay (Figure 4.8A–B). This behavior can now be explained. Focusing on the τ_1 = 0 cut through the data is sufficient. Neglecting cross-relaxation and thermal effects and using our current notation, the τ_1 = 0 low-fluence data should fit

$$A_0^{(2)}(\tau_2,0) = e^{i\Phi_e} C_{1'}(\tau_2) - \frac{1}{2}\frac{|\sigma_{12}|\sigma'_{12}}{|\sigma_e|\sigma'_{01}} e^{i\Phi_{12}} C_{2'}(\tau_2) \qquad (167)$$

(cf. eq 114). The initial rise in the signal is due to the decay of the negative biexciton signal. The same cut of the fluence-induced data has now been predicted to be (eq 166)

$$A_1^{(2)}(\tau_2,0) = e^{i\Phi_{12}} C_{2'}(\tau_2) \qquad (168)$$

Comparing eqs 167 and 168, as the fluence is increased, the negative biexciton signal will be reduced, canceled and eventually replaced by a positive biexciton contribution. This is exactly the pattern seen in Figure 4.8A–B, and these equations fit the data well using the parameters already determined in chapter 4. Thus, the qualitative behavior of the MUPPETS at high fluence is explained.

On a quantitative basis, the fluence-induced MUPPETS signal (eq 168) is predicted to be exactly the same as the fluence-induced 1D signal (eq 113, neglecting cross-relaxation and thermal effects):

$$A_1^{(2)}(\tau_2,0) = A_1^{(1)}(\tau_2) \qquad (169)$$

The comparison between MUPPETS and transient-grating data is shown in Figure 5.3. The two signals are identical, as predicted. No new information is gained, but the agreement indicates that no unanticipated states, species or phenomena are accessed in the MUPPETS experiments under the current experimental conditions, even at the highest fluences.

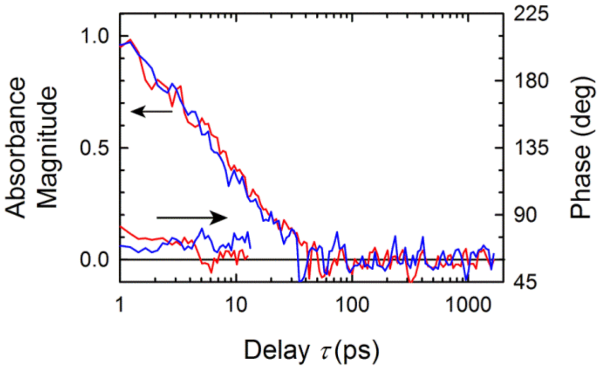

Figure 5.3. Fluence-induced component of the MUPPETS data at $\tau_1 = 0$, $A_1^{(2)}(\tau,0)$ (blue, from Figure 4.8C–D) compared to the fluence-induced transient-grating data $A_1^{(1)}(\tau)$ (red, from Figure 4.5C–D). Both experiments are predicted to give the biexciton decay $C_{2'}(\tau)$ and are in good agreement.

Huxter and Scholes reported biexciton lifetimes of CdSe nanoparticles using a high-order grating technique.[67] Their technique is similar to MUPPETS with τ_1 fixed to zero, and they also used band-edge excitation to avoid creating triexcitons. They did not specifically comment on the fluence dependence of their results or the relative signs or amplitudes of the components assigned to excitons and biexcitons. However, the results found here show that these factors have little effect on the time constants measured. The biexciton decay is the only new component added, whether saturation occurs or does not.

Expanding our scope to include $\tau_2 > 0$ brings the new biexciton–biexciton correlation function $C_{2'2'}(\tau_2, \tau_1)$ into play (eq 166). The biexciton and exciton have already been shown to be uncorrelated, $C_{2'1'}(\tau_2, \tau_1) = C_{2'}(\tau_2)C_{1'}(\tau_1)$ (chapter 4, section 4.5), so the two limiting possibilities are that the biexciton dispersion is homogeneous, $C_{2'2'}(\tau_2, \tau_1) = C_{2'}(\tau_2)C_{2'}(\tau_1)$, and

$$A_1^{(2)}(\tau_2,\tau_1) = \tfrac{1}{2} e^{i\Phi_{12}} C_{2'}(\tau_2)\Big(C_{2'}(\tau_1) + C_{1'}(\tau_1)\Big) \tag{170}$$

or the dispersion is heterogeneous, $C_{2'2'}(\tau_2, \tau_1) = C_{2'}(\tau_2 + \tau_1)$, and

$$A_1^{(2)}(\tau_2,\tau_1)=\tfrac{1}{2}e^{i\Phi_{12}}\left(C_{2'}(\tau_2+\tau_1)+C_{2'}(\tau_2)C_{1'}(\tau_1)\right) \tag{171}$$

These two cases are only distinguishable when τ_1 is near the biexciton half-life τ_b. If $\tau_1 \ll \tau_b$, then eq 168 holds. On the other hand, if $\tau_1 \gg \tau_b$, then $C_{2'2'}(\tau_2,\tau_1)\approx 0$, and eq 166 reduces to

$$A_1^{(2)}(\tau_2,\tau_1)=\tfrac{1}{2}e^{i\Phi_{12}}C_{2'1'}(\tau_2,\tau_1); \quad \tau_1 \gg \tau_b \tag{172}$$

Either limit is insensitive to the heterogeneity of the rate dispersion.

Our data are shown in Figure 5.4A. No change in shape with τ_1 is evident, a result that is consistent with eq 170. However, only the data set with τ_1 = 10 ps is in the sensitive range, and the biexciton–biexciton correlation is diluted by averaging with the biexciton–exciton correlation function (eq 166).

To judge the expected effects, calculations for the data assuming biexciton heterogeneity (eq 171) and the 1D functions measured in chapter 4 are shown in Figure 5.4B. If the biexciton relaxation were homogeneous (eq 170), all the curves in this figure would be identical. With an assumption of heterogeneity, there is a difference, and it is largest for τ_1 = 10 ps, as expected. However, the effect is quite small, and the current data cannot comment on the heterogeneity of the biexciton decay. Although we do not gain any new information from Figure 5.4, it does further confirms the completeness of the theory.

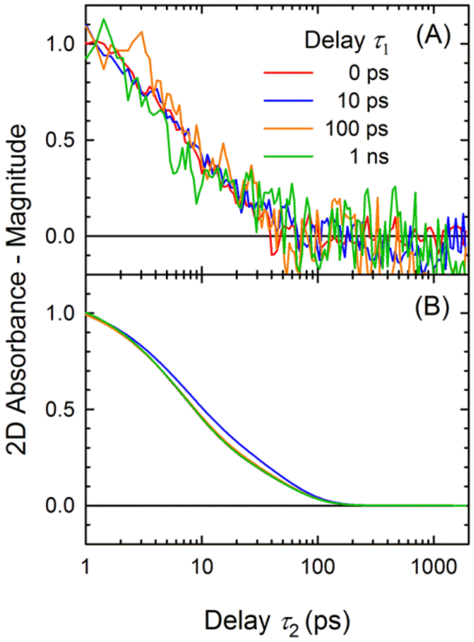

Figure 5.4. Fluence-induced component of the MUPPETS data at various values of τ_1. These data are governed by biexciton dynamics. (A) Magnitude of $A_1^{(2)}(\tau_2, \tau_1)$. (The phases given in the Supporting Information.) (B) Calculations corresponding to (A) with the assumption of a heterogeneous biexciton decay. A homogeneous decay would give identical curves. The experiments are consistent with theory, but must be redesigned to extract meaningful new information.

Although this data set is not ideal for measuring biexciton–biexciton heterogeneity, these calculations show how the measurements could be improved. More data should be taken over the range of τ_1 corresponding to the biexciton decay. In addition, the fluence of the second excitation should be kept low and only the fluence of the first should be increased. In this case, the set of pathways in Figure 5.2C, which contribute $C_{2'1'}(\tau_2, \tau_1)$ to eq 166, would be eliminated, and only those in Figure 5.2B, which create $C_{2'2'}(\tau_2, \tau_1)$, would be retained.

5.3 THERMAL EFFECTS: THEORY

The analysis of in chapter 4 of the paper ignored any signal from heating of the solvent, but in principle, all of the transient-grating and MUPPETS measurements at long times could be perturbed by thermal effects. Some measurements (e.g., Figure 4.9B) appear to have a thermal signal; others are more ambiguous. This section develops the theory, methods and analysis needed to quantify the thermal effects in all these measurements.

Methods to extend the pathway formalism to thermal signals have been developed for two-level systems[18] and also for excitonic systems.[66] These methods and notation are reviewed in subsection 5.3.1 to set-up the calculations in subsection 5.3.2, the extension to fluence-induced data in subsection 5.3.3 and the comparison to data in section 5.4.

5.3.1 Including Thermal Signals in Pathways.

The calculations are greatly simplified by the linearity of the solvent thermal response. As a result, only heat generated in the final time period is detectable.[18] The generalized absorbance due to thermal effects $A_{\varepsilon}^{(N)}(\tau_N,\ldots,\tau_1)$ is calculated from[66]

$$\begin{aligned} A_{\varepsilon}^{(N)}(\tau_N,\ldots,\tau_1) = (-1)^N \rho L\,[\sigma_{\varepsilon} \,|\, C_{\varepsilon}(\tau_N) \\ \times \mathbf{G}_{\varepsilon}(?\,\Gamma + t_{N-1}, t_{N-1})\mathbf{T}_N \ldots \mathbf{G}(t_1, t_0)\mathbf{T}_1 \,|\, eq] \end{aligned} \tag{173}$$

and adds to the fully resonant absorbance (eq 131). The solute time evolution between times $t_{N\text{-}1}$ (the time of the final excitation) and t_N (the time of the probe) $\mathbf{G}(t_N, t_{N\text{-}1})$ is replaced by a product of the thermal-response function $C_{\varepsilon}(\tau_N)$ and the thermal yield $\mathbf{G}_{\varepsilon}(\tfrac{1}{4}\Gamma + t_{N\text{-}1}, t_{N\text{-}1})$. The operator $\mathbf{G}_{\varepsilon}(t_1, t_0)$ measures the total amount of heat deposited in the solvent at time t_1 from electronic states populated at time t_0.

The thermal-response function $C_{\varepsilon}(\tau_N)$ gives the change in index-of-refraction of the solvent at time τ_N due to heat deposited at time zero. It consists of a purely thermal component, which decays slowly on our timescale, and an acoustic component with a period Γ. Over short times, it is sufficient to use the simple approximation[18]

$$C_\varepsilon(\tau_N) = 1 - \cos(\tau_N / \Gamma) \tag{174}$$

The acoustic period is calculated from the experimental geometry and the speed-of-sound of the solvent. In our system, ¼Γ = 1.27 ns. Thus the biexciton decay is nearly instantaneous compared to the thermal response, but the exciton decay is not.

Equation 173 makes the approximation that any heat deposition before ¼Γ (half way to the first maximum) is instantaneous and any heat deposited after ¼Γ has no effect. This approximation is reasonable for the CdSe/Zn exciton decay, which has significant components before and after ¼Γ, but only a small decay in the region near ¼Γ. Under this approximation, $\mathbf{G}_\varepsilon(\tfrac{1}{4}\Gamma+t_{N-1}, t_{N-1})$ does not contribute to the time evolution of the signal, and convolutions are avoided.

In eq 173, the states describing the system must be expanded to $|P\ n_\varepsilon]$. The electronic state of the solute is P, as before. The added variable n_ε measures the change in solvent energy as the number of excitation photons of frequency ω that are converted to heat per solute.[66] Because thermal effects are only created over the last time period, the variable n_ε can be suppressed during earlier periods (see, for example, Figures 5.5 and 5.6).

The other new element in eq 173 is the thermal-detection vector $[\sigma_\varepsilon|$.[66] It has components

$$\left(\sigma_\varepsilon\right)^{i n_\varepsilon} = i\sqrt{2}\sigma''_\varepsilon \delta^i_{0'} n_\varepsilon \tag{175}$$

where i is the solute electronic state in the exciton basis set. It is purely imaginary, as expected for a nonresonant process. The magnitude of the thermal signal is determined by the thermal cross-section σ_ε'', which is defined by

$$\sigma''_\varepsilon = \frac{\omega}{c}\left(1+\frac{1}{n_s^2}\right)\left(\frac{-dn_s}{d\rho_s}\right)\left(\frac{d\rho_s}{d\varepsilon_s}\right)\hbar\omega \tag{176}$$

where n_s is the solvent index-of-refraction, and ρ_s is the solvent density. Although σ_ε'' is a property of the solvent, it has the units of a cross-section and plays a role analogous to a solute absorption cross-section.

Equation 173 can be expanded into pathways by inserting sets of states between the operators. The result is

$$\begin{aligned}\frac{A_\varepsilon^{(N)}(\tau_N,\ldots,\tau_1)}{A'^{(0)}} &= (-1)^N I^N \left[(\sigma_\varepsilon)^{nq} (\sigma_T)_m^l \ldots (\sigma_T)_k^j \right] \\ &\times C_\varepsilon(\tau_N) \Big\langle (G_\varepsilon)_{nq}^{mp} (?\ \Gamma + t_{N-1}\ t_{N-1} \\ &\times G_l^k(t_{N-1},t_{N-2}) \ldots G_j^{1'}(t_1,t_0) \Big\rangle \end{aligned} \tag{177}$$

(cf. eqs 137 and 138). Where double indices occur, the first refers to the solute electronic state and the second to the solvent energy.

In the exciton basis set, the selection rules on $(G_\varepsilon)_{nq}^{mp}(t_1,t_0)$ are quite restrictive. The only nonzero elements are

$$(G_\varepsilon)_{0'1}^{1'0}(t_1,t_0) = \frac{Q_1}{\sqrt{2}} \left(1 - G_{1'}^{1'}(t_1,t_0) \right). \tag{178}$$

and

$$(G_\varepsilon)_{0'1}^{2'0}(t_1,t_0) = \frac{Q_2}{\sqrt{2}} \left(1 - G_{2'}^{2'}(t_1,t_0) \right) - \frac{Q_1}{\sqrt{2}} G_{1'}^{2'}(t_1,t_0). \tag{179}$$

In our model, we have allowed for the possibility that the exciton or biexciton may decay to a high energy "trap" state, and thus, does not release heat to the solvent. The fraction of the energy released as heat is Q_1 or Q_2 for the exciton or biexciton respectively. The derivation of eqs 178 and 179 is given in the Supporting Information.

5.3.2 Calculating Low-Fluence Thermal Signals.

The sequence of operators that creates the low-fluence, 1D thermal absorbance is

$$A_{\varepsilon \mathrm{A}}^{(1)}(\tau_1) = +\rho I [\sigma_\varepsilon | C_\varepsilon(\tau_1) \mathbf{G}_\varepsilon (? \, \Gamma + t_0 \;\; t_0 \;\; \mathbf{T}_1 \;\; eq \tag{180}$$

There is only one allowed pathway (Figure 5.5A) just as there is only one low-fluence, fully resonant pathway (Figure 5.1A and eq 139). This pathway gives a contribution to the absorption of

$$\frac{A_{\varepsilon \mathrm{A}}^{(1)}(\tau_1)}{A'^{(0)}} = -i\sigma_\varepsilon'' I C_\varepsilon(\tau_1) Q_1 \left(1 - C_{1'}(? \, \Gamma \;\right) \tag{181}$$

(c.f. eq 146).

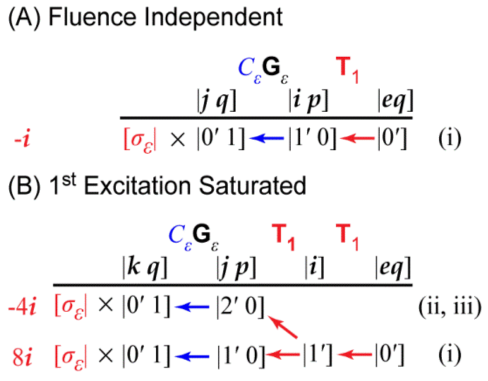

Figure 5.5. Pathways used to calculate the thermal signal in 1D (pump–probe and transient-grating) experiments, including the fluence dependence. The format is explained in the Figure 5.1 caption. The time dependence (blue) is governed by the solvent thermal-response operator C_ε. The yield of solvent energy is given by $\mathbf{G}_\varepsilon$. The relative weights (left) are shown here for the simple case $\sigma_\varepsilon'' = 1$ and $\mathbf{G}_\varepsilon = 1$. The indices on each pathway (right) indicate the corresponding resonant pathways in Figure 5.1. The later states $|P\, n_\varepsilon]$ are expanded to include the number of photons converted to solvent heat n_ε. (A) Pathways with no fluence dependence. (B) Pathways with fluence dependence due to two interactions with the excitation pulses. (C) Pathways with fluence dependence due to two interactions with the detection pulses.

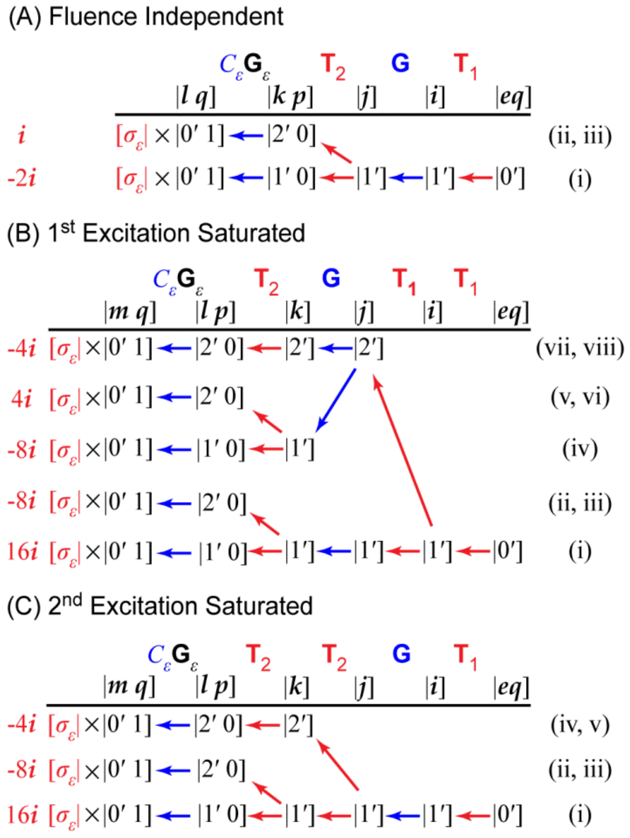

Figure 5.6. Pathways used to calculate the thermal signal in 2D (MUPPETS) experiments. The format is explained in the captions to Figures 5.1 and 5.5. The indices on each pathway indicate the corresponding resonant pathways in Figure 5.2. (A) Pathways with no fluence dependence. (B) Pathways with fluence dependence due to two interactions with the excitation pulses. (C) Pathways with fluence dependence due to two interactions with the detection pulses.

The sequence of operators that creates the low-fluence, 2D thermal absorbance is

$$A_{\varepsilon\mathrm{A}}^{(2)}(\tau_2,\tau_1) = \rho L\,[\sigma_\varepsilon\,|\,C_\varepsilon(\tau_2)\mathbf{G}_\varepsilon(?\ \Gamma + t_1\ t_1\ \mathbf{T}_2 \\ \times\mathbf{G}(t_1,\,t_0)\mathbf{T}_1\,|\,eq] \tag{182}$$

It is expanded to two pathways in Figure 5.6A, whereas the corresponding fully resonant signal $A_{\mathrm{A}}^{(2)}(\tau_2,\tau_1)$ has three pathways (Figure 5.2A). However, eq 179 has two terms for the detection of the biexciton state, the first associated with diagonal biexciton decay and the second with cross-relaxation. When the thermal pathways are evaluated, they give three terms,

$$\begin{aligned}\frac{A^{(2)}_{\varepsilon\mathrm{A}}(\tau_2,\tau_1)}{A'^{(0)}} = {} & -i\sigma''_{\varepsilon} I^2 C_{\varepsilon}(\tau_2)\Big[2\sigma'_{01}Q_1\big(C_{1'}(\tau_1) \\ & -C_{1'1'}(?\ \Gamma\ \tau_1\ \big)+\sigma'_{12}Q_1 C^{2'}_{1'1'}\ \ \Gamma\ \tau_1 \\ & -\sigma'_{12}Q_2\big(C_{1'}(\tau_1)-C_{2'1'}(?\ \Gamma\ \tau_1\ \big)\Big]\end{aligned} \tag{183}$$

An important result of this calculation is that for each resonant pathways in Figure 5.2A there is a corresponding thermal term in eq 183. During τ_2, the first terms in both eqs 147 and 183 concern exciton dynamics, the second terms involve cross-relaxation, and the last terms deal with biexciton dynamics. The correspondence between resonant and thermal pathways is indicated in Figures 5.5 and 5.6 by labeling with the corresponding indices from Figures 5.1 and 5.2.

5.3.3 Calculating Fluence-Induced Thermal Signals.

Following the methods of section 5.2, the calculation of thermal effects can by extended to the first-order, fluence-induced signals. In 1D, the first excitation can have a double interaction, leading to a thermal contribution to the absorbance

$$A^{(1)}_{\varepsilon\mathrm{B}}(\tau_1) = -\phi L\,[\![\sigma_{\varepsilon}\,|\,C_{\varepsilon}(\tau_1)\mathbf{G}_{\varepsilon}(?\ \Gamma+t_0\ \ t_0\ \ \mathbf{T}_1\mathbf{T}_1\ \ eq \tag{184}$$

This term expands into two pathways (Figure 5.5B). Evaluating those pathways leads to three terms in the thermal absorbance

$$\begin{aligned}\frac{A^{(1)}_{\varepsilon\mathrm{B}}(\tau_1)}{A'^{(0)}} = {} & 4i\sigma''_{\varepsilon} I^2 C_{\varepsilon}(\tau_1)\Big[2\sigma'_{01}Q_1\big(1-C_{1'}(?\ \Gamma\ \big) \\ & +\sigma'_{12}C^{2'}_{1'}(?\ \Gamma\ -\sigma'_{12}Q_2\big(\ -(C_{2'}\ \ \Gamma\ \big)\Big]\end{aligned} \tag{185}$$

A factor of $\varepsilon_2 = 4$ to account for phase-matching degeneracy is included in eq 185 and in the weights given in Figures 5.5 and 5.6. These three terms are in one-to-one correspondence with the corresponding resonant absorbance (eq 152). Because the thermal-grating signal requires time to develop, there is no effect from two interactions with the detection pulses, i.e., no analog of the pathways in Figure 5.5C.

A similar approach in 2D generates signals due to double interaction of the first pulse

$$A_{\varepsilon\mathrm{B}}^{(2)}(\tau_2,\tau_1) = \rho L\,[\sigma_\varepsilon\,|\,C_\varepsilon(\tau_2)\mathbf{G}_\varepsilon\mathbf{T}_2\mathbf{G}(t_1,\ t_0)\mathbf{T}_1\mathbf{T}_1\,|\,eq] \tag{186}$$

or with the second pulse

$$A_{\varepsilon\mathrm{C}}^{(2)}(\tau_2,\tau_1) = \rho L\,[\sigma_\varepsilon\,|\,C_\varepsilon(\tau_2)\mathbf{G}_\varepsilon\mathbf{T}_2\mathbf{T}_2\mathbf{G}(t_1,\ t_0)\mathbf{T}_1\,|\,eq] \tag{187}$$

These correspond to the expressions for saturation of the 2D resonant signal $A_{\mathrm{B}}^{(2)}(\tau_2,\tau_1)$ and $A_{\mathrm{C}}^{(2)}(\tau_2,\tau_1)$ (eqs 158 and 159). Expansion of eqs 186 and 187 leads to the pathways shown in Figure 5.6B and 5.6C, respectively. The number of terms is large, so we make a detailed evaluation in limits that apply to our system: any term involving cross-relaxation is dropped, and the biexciton relaxation is fast relative to Γ. Evaluating them gives

$$\begin{aligned}\frac{A_{\varepsilon\mathrm{B}}^{(2)}(\tau_2,\tau_1)}{A'^{(0)}} &= 4i\sigma''_\varepsilon I^3 C_\varepsilon(\tau_2)\\ &\times\Big[\left(2\sigma'_{01}\right)^2 Q_1\left(C_{1'}(\tau_1)-C_{1'1'}(?\ \Gamma\ \tau_1\ ,)\right.\\ &-\sigma'_{12}\left(2\sigma'_{01}\right)Q_2\left(C_{1'}(\tau_1)-C_{2'1'}(?\ \Gamma\ \tau_1\ ,)\right.\\ &-\left(\sigma'_{12}\right)^2 Q_2\left(C_{2'}(\tau_1)-C_{2'2'}(?\ \Gamma\ \tau_1\ )\right)\Big]\end{aligned} \tag{188}$$

which is based on pathways i, iii, and viii, and

$$\begin{aligned}\frac{A_{\varepsilon\mathrm{C}}^{(2)}(\tau_2,\tau_1)}{A'^{(0)}} &= 4i\sigma''_\varepsilon I^3 C_\varepsilon(\tau_2)\\ &\times\Big[\left(2\sigma'_{01}\right)^2 Q_1\left(C_{1'}(\tau_1)-C_{1'1'}(?\ \Gamma\ \tau_1\ ,)\right.\\ &-\sigma'_{12}\left(2\sigma'_{01}\right)Q_2\left(C_{1'}(\tau_1)-C_{2'1'}(?\ \Gamma\ \tau_1\ ,)\right.\\ &-\left(\sigma'_{12}\right)^2 Q_2\left(C_{1'}(\tau_1)-C_{2'1'}(?\ \Gamma\ \tau_1\ )\right)\Big]\end{aligned} \tag{189}$$

which is based on pathways i, iii, and v.

5.4 THERMAL EFFECTS: COMPARISON TO DATA

5.4.1 Including Thermal Signals in the Fit-Free Analysis.

Chapter 4 of this paper drew a number of conclusions based on direct comparisons between different sets of data, without any fitting required.[108] In this section, we examine whether including thermal effects changes the validity of those comparisons. The analysis is aided by following the correspondence between fully resonant and thermal terms.

We first consider the comparison of MUPPETS decay slices in τ_2 at different values of τ_1 (Figure 4.10). The discussion is simplified by introducing three functions that represent the size of the thermal effects associated with the three resonant MUPPETS pathways:

$$d_{1'1'}(\tau_1) = \frac{\sigma''_{\varepsilon}}{|\sigma_e|} Q_1 \left(C_{1'}(0) - \frac{C_{1'1'}(?\;\mathrm{I}\!\Gamma\;\tau_1}{C_{1'}(\tau_1)} \right) \tag{190}$$

$$d^{2'}_{1'1'}(\tau_1) = \frac{\sigma''_{\varepsilon}}{|\sigma_e|} Q_1 \left(C^{2'}_{1'}(0) - \frac{C^{2'}_{1'1'}(?\;\mathrm{I}\!\Gamma\;\tau_1}{C_{1'}(\tau_1)} \right) \tag{191}$$

and

$$d_{2'1'}(\tau_1) = \frac{\sigma''_{\varepsilon}}{|\sigma_{12}|} Q_2 \left(C_{2'}(0) - \frac{C_{2'1'}(?\;\mathrm{I}\!\Gamma\;\tau_1}{C_{1'}(\tau_1)} \right) \tag{192}$$

The first function $d_{1'1'}(\tau_1)$ is associated with the exciton–exciton pathway (Figures 5.2A.i and 4.2A), the second $d^{2'}_{1'1'}(\tau_1)$ is associated with the cross-relaxation (Figures 5.2A.ii and 4.2B), and the third $d_{2'1'}(\tau_1)$ is associated with the exciton–biexciton pathway (Figures 5.2I.iii and 4.2C).

After the fully resonant (eq 147) and thermal signals (eq 182) are added, the total is normalized (eq 105), and the low-fluence component is taken (eq 165), the result is

$$\begin{aligned} A_0^{(2)}(\tau_2,\tau_1) = & \left(e^{i\Phi_e} C_{1'1'}(\tau_2,\tau_1) - i d_{2'1'}(\tau_1) C_\varepsilon(\tau_2) C_{1'}(\tau_1)\right) \\ & -\frac{1}{2}\frac{\sigma'_{12}}{\sigma'_{01}}\left(e^{i\Phi_e} C_{1'1'}^{2'}(\tau_2,\tau_1) - i d_{1'1'}^{2'}(\tau_1) C_\varepsilon(\tau_2) C_{1'}(\tau_1)\right) \\ & -\frac{1}{2}\frac{|\sigma_{12}|\sigma'_{12}}{|\sigma_e|\sigma'_{01}}\left(e^{i\Phi_{12}} C_{2'1'}(\tau_2,\tau_1) - i d_{2'1'}(\tau_1) C_\varepsilon(\tau_2) C_{1'}(\tau_1)\right) \end{aligned} \tag{193}$$

Each resonant term (the first term within each set of parentheses) has an associate thermal term (the second term in each set of parentheses) with a similar size and sign. The thermal cross-relaxation $d_{1'1'}^{2'}(\tau_1)$ will be small whenever the resonant cross-relaxation $C_{1'1'}^{2'}(\tau_2,\tau_1)$ is small (eq 191). (The $C_{1'}^{2'}(0)$ = 0 term is only included to show symmetry.) Also, the signs of the exciton–exciton and exciton–biexciton thermal terms, $d_{1'1'}(\tau_1)$ and $d_{2'1'}(\tau_1)$ respectively, have opposite signs, just as the resonant terms do.

The thermal terms in eq 193 are always separable in τ_1 and τ_2. In general, this result will complicate the interpretation of the MUPPETS data, because in many models (for example, Figure 4.11B–D), the resonant terms are not separable. In those cases, detailed modeling of the thermal effects is necessary to correctly interpret the data.

However, in one case, when the exciton decay is homogeneous and the biexciton decay is uncorrelated with the exciton decay (see Figure 4.11A), the resonant terms are separable in τ_1 and τ_2, and thus, the total signal is as well. In this case, the slices along τ_2 of the MUPPETS data at different values of τ_1 have identical shapes. Thus Figure 4.10 remains a valid, fit-free test for this model, regardless of the size of any thermal effects. The conclusions of chapter 4 are unchanged.

Section 4.4 in chapter 4 showed that important conclusions can be obtained from the τ_1 = 0 cut of the MUPPETS data by itself. To discuss this case, three constants, $d_{1'}$, $d_{1'}^{2'}$ and $d_{2'}$, are defined as the τ_1 = 0 limits of the three functions in eqs 190–192:

$$d_i^j = d_i^j(0) \tag{194}$$

They are also be associated with 1D exciton, cross-relaxation and biexciton pathways (Figure 5.2A.i–iii, respectively). With these definitions, the $\tau_1 = 0$ slice of the MUPPETS signal (eq 193) becomes

$$\begin{aligned} A_0^{(2)}(\tau_2,0) &= \left(e^{i\Phi_e}C_{1'}(\tau_2) - id_{1'}C_\varepsilon(\tau_2)\right) \\ &\quad -\frac{1}{2}\frac{\sigma'_{12}}{\sigma'_{01}}\left(e^{i\Phi_e}C_{1'}^{2'}(\tau_2) - id_{1'}^{2'}C_\varepsilon(\tau_2)\right) \\ &\quad -\frac{1}{2}\frac{|\sigma_{12}|\sigma'_{12}}{|\sigma_e|\sigma'_{01}}\left(e^{i\Phi_{12}}C_{2'}(\tau_2) - id_{2'}C_\varepsilon(\tau_2)\right) \end{aligned} \tag{195}$$

For comparison, the 1D, low-fluence absorbance is derived from eqs 146, 181, I.104 and 156:

$$A_0^{(1)}(\tau_1) = e^{i\Phi_e}C_{1'}(\tau_1) - id_{1'}C_\varepsilon(\tau_1) \tag{196}$$

In both eqs 195 and 196, the correspondence between resonant and thermal terms is maintained. The low-fluence, 1D signal (eq 196) isolates both the resonant and thermal effects of exciton decay. In the MUPPETS signal (eq 195), the thermal effects of exciton and biexciton decay cancel as the resonant signals do. As a result, the thermal signal is smaller MUPPETS than in 1D measurements.

We next look at the biexciton signal $A_b(\tau)$, which is extracted as the difference between the low-fluence 1D signal and the $\tau_1 = 0$ slice of the MUPPETS data

$$A_b(\tau) = 2\frac{\sigma'_{01}|\sigma_e|}{\sigma'_{12}|\sigma_{12}|}\left(A_0^{(1)}(\tau) - A_0^{(2)}(\tau,0)\right) \tag{197}$$

(cf eq 115). In section 4.2 of chapter 4, the biexciton signal was interpreted as isolating the biexciton decay from the exciton decay, including the exciton decay of photoproducts. A small cross-relaxation term also contributes (see eq 116). When thermal effects are included by putting eqs 196 and 195 into eq 197, the correspondence between resonant and thermal terms is maintained:

$$A_b(\tau) = \left(e^{i\Phi_{12}} C_{2'}(\tau) - i d_{2'} C_\varepsilon(\tau)\right) + \frac{|\sigma_{12}|}{|\sigma_e|}\left(e^{i\Phi_e} C_{1'}^{2'}(\tau) - i d_{1'}^{2'} C_\varepsilon(\tau)\right) \tag{198}$$

Equation 198 extends the interpretation given in chapter 4. The biexciton signal also isolates the component of the thermal signal that is attributable to the biexciton decay $d_{2'}$. The small cross-relaxation term also brings along its small thermal signal $d_{1'}^{2'}$. The exciton thermal effects are eliminated along with its resonant signal.

Chapter 4 directly compared the biexciton signal $A_b(\tau)$ to the fluence-induced component of the 1D signal $A_1^{(1)}(\tau)$ (Figure 4.9B). How this comparison survives the addition of thermal effects depends on the energy of the probe pulses. If the probe pulses are substantially weaker than the excitation pulses, the pathways in Figure 5.1C can be neglected. Adding the absorbances due to the remaining pathways (Figures 5.1A–B and 5.5A–B), normalizing (eq 104), and taking the linear, fluence-induced term (eq 156) gives

$$A_1^{(1)}(\tau) = \left(e^{i\Phi_{12}} C_{2'}(\tau) - i d_{2'} C_\varepsilon(\tau)\right) + \frac{|\sigma_{12}|}{|\sigma_e|}\left(e^{i\Phi_e} C_{1'}^{2'}(\tau) - i d_{1'}^{2'} C_\varepsilon(\tau)\right) \tag{199}$$

The correspondence between resonant and thermal terms still holds. In the absence of photoproducts, $A_b(\tau) = A_1^{(1)}(\tau)$.

However, the experiments in chapter 4 were done with the probe-pulse fluence equal to that of the excitation pulses. This condition does not alter the low-fluence signal, even with the thermal signal included (eq 196). However, it adds the pathways in Figure 5.1C to the fluence-induced signal. Recalculating eq 199 with these terms included gives

$$
\begin{aligned}
A_1^{(1)}(\tau_2) = {} & \left(e^{i\Phi_{12}} C_{2'}(\tau_2) - i d_{2'} C_\varepsilon(\tau_2)\right) \\
& + \frac{|\sigma_e|}{|\sigma_{12}|}\left(e^{i\Phi_e} C_{1'}^{2'}(\tau_2) - i d_{1'}^{2'} C_\varepsilon(\tau_2)\right) \\
& + \left(e^{i\Phi_{12}} C_{2'}(\tau_2) - i \frac{|\sigma_e|\sigma'_{10}}{|\sigma_{12}|\sigma'_{12}} d_{1'} C_\varepsilon(\tau_2) \right)
\end{aligned}
\tag{200}
$$

The last set of terms in parentheses is new. These terms do not change the shapes of either the resonant or thermal signals. However, they do perturb the ratio of resonant- to thermal-signal sizes. Part of the biexciton decay is paired with a thermal effect due to excitons: the strict correspondence between resonant and thermal terms is lost. It is lost because resonant detection is subject to saturation, whereas the nonresonant detection of thermal effects is not.

Fortunately, in our system the timescales of the biexciton decay and the thermal signal are distinct. The direct comparison of $A_b(\tau)$ and $A_1^{(1)}(\tau)$, as in Figure 4.9B, is still valid at times before the thermal signal rises (< 300 ps). At later times, the sizes of the thermals signals may not be identical. In well characterized system, eq 200 allows this effect to be calculated. However, using low energy probe pulses in the 1D measurements would have allowed direct comparison of the two results without calculations.

5.4.2 Measuring the Thermal Cross-Section.

Further analysis of the thermal contributions to the data requires fitting to detailed models. The shape of the thermal response under a wide range of conditions has been discussed previously.[116-118] Here, a simple short-time approximation (eq 174) will be sufficient. The acoustic period, $\Gamma = 5.08$ ns, is known from the speed of sound in toluene[119] and the angle between zero- and first-order diffraction, $\alpha = 2.28^{\circ}$.[18] However, it is not practical to accurately predict the absolute size of the thermal response in the face of numerous experimental imperfections. Fortunately, the results of section 5.3 allow calibration of the relative thermal cross-section $\sigma_\varepsilon''/|\sigma_e|$ from the data already used to calibrate the phase of our signals (Figure 4.4).

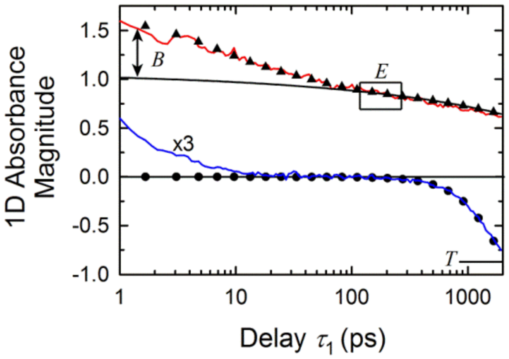

Figure 5.7. Calibration of the thermal cross-section with an external standard. The magnitude of the transient-grating signal $A^{(1)}(\tau_1)$ of azulene in toluene (blue) and CdSe/ZnS in toluene (red) were measured contemporaneously and with the same excitation energy (10.6 nJ/pulse) (from Figure 4.4). The parameters T, E and B are determined from global fits, but the labels indicate the regions that most clearly determine their values. The fit of late azulene data to eq 201 (black circles) yields the thermal amplitude T. The fit of CdSe/ZnS data to eq 202 (black triangles) yields the exciton amplitude E. The difference between the initial data and $EC_{1'}(\tau_1)$ (black solid curve) yields the biexciton amplitude B. These three fit parameters are sufficient to determine the ratio of thermal and resonant cross-sections (eq 203).

Those data are repeated in Figure 5.7. It consists of transient-grating results from CdSe/ZnS nanoparticles and azulene, each in toluene, taken on the same day with no changes to the apparatus. In this analysis of the data, the focus is on the magnitudes of the absorbances, $\left|A_{\text{az}}^{(1)}(\tau_1)\right|$ and $\left|A_{\text{CdSe}}^{(1)}(\tau_1)\right|$ for azulene and CdSe/ZnS, respectively, rather than on their phases. The data for azulene (blue) has a resonant component only before 10 ps, because of the rapid decay of the excited state.[48, 98] After this time, the signal is only due to thermal effects, and the data are described by

$$\frac{\left|A_{\text{az}}^{(1)}(\tau_1)\right|}{A_{\text{az}}^{\prime(0)}} = I\sigma_{\varepsilon}'' C_{\varepsilon}(\tau_1) = TC_{\varepsilon}(\tau_1) \qquad (201)$$

(eq 181 with $Q_1 = 1$ and $C_{1'}(\tfrac{1}{4}\Gamma) = 0$). Using eq 174 for $C_{\varepsilon}(\tau_1)$, the thermal amplitude T is fit.

The CdSe/ZnS data before thermal effects (<300 ps) and neglecting cross-relaxation is described by

$$\begin{aligned}\frac{\left|A^{(1)}_{\text{CdSe}}(\tau_1)\right|}{A'^{(0)}_{\text{CdSe}}} &= \left|I\sigma_e\left(1-16\sigma'_{12}I\right)C_{1'}(\tau_1)+8\sigma_{12}\sigma'_{12}I^2C_{2'}(\tau_1)\right| \\ &= \left|EC_{1'}(\tau_1)+Be^{i\left(\Phi_{12}-\Phi_e\right)}C_{2'}(\tau_1)\right| \qquad (202)\end{aligned}$$

(eqs 146, 152 and 155). Because CdSe has a larger absorption cross-section than azulene, we had to use a pulse energy that created some biexcitons in the CdSe sample to get a strong signal from the azulene solution. Thus, eq 202 contains terms for both saturation of the exciton and formation of the biexciton. The data is fit using the forms for $C_{1'}(\tau_1)$ and $C_{2'}(\tau_1)$ found in chapter 4 (eqs I.106 and I.107) The exciton magnitude E is well determined by the data near 300 ps, after $C_{2'}(\tau_1)$ has fully decayed and before any potential thermal effects begin. The number of biexcitons is measured by B. It is determined primarily by the increase of the initial signal size over that expected from E. Using eqs 201 and 202, one can solve for the ratio of thermal and exciton cross-sections in terms of the fitting parameters

$$\frac{\sigma''_{\varepsilon}}{\left|\sigma_e\right|} = \frac{T}{E}\left[1+2\left(\frac{\sigma'_{12}\left|\sigma_e\right|}{\left|\sigma_{12}\right|\sigma'_{01}}\right)\frac{B}{E}\right]^{-1} = 0.136 \qquad (203)$$

This measurement is robust. The pulse energies and various instrumental factors cancel in taking the ratio of the two measurements. Only the static absorbances $A'^{(0)}$ of the two samples are needed to match their properties. Knowledge of the cross-sections in the system is only needed to calculate the small deviation from one of the factor in parentheses.

5.4.3 Modeling Thermal Effects in the Data.

A notable result from chapter 4 is that good fits to the data were possible without including thermal effects. The absence of thermal effects could imply that the exciton and biexciton decay to relatively high energy trap states without releasing heat. Such a conclusion requires a comparison of the size of predicted effects to the error level of the data. We will show that the thermal signals should exceed the random noise of the experiment, but that systematic errors prevent a firm conclusion.

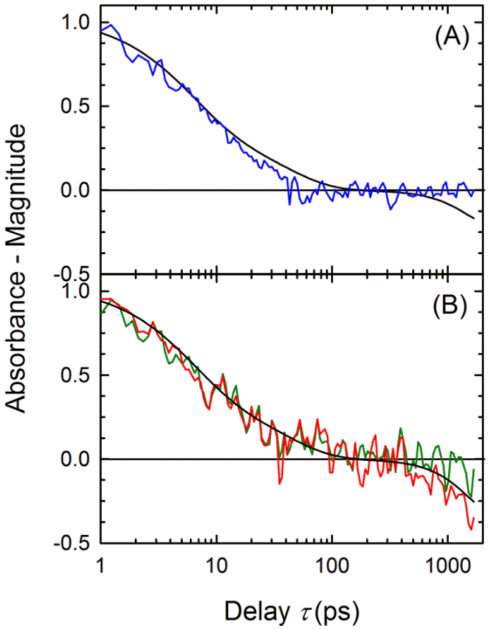

Figure 5.8. Comparison of the calculated biexciton thermal signal with $Q_2 = 1$ (black) to various measurements. (A) The fluence-induced transient-grating magnitude $\left|A_1^{(1)}(\tau)\right|$ (blue, from Figure 4.5C) does not show a thermal signal at long times. (B) The biexciton signal derived from MUPPETS measurements changes with the 1D decay used in the calculation. Using transient-grating data (red, same as Figure 4.9B) is consistent with a strong thermal signal. Using the pump–probe-based model of chapter 4 (green) is not.

The absence of a thermal signal is clearest in the fluence-induced transient-grating data $A_1^{(1)}(\tau)$ (Figure 5.8A). According to eq 200, the biexciton decay at short time should be accompanied by a long-time signal from the heat released by the biexciton decay. However, the data show no signal at long time. Figure 5.8A also shows the predicted thermal signal (eq 200) if $Q_2 = 1$, i.e., if all the biexciton energy were released as heat. Although the predicted size is smaller than the resonant signal, it should be visible above the experimental noise. These data imply that $Q_2 \approx 0$.

In contrast, the biexciton signal $A_b(\tau)$, shown previously in Figure 4.9B and repeated in Figure 5.8B (red), does show a pronounced long time signal. Calculations with $Q_2 = 1$ (eq 198) are consistent with its size and shape. (The calculations for $A_b(\tau)$ and $A_1^{(1)}(\tau)$ are different due to probe saturation. This effect is not sufficient to explain the difference between these data sets.)

That biexciton signal was calculated by using the transient-grating data to represent $A_0^{(1)}(\tau)$ in eq 197. It is also possible to use the model for $C_{1'}(\tau)$ defined in section 4.3.2 of chapter 4. This calculation yields the green data in Figure 5.8B. In this version of the biexciton signal, the thermal signal is missing, again suggesting $Q_2 \approx 0$.

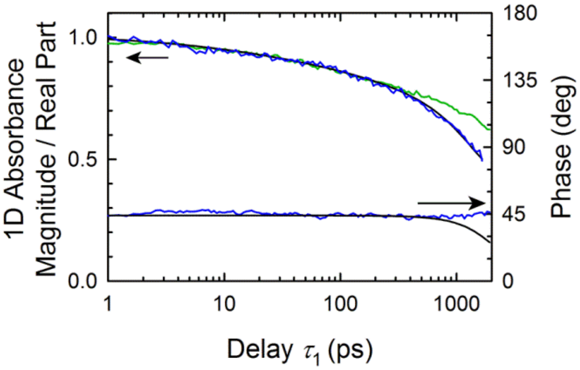

Figure 5.9. Comparison of low-fluence 1D measurements: real pump–probe (green, from Figure 4.6B) and complex transient-grating (blue, from Figure 4.5C–D) data. The transient-grating magnitude can be accounted for by adding an imaginary, thermal component to the pump–probe results (black curves), but in that case, the phase of the transient-grating should not be constant.

The difficulty in measuring the heat yield from the biexciton decay Q_2 is mirrored by a difficulty in measuring the heat yield from the exciton decay Q_1. Both problems originate in a discrepancy between the pump–probe and transient-grating data at long times. These two 1D data sets are compared in Figure 5.9. The pump–probe measurement should be the real part of the complex transient-grating signal. The pump–probe data and the transient-grating magnitude are the same at early times, and the transient-grating phase is constant. These early data are consistent with each other. At long times, the pump–probe data and the transient-grating magnitude diverge. This difference could be accounted for by including an imaginary thermal signal, which would only affect the transient-grating data. A calculation using the pump–probe fit (eq 106) for $C_1'(\tau_1)$ and $Q_1 = 1$ for the thermal effect (eq 196) is shown, and it matches the transient-grating magnitude quite well. Unfortunately, the thermal-grating phase is constant at long times, which is inconsistent with a significant, imaginary thermal contribution, as shown in Figure 5.9. Thus, the transient-grating phase implies $Q_1 = 0$, whereas the comparison of pump–probe and transient-grating magnitudes suggest $Q_1 = 1$. The ambiguity in the 1D data also translates into the calculation of the biexciton signal (Figure 5.8) and thus into determining the thermal yield from the biexciton Q_2.

The last set of data to consider is the MUPPETS data by itself. As argued above, the qualitative interpretation of the MUPPETS data (e.g., Figure 4.10) is independent of the size of the thermal contribution. However, quantitative modeling depends on the 1D response, including its thermal component. In chapter 4, a hybrid model was used to fit the MUPPETS data: the magnitude of $C_1'(\tau_1)$ was taken from the pump–probe fit, but the phase was taken as a constant, as given by the transient-grating experiments. The constant-phase assumption correctly accounts for the MUPEPTS phase and magnitude (Figure 4.11). The lack of a thermal contribution to the MUPPETS phase means that $2Q_1 = Q_2$ and implies that $Q_1 < 0.5$, at least.

It is also possible to model the MUPPETS data using $Q_2 = 1$ along with the model in Figure 5.9 that reconciles the pump–probe and transient-grating magnitude ($Q_1 = 1$). The magnitude of the MUPPETS data can be fit correctly this way, but the predicted phase is no longer correct (not shown), as with the 1D data in Figure 5.9.

In conclusion, the discrepancy between pump–probe and transient-grating data is not large enough to affect any of the conclusions about the exciton and biexciton conclusion in chapter 4. However, they create enough uncertainty to prevent a conclusion regarding the role of trap states in the decay.

The inconsistency between pump-probe and transient-grating measurements persisted despite repeated measurements of both. It must be attributed to an unresolved instrumental error. We point out that this problem would not be noticed without a complete measurement of both pump–probe and phase-resolved transient-grating data with calibrated, absolute phases. These measurement may appear to be redundant, but their comparison is an important control for systematic errors.

5.5 SUMMARY

This paper has looked at secondary processes that have the potential to interfere with the interpretation of MUPPETS experiments, specifically saturation and solvent heating. It serves three different ends: it derives the theory needed to calculate these effects, it shows that these effects do not alter the conclusions of chapter 4 of the paper,[108] and it provides a specific example of these effects to aid in designing and analyzing future experiments.

The incoherent-pathway formalism[16, 17] has been extended to allow a systematic calculation of fluence-induced effects, thermal effects and even fluence-induced thermal effects in MUPPETS experiments. Although these processes are well understood in 1D experiments, the methods presented here provide a convenient method for calculating them. It is particularly useful in heterodyned experiments on multilevel systems, where multiple transitions with different phases must be considered.

In contrast, the calculation of fluence-induced effects in MUPPETS is new. The change in sign of the biexciton signal with increasing fluence was satisfactorily explained. The ability to quantitatively model this $\chi^{(7)}$ experiment increases our confidence that our model for CdSe is complete and that no unexpected species, such as triexcitons or photoproducts, occur under our conditions. In general, understanding fluence-induced effects is important in high order spectroscopies such as MUPPETS, as high fluences are often needed to obtain sufficient signal size.

A new correlation function $C_{2'2'}(\tau_2, \tau_1)$, which has information on the heterogeneity of the biexciton decay, is accessible, in principle, by deliberately creating and measuring a fluence-induced signal. Although the current data set addresses this point poorly, the theory suggests methods for improving the experimental design to address this quantity.

In the calculations, processes detected through solvent heating were placed on the same footing as resonantly detected processes. This approach led to a robust method of predicting the size of thermal signals using an external standard. In principle, this method can lead to the identification of spectroscopically dark, trap states. The low ratio of thermal to resonant cross-sections in this system along with small inconsistencies in the 1D data undermined this approach here. However, the obstacles that must be overcome are now well defined.

Overall, none of the interpretations of chapter 4 are altered by these effects. For example, the comparison of 1D and MUPPETS data to separate exciton and biexciton dynamics is still valid, if we understand these dynamics to include the thermal effects attributable to relaxation across each transition. However, in many cases thermal effects were unimportant only because of specific features of the nanoparticle system studied. For example, the MUPPETS modeling is unaffected by thermal effects only because there is no evidence for exciton heterogeneity or exciton–biexciton correlation. More generally, modeling of thermal effects is important for the quantitative interpretation of MUPPETS results. This paper makes that modeling possible.

CHAPTER 6 TWO-DIMENSIONAL ANISOTROPY MEASUREMENTS SHOWING LOCAL HETEROGENEITY IN A POLYMER MELT

In low viscosity, small-molecule solvents, the anisotropy decay of a solute is usually exponential and yields a well-defined rotation rate.[120, 121] In complex fluids, including polymer melts, the anisotropy decay of a small solute is nonexponential, and the rotation rates are dispersed.[122-132] Standard, one-dimensional (1D) experiments are silent on whether or not this rate dispersion is due to heterogeneity or anisotropy in the local structure of the solvent. We have developed two-dimensional (2D) methods that distinguish between heterogeneous and homogeneous causes of rate dispersion, and we have called them MUPPETS (multiple population-period transient spectroscopy).[11, 13, 16, 17, 21] Up to this time, they have been limited to measuring electronic-state decay. This Letter demonstrates a polarized version of MUPPETS that measures heterogeneity in anisotropy decays and applies this new method to the problem of small-molecule rotation in a polymer melt.

The rotation of solutes in small-molecule solvents has been extensively studied by polarized 1D spectroscopies, such as pump–probe or time-resolved fluorescence.[120, 133] These experiments have a single excitation and a single period of evolution before the final signal detection. The change in absorbance $A^{(1)}(\tau_1; \theta)$ is measured at a time delay τ_1 between the excitation and detection pulses and with an angle θ between their linear polarizations. The standard, 1D anisotropy decay $r^{(1)}(\tau_1)$ is defined by

$$r^{(1)}(\tau_1) = \frac{A^{(1)}(\tau_1;0°) - A^{(1)}(\tau_1;90°)}{A^{(1)}(\tau_1;0°) + 2A^{(1)}(\tau_1;90°)}. \tag{204}$$

Theory relates this quantity to the ratio of two correlation functions. In our notation, these two are $C^{\{2\}}(\tau_1)$, which measures the product of the excited-state population and the second Legendre polynomial $P_2(x)$ of the cosine of the angle change of the transition dipole $\Omega(\tau_1)$, and $C^{\{0\}}(\tau_1)$, which measures the excited-state population free of rotational dynamics (the 0th Legendre polynomial of the angle change). Thus,

$$r^{(1)}(\tau_1) = \frac{2}{5}\frac{C^{\{2\}}(\tau_1)}{C^{\{0\}}(\tau_1)} = \frac{2}{5}\left\langle P_2(\cos\Omega(\tau_1))\right\rangle. \tag{205}$$

If rotation and electronic-state decay are independent, the latter cancels in the ratio, leaving only the rotational dynamics shown on the right-hand side of eq 205.

In small-molecule solvents, hydrodynamic descriptions of solute rotation work well.[120, 121] The rotation is diffusive, and the associated friction is proportional to the macroscopic viscosity. Hydrodynamic models allow for a multiexponential decay of an anisotropic solute, but in practice, deviations from exponential decay are often hard to see in simple solvents. As the solvent molecules become longer, the anisotropy decay can become nonexponential, i.e., dispersed. The shape of the decay changes as the solvent changes, a result incompatible with simple hydrodynamic models. Extending anisotropy measurements to 2D—two excitation pulses and two periods of evolution—will yield information on the cause of this dispersion.

Other complex fluids and other processes also show rate dispersion. Ediger used photobleaching to explore rotational-rate heterogeneity on the seconds timescale close to the glass transition.[134] On shorter timescales, Yang and Richert used temperature dependent fluorescence linewidths to show that heterogeneity in solvation rates exists in a supercooled liquid (1.15–1.4 T_g) in the 1–10 ns time window.[135] Heterogeneity in the rate of isomerization in ionic liquids has been inferred from the excitation-wavelength dependence of fluorescence lifetimes and spectra.[136-138] In an ionic liquid, Fruchey and Fayer used rotational measurements to show that two different solutes have different local environments.[139] In comparison to these methods, a full 2D measurement allows not just the detection of heterogeneity, but a quantitative assessment of the relative contributions of heterogeneous and homogeneous mechanisms to the total dispersion.

We previously studied the 1D anisotropy decay of anthracene in solvents whose chain length ranged between the small-molecule and high polymer limits.[128, 129] As the solvent molecules lengthen, the solvent's viscosity increases dramatically. However, once the solvent length exceeds the solute length, the rotational friction decouples from the viscosity. We also found a transition from exponential to nonexponential decay that occurs when the polymer becomes more than ~4 monomers long. The shape of the decay is then constant as the polymer lengthens further. Other observations of nonexponential rotation fit into this scheme.[123-127]

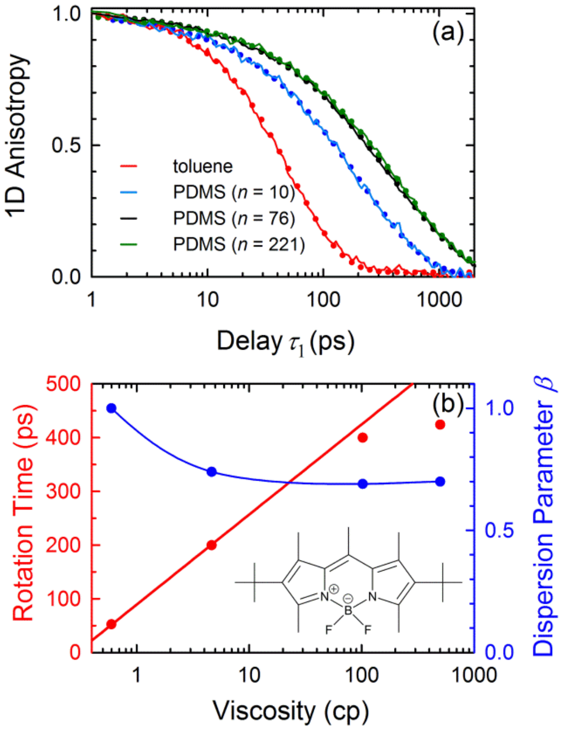

Figure 6.1. 1D measurements of PM597 rotation in toluene and in polymer melts (PDMS) of varying chain length, all at 25 °C. (a) Optical anisotropy decays, $r^{(1)}(\tau_1)/r^{(1)}(0)$, (solid curves) and stretched-exponential ($\exp[-(\tau_1/T)^{\beta}]$) fits (points). (b) Fit parameters from (a) versus macroscopic viscosity η. The rotation time T falls below the linear dependence (red line) of hydrodynamic models. Dispersion appears and saturates as the polymer chain length and viscosity grow. Error estimates fall within the symbols. The blue curve is a guide to the eye showing the trend found in Refs. 9,10. Inset: pyrromethene 597 (PM597).

Figure 1 briefly confirms that the general phenomena found in Refs. 9,10 also apply to the specific system studied here: pyrromethene 597 (PM597) in poly(dimethylsiloxane) (PDMS). Figure 1a shows 1D anisotropy decays (SI), and Figure 1b shows the results of stretched-exponential fits. The rotation time is nearly linear with viscosity for the three smaller solvents, but for the largest, the rotation time no longer increases with the viscosity. In toluene, the decay is well fit by a single exponential (β = 1), showing that the anisotropy of PM597 is minimal. However in the polymer samples, rate dispersion appears ($\beta < 1$) due to solvent interactions.

Two explanations for the rate dispersion are possible. One is development of microheterogeneity.[134, 140, 141] The polymer structure around different solute molecules varies significantly and exerts different levels of rotational friction. In this case, the anisotropy decay of each individual solute molecule is exponential, but averaging over the ensemble of different rates yields a nonexponential decay.

Alternatively, the solvent may develop an anisotropic local structure as its molecules lengthen and, as a result, develop an anisotropic rotational-friction tensor.[122, 124-127] In one such picture, the solute "wobbles" rapidly over a limited cone of angles around a local director determined by the solvent, causing partial decay of the anisotropy.[142] On a longer timescale, the director reorients, completing the anisotropy decay. The combination of these two processes, one fast and one slow, causes the observed rate dispersion. This mechanism is homogeneous. Every solute molecule undergoes the same two phases of relaxation and has an identical, but nonexponential, anisotropy decay.

One-dimensional experiments cannot distinguish between homogeneous and heterogeneous causes of rate dispersion, but 2D methods can. The 2D MUPPETS experiment (Figure 2) uses six, femtosecond optical pulses organized in three simultaneous pairs.[21] The first pair (1*a* and 1*b*) excites the entire ensemble in a spatial grating. During the first evolution period τ_1, the fast subensembles decay. A second pair of pulses (2*a* and 2*b*) attempts to create a second grating, but its formation is perturbed by the grating of surviving molecules. Signal detection is by heterodyned diffraction from

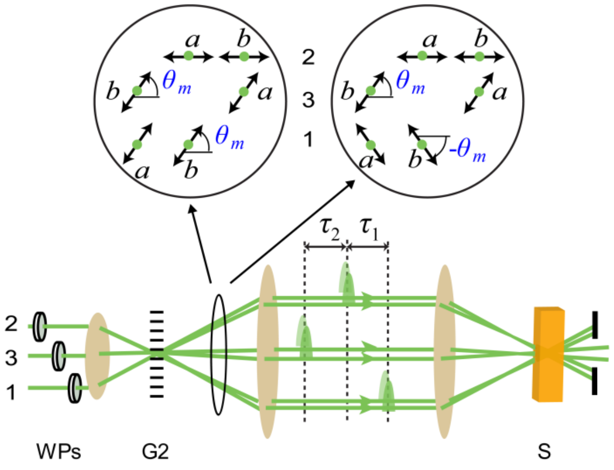

Figure 6.2. Schematic of the set-up that generates the 6-pulse MUPPETS sequence. Three input pulses (1–3, green) with time delays τ_1 and τ_2 have their polarization adjusted by waveplates (WP) before they are split into simultaneous pairs (*a* and *b*) by transmission grating G2. The beams are refocused in the sample S (orange). The two polarization conditions used to measure the 2D anisotropy $r^{(2)}(\tau_2, \tau_1)$ are shown in the cross sections at the top.

the resulting spatial pattern by the third pulse-pair (3*a* and 3*b*). The phase-matching conditions are selected to create a double-difference measurement that isolates the decay during τ_2 of molecules that survive τ_1, i.e., the decay of slowly relaxing molecules. By varying τ_1, the distribution of rate heterogeneity is mapped out. In the absence of distinct rate subensembles, the value of τ_1 has no effect on the decay during τ_2.

We previously analyzed rotational dynamics in MUPPETS using irreducible-tensor methods.[16, 17] Four irreducible correlation functions $C^{\{\ell_2,\ell_1\}}(\tau_2, \tau_1)$ occur, differing by whether rotation does ($\ell_n = 2$) or does not ($\ell_n = 0$) affect the decay during each evolution period τ_n. The 2D anisotropy $r^{(2)}(\tau_2, \tau_1)$ that measures rotational-rate heterogeneity is

$$
\begin{aligned}
r^{(2)}(\tau_2,\tau_1) &= \frac{4}{35}\frac{C^{\{2,2\}}(\tau_2,\tau_1)}{C^{\{0,0\}}(\tau_2,\tau_1)} \\
&= \frac{4}{35}\left\langle P_2(\cos\Omega(\tau_2+\tau_1))P_2(\cos\Omega(\tau_1))\right\rangle
\end{aligned}
\tag{206}
$$

(cf. eq 205). The other two correlation functions, $C^{\{2,0\}}(\tau_2, \tau_1)$ and $C^{\{0,2\}}(\tau_2, \tau_1)$, measure correlations between electronic and orientational relaxation and are not relevant here. In one limit, the rotational-rate dispersion is solely due to heterogeneity. In this case,

$$
r^{(2)}(\tau_2,\tau_1) = r^{(1)}(\tau_2+\tau_1)\,. \tag{207}
$$

In the other limit, dispersion is purely due to homogeneous mechanisms, and

$$
r^{(2)}(\tau_2,\tau_1) = r^{(1)}(\tau_2)r^{(1)}(\tau_1)\,. \tag{208}
$$

Combinations of homogeneous and heterogeneous mechanisms produce intermediate results.

Using the methods of Refs. [16, 17], we find that the 2D anisotropy can be measured by combining MUPPETS signals from two polarization configurations:[143]

$$
r^{(2)}(\tau_2,\tau_1) = \frac{A^{(2)}(\tau_2,\tau_1;\theta_m,\theta_m) - A^{(2)}(\tau_2,\tau_1;-\theta_m,\theta_m)}{5A^{(2)}(\tau_2,\tau_1;\theta_m,\theta_m) + 7A^{(2)}(\tau_2,\tau_1;-\theta_m,\theta_m)} \tag{209}
$$

(cf. eq 204). All polarizations are linear, and the pulses within each simultaneous pair have the same polarization. The MUPPETS signal is an absorbance change $A^{(2)}(\tau_2, \tau_1; \theta_{32}, \theta_{21})$, with θ_{21} being the angle between pairs 2 and 1, and θ_{32} being the angle between pairs 3 and 2 (see Figure 2). The magic angle, θ_m = 54.7°, is the one familiar from 1D measurements.

With the configurations in eq 209, the polarization-control optics can be placed before the phase sensitive region of the set-up, that is, before grating G2 (Figure 2). Both quarter- and half-wave plates were used to correct for ellipticity introduced by corner cubes in the delay lines. The resulting pulses had extinction ratios of >1000:1 after the sample. The sample consisted of PM597 (Exciton) dissolved in methyl-terminated PDMS (Gelest) with an average molecular weight of 5970 g/mol (η = 100 cP, n = 76 monomers) at 25 °C. Light pulses were at the first absorption peak (527 nm) and had a duration of less than 300 fs, which is too short to affect our data. Although the MUPPETS experiment is heterodyned, and its signal has a phase. In this system, the phase is constant with delay time (SI). Only the magnitude is reported.

Results for the two polarization configurations needed to calculate the 2D anisotropy are shown in Figure 3a for several values of τ_1. The anisotropy is seen as the difference between these configurations at early times, which disappears as τ_2 exceeds the rotation time (400 ps). The size of the initial anisotropy also decreases as τ_1 exceeds the rotation time, as expected. The isotropic decay $C^{\{0,0\}}(\tau_2, \tau_1)$ derived from the sum of the two configurations is consistent with an uncomplicated decay of the excited-state population (SI).

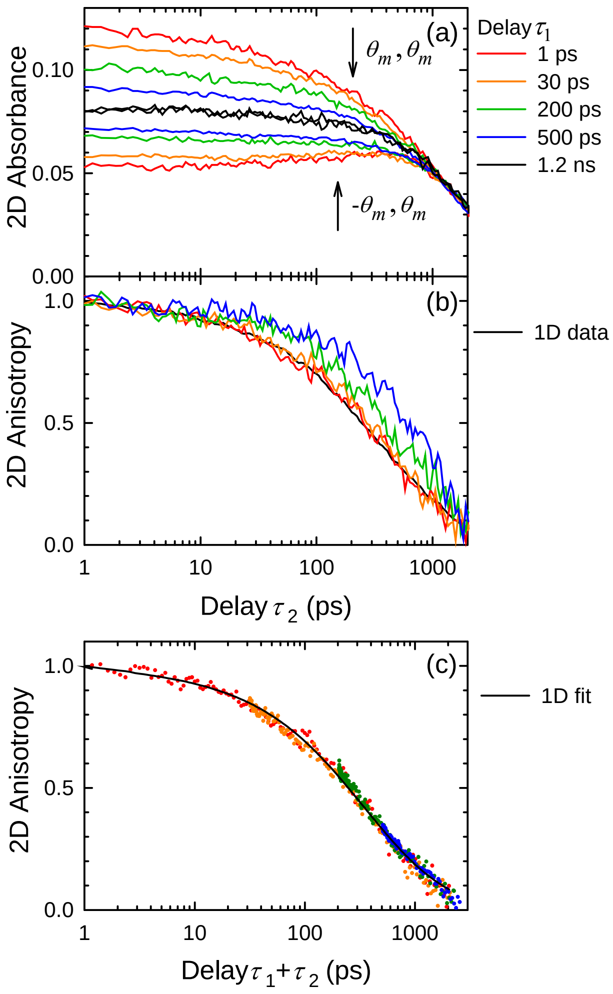

Figure 6.3. Polarized MUPPETS results in PDMS ($n = 76$). (a) The 2D absorbance at two polarizations, $A^{(2)}(\tau_2, \tau_1; \theta_m, \theta_m)$ (upper) and $A^{(2)}(\tau_2, \tau_1; -\theta_m, \theta_m)$ (lower), for several values of τ_1. (b) The 2D anisotropy $r^{(2)}(\tau_2, \tau_1)$ calculated from the data in (a) is represented by several cuts through the full 2D surface. For comparison, the 1D anisotropy $r^{(1)}(\tau_2)$ from Figure 1(a) is shown in black. (c) 2D anisotropies for various values of τ_1 plotted against $\tau_1 + \tau_2$ fall on a common curve and that curve matches the 1D anisotropy (MEM fit from Figure 4, black).

The 2D anisotropy $r^{(2)}(\tau_2, \tau_1)$ is calculated using eq 209. The full 2D surface is most easily understood by comparing selected cuts, as shown in Figure 3b. For short τ_1, the 2D anisotropy is the same as the 1D anisotropy, as it should be. The maximum observed anisotropy, $r^{(2)}(1\text{ ps}, 1\text{ ps}) = 0.07$ is below the theoretical value of 0.11. Part of the deficit may be due to the finite angle between the beams (4.6°), which is not included in the theory.

If there were no rotational heterogeneity, eq 208 would hold. After normalizing their amplitudes, the cross-sections in τ_2 would have shapes independent of τ_1. Figure 3b shows that this prediction is not true, so heterogeneity does exist. In the presence of heterogeneity, fast decaying subensembles are removed from the measurement as τ_1 increases, and the average decay of the remaining subensembles becomes slower and less disperse. The data in Figure 3b show this behavior. Thus, heterogeneity in the local rotational friction is a significant contribution to the observed dispersion.

This analysis by itself does not prove that homogeneous dispersion is absent; a combination of homogeneous and heterogeneous mechanisms may be operating. Figure 3c provides one test of this question. The cross-sections from Figure 3b are replotted versus $\tau_1 + \tau_2$. The data from different values of τ_1 fall onto a common curve. This result holds only if the decay of each subensemble is exponential (eq 207), that is, if there is no homogeneous contribution to the dispersion.

Equation 207 also holds that the common curve should be the same as the 1D decay. To represent the 1D data (Figure 1a), a standard maximum-entropy method (MEM) fit to the 1D data is shown in Figure 3c. (The MEM produces a smooth fit without assuming a specific functional form.[144, 145]) The fit is good. Through eq 207, this curve is a complete fit to both the 1D and 2D data, under the assumption that there is no homogeneous contribution to the dispersion.

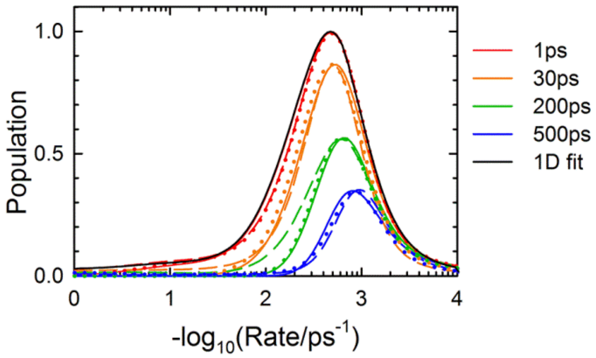

Figure 6.4. 2D anisotropy results expressed as rate spectra. Solid, black: Rate spectrum of the 1D anisotropy. Solid, colored: Spectra predicted from the 1D data, assuming no homogeneous dispersion. Dashed: Spectra from MUPPETS data, biased to minimize homogeneous dispersion. Dotted: Spectra from MUPPETS data, biased to maximize homogeneous dispersion.

A useful perspective is gained by examining the rate spectra of these results. In the case of heterogeneous dispersion, these spectra give the relative populations of the subensembles versus the log of their rate constants.[11] The rate spectrum of the 1D anisotropy decay has been calculated by the maximum-entropy method (MEM) and is shown in Figure 4 as the black curve. (The same fit shown in the time domain in Fig. 3c.) For ease of comparison to the time plots, the inverse rate (time constant) is used. The resulting distribution of rates is not only broad at the half-maximum, it also has a long tail extending toward fast rates and short time constants. One should be cautious about over interpreting the details of shape in rate spectra, but this asymmetry appears to be real.

The effect of the MUPPETS experiment is illustrated by the solid curves in Figure 4. The MUPPETS rate spectra (transforming along τ_2 for each value of τ_1) are predicted from the 1D rate spectrum under the assumption of only heterogeneous dispersion.[146] These predictions are shown as colored, solid curves in Figure 4a. The fast subensembles is preferentially suppressed as τ_1 increases, causing the left-hand side of the spectra to be progressively removed. If there were only homogeneous dispersion, its amplitude would drop, but the shape and position of the spectrum would be unchanged.

The rate spectra of the data need to be calculated and compared to these predictions. However, extracting a rate spectrum from data does not give a unique answer. A diverse family of spectra all fit the data within its noise. In the MEM, the fit is selected that also comes closest to a "prior" spectrum.[144, 145] The standard MEM uses a flat prior to find the spectrum that both fits the data and also is as broad and smooth as possible. We alter the MEM to find spectra that both fit the data and are biased toward either maximum or minimum amounts of heterogeneity. In the first case, the spectra predicted by assuming only heterogeneous dispersion are used as the prior (dotted curves in Figure 4). In the second case, spectra predicted assuming only homogeneous dispersion are used as the prior (dashed curves in Figure 4). In both cases, the fit has been refined to similar values of χ-squared.

To summarize, the black curve in Figure 3c and the solid curves in Figure 4 are one model that fits the data acceptably well, whereas the dashed and dotted spectra in Figure 4 define the range of models that can fit the data. This error range is small. It is also much closer to the heterogeneous-only model (Figure 4, colored solid curves) than to the homogeneous-only model (Figure 4, unchanging black curve). The data cannot show that the homogeneous dispersion is zero, but it does show that it is small compared to the total dispersion.

The development of local rate heterogeneity upon approaching the glass transition has been widely predicted by computer simulations of small-molecule liquids.[141] Experiments to verify these predictions have often been conducted on polymers within a few degrees of their glass transition temperatures T_g, where solute rotation times are on the millisecond or seconds timescales.[122, 130, 134, 140] In contrast, our polymer sample is 155 K above its glass-transition temperature,[147] i.e., $2.1T_g$, and has a rotational time of only 400 ps. It appears that the heterogeneity in this polymer is more closely related to its conformational flexibility than to its glass transition. Clarifying the relationship between these two mechanisms for local rate heterogeneity in polymers is an important direction for future research.

CHAPTER 7 ONE-DIMENSIONAL ANISOTROPY MEASUREMENTS IN IONIC LIQUIDS WITH DIFFERENT ALKYL CHAIN AND MOLAR FRACTION

7.1 INTRODUCTION

Dynamics in ionic liquids have attracted intense attention for several reasons: (1) They dissolve a wide range of polar or nonpolar molecules, making them great solvents for organic and inorganic reactions; (2) Even though ionic liquids are liquids, they have negligible vapor pressure; (3) they have high ionic conductivity. The best studied ionic liquids consist of imidazolium cations and anions such as PF_6^- or BF_4^-.

In addition to the large amount of work focused on the physical properties and solvent characteristics of ionic liquids, one particular interest is the microscopic heterogeneity of these liquids. Ionic liquids may not be a uniform system, but consist of micro-structured regions that are called local heterogeneity. Maroncelli and coworkers have measured the rotational correlation function of several dyes in $[BMIM^+][PF_6^-]$ and found a stretched exponential decay for all the probes.[148] This non-exponential decay form should be characteristic of supercooled liquids or polymers, not conventional simple solvents. Other evidence comes from the research done by Samanta and coworkers, in which they observed excitation-wavelength-dependent shift of fluorescence spectra.[149, 150] Lopes and Padua did MD simulations on two common ionic liquids and observed the nanostructure of separated polar and nonpolar regions in those liquids.[12] Their work demonstrated the possible existence of heterogeneity theoretically. The polar region has the structure of a tridimensional network of ionic channels, whereas the nonpolar domain is either dispersed or continuous depending on the alkyl side chain. Kim and coworkers calculated the rotational correlation functions for a diatomic solute in $[EMI^+][PF_6^-]$ and found that the rotational decay can be well fitted by a stretched exponential function.[151] They attributed this nonexponential behavior to the heterogeneous dynamics in $[EMI^+][PF_6^-]$.

In this chapter, we measured the rotational decay of pyrromethene 597 (PM597) in a series of ionic liquids, 1-alkyl-3-methylimidazolium tetrafluoroborate $[C_nMIM^+][BF_4^-]$ mixed with acetonitrile. We conducted two sets of experiments. In one of them, we fixed the volume fraction between ionic liquids and acetonitrile but varied the alkyl chain length in ionic liquids. In another set, we used only one type of ionic liquid but changed the volume fraction of ionic liquid. Nonexponential rotational decays were observed for all samples from alkyl chain of ethyl (C_2) to dodecyl (C_{12}). This result shows a clear deviation from the Stokes-Einstein-Debye model.

7.2 EXPERIMENTAL DETAILS

All of our ionic liquids were purchased from IoLiTec at 98+% grade and kept in a desiccator before using. Pyrromethene 597 (PM597) dye was ordered from Exciton and used directly without further processing. The ionic liquids were mixed with the required amount of acetonitrile, and then PM597 was dissolved into the mixed solvent to get an optical density of 0.4 in a 1 mm silica cuvette. Although no evidence of photoproducts was observed during our experiments, a flow system was used to ensure against any accumulation of them.

The experiments were conducted with a two beam pump–probe polarized setup. A 1000 Hz, 527 nm, 300 fs pump pulse excited the sample. After a time delay, a probe pulse *a* passed through the sample, and the intensity of *a* was detected by a photodiode. A reference pulse *b,* which has the same origin as pulse *a*, but does not pass through the sample, was measured by another detector. The difference between two detectors was then measured to cancel the fluctuations in probe intensity. The noise from fluctuations in the pump intensity was reduced by directing a sample of the pump pulse to a home-made, 300 ms time-constant photodiode. The signal from this photodiode went into the auxiliary channel of the lock-in amplifier. The raw intensity from the difference of the a and b detectors is normalized by the square of this auxiliary intensity to get the final signal. For each sample, pump–probe data were measured in both parallel and perpendicular polarizations. In polarization experiments, the rotational dynamics are measured by the anisotropy decay. According to the Eq. (204) in chapter 6, the 1D anisotropy decay $r^{(1)}(\tau_1)$ is calculated from two absorbances, measured by setting the polarization of pump and probe to be either parallel or perpendicular to each other.

7.3 RESULTS AND DISCUSSION

In the first series of measurements, solvent mixtures were used to keep the entire decay within our experimental time range. We fixed the molar fraction of ionic liquids $[C_n\mathrm{MIM}^+][\mathrm{BF}_4^-]$ at $x_{IL} = 0.2$ and varied the alkyl chain length *n*. Figure 7.1 shows the individual absorbance at 0° and 90° polarizations for PM597 in all ionic liquids. The curves were manually adjusted to match with each other at long time.

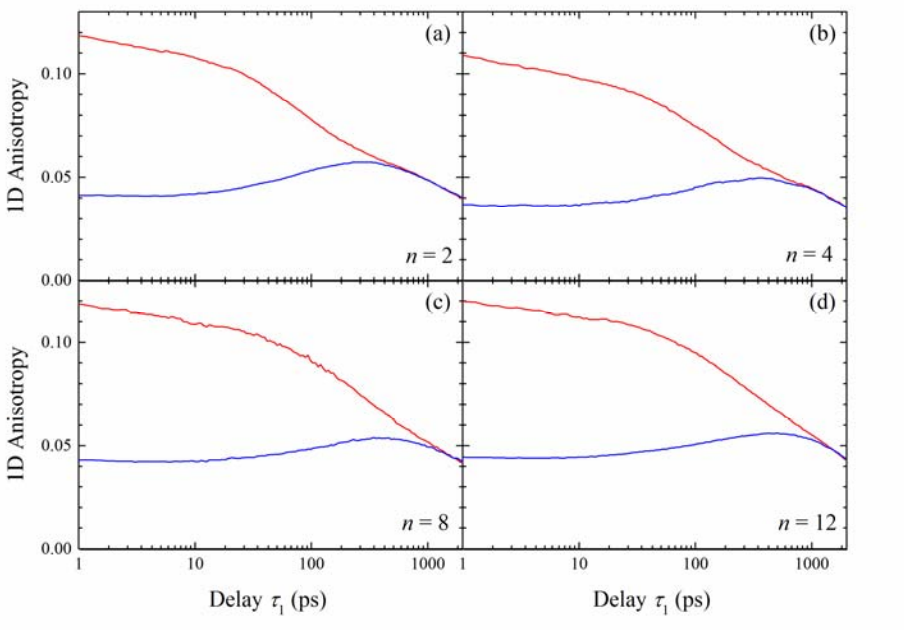

Figure 7.1. 1D polarization experiments of PM597 in different ionic liquids $[C_nMIM^+][BF_4^-]$ mixed with acetonitrile. (a) $n = 2$, (b) $n = 4$, (c) $n = 8$, (d) $n = 12$

Figure 7.2 (a) shows the results of anisotropy decay for all ionic liquids. As shown in the figure, the rotational time increases with increasing alkyl-chain length from ethyl (C_2) to dodecyl (C_{12}). This result is consistent with the increase of viscosity as the alky chain increases.[152]

Besides, the rotational decay is sometimes nonexponential, and all were fitted by stretched exponential functions in the form of $S(t) = \exp[-(t/T)^{\beta}]$. Fitting parameters are tabulated in Table 7.1. Nonexponential decay might be caused by the heterogeneous microstructure that mentioned in other studies.[139, 153] The anisotropy decay of pure acetonitrile, which can be well fitted into a single exponential decay function, is shown in the figure (orange) for reference. The time axis of each plot is then transferred to a normalized scale in Figure 7.2 (b). The timescale for each solvent has been divided by the rotational time constant, from the fitting. Slight, but distinguishable, differences in the shape of the decay can be observed.

Table 7.1. Fit parameters and physical properties of solvents: molecular weight *M*, length of alkyl chain *n*, molar fraction of ionic liquid *x*, and stretched-exponential fit parameters *T* and *β*.

	M (g/mol)	*n*	*x*	*T* (ps)	*β*
CH_3CN	41	-		33.4	1
$EMIM^+ BF_4^-/ CH_3CN$	198	2	0.2	93.6	0.91
$BMIM^+ BF_4^-/ CH_3CN$	226	4	0.2	132.2	0.86
$C_8MIM^+ BF_4^-/ CH_3CN$	282	8	0.2	230	0.82
$C_{12}MIM^+ BF_4^-/ CH_3CN$	338	12	0.2	252.8	0.79

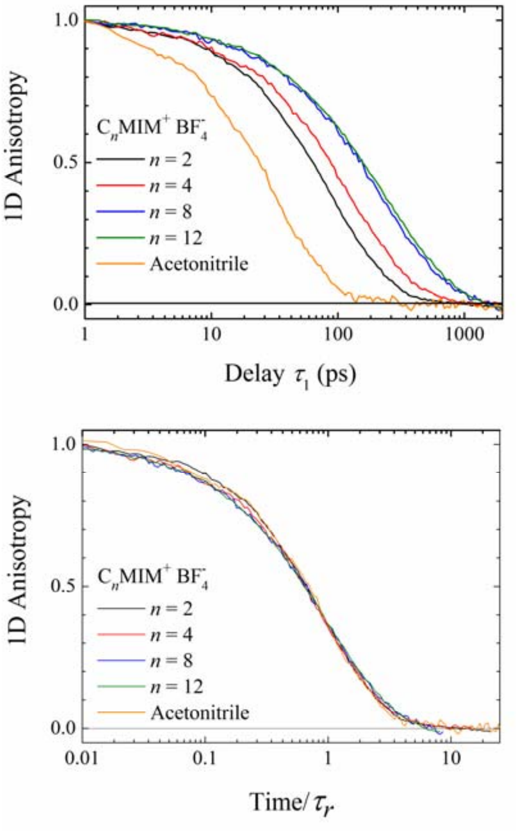

Figure 7.2. 1D polarization experiments of PM597 in different ionic liquids mixed with acetonitrile. (a) Anisotropy decay results in ionic liquids with different alkyl chain length (x_{IL} = 0.2) and in pure acetonitrile (orange). (b) Anisotropy decays plotted versus normalized time scale (Time/τ_r).

On the other hand, if we fix the chain length at 12 and change the ratio between the ionic liquids and acetonitrile, the results are shown in figure 7.3. The ionic liquid we used is $[C_{12}MIM^+][BF_4^-]$. With the increase of ionic-liquid molar fraction, the decay becomes slower. However, the stretched-exponential parameter β changes little, alwasy around 0.83. Bring them to a normalized time scale make three curves overlap [Fig. 7.4 (b)].

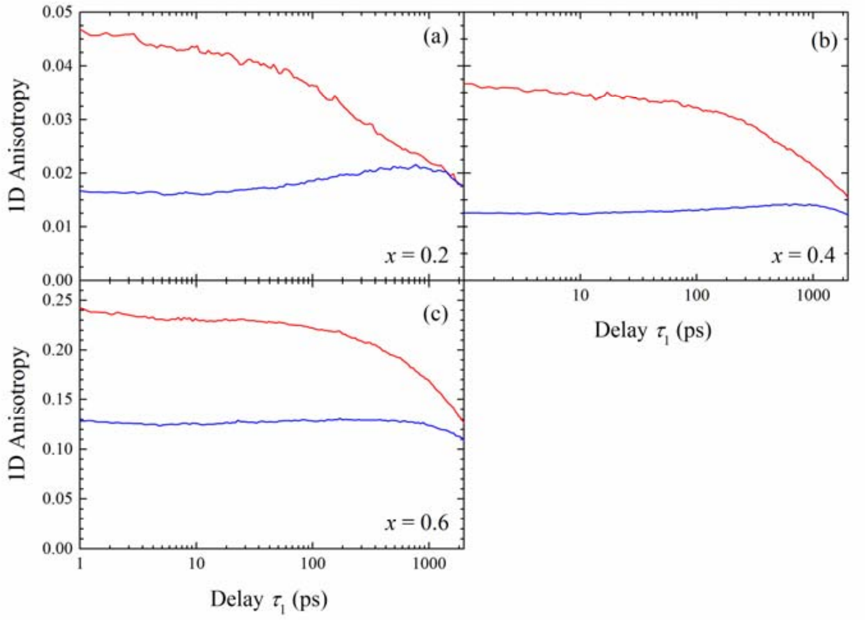

Figure 7.3. 1D polarization experiments of PM597 in $[C_nMIM^+][BF_4^-]$ at different molar fraction. (a) $x = 0.2$, (b) $x = 0.4$, (c) $x = 0.6$

Overall, the rotational decays have a detectable nonexponentiality, but it is much smaller than is seen in solvation expeirments.[131, 148, 154, 155] Our group is currently studying the origin of nonexponential decay in ionic-liquid solvation. These studies of rotation provide a useful contrast to those studies.

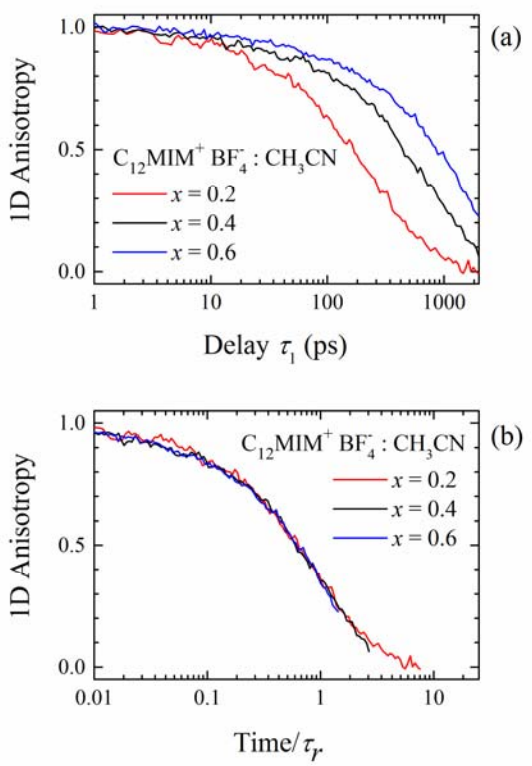

Figure 7.4. 1D polarization experiments of PM597 in $[C_{12}MIM^+][BF_4^-]$ mixed with acetonitrile. (a) Anisotropy decay results at different $[C_{12}MIM^+][BF_4^-]$ molar fraction. (b) Anisotropy decays plotted versus normalized time scale (Time/τ_r).

Table 7.2. Fit parameters and physical properties of solvents: ionic liquid molar fraction *x*, stretched-exponential fit parameters *T* and *β*.

	x	*T (ps)*	*β*
$C_{12}MIM^+ BF_4^- /CH_3CN$	0.2	263	0.81
$C_{12}MIM^+ BF_4^-/ CH_3CN$	0.4	871	0.83
$C_{12}MIM^+ BF_4^-/ CH_3CN$	0.6	1375	0.81

REFERENCES

(1) Coe, S.; Woo, W.-K.; Bawendi, M.; Bulović, V. *Nature* **2002**, *420*, 800.
(2) Colvin, V.; Schlamp, M.; Alivisatos, A. *Nature* **1994**, *370*, 354.
(3) Mueller, A. H.; Petruska, M. A.; Achermann, M.; Werder, D. J.; Akhadov, E. A.; Koleske, D. D.; Hoffbauer, M. A.; Klimov, V. I. *Nano Lett.* **2005**, *5*, 1039.
(4) Stouwdam, J. W.; Janssen, R. A. *J. Mater. Chem.* **2008**, *18*, 1889.
(5) Medintz, I. L.; Clapp, A. R.; Mattoussi, H.; Goldman, E. R.; Fisher, B.; Mauro, J. M. *Nature materials* **2003**, *2*, 630.
(6) Medintz, I. L.; Uyeda, H. T.; Goldman, E. R.; Mattoussi, H. *Nature materials* **2005**, *4*, 435.
(7) Huffaker, D.; Park, G.; Zou, Z.; Shchekin, O.; Deppe, D. *Applied physics letters* **1998**, *73*, 2564.
(8) Malko, A.; Mikhailovsky, A.; Petruska, M.; Hollingsworth, J.; Htoon, H.; Bawendi, M.; Klimov, V. *Applied physics letters* **2002**, *81*, 1303.
(9) Achermann, M.; Bartko, A. P.; Hollingsworth, J. A.; Klimov, V. I. *Nat. Phys.* **2006**, *2*, 557.
(10) Roussignol, P.; Kull, M.; Ricard, D.; De Rougemont, F.; Frey, R.; Flytzanis, C. *Appl. Phys. Lett.* **1987**, *51*, 1882.
(11) Khurmi, C.; Berg, M. A. *J. Chem. Phys.* **2008**, *129*, 064504.
(12) Canongia Lopes, J. N. A.; Padua, A. A. H. *J. Phys. Chem. B* **2006**, *110*, 3330.
(13) van Veldhoven, E.; Khurmi, C.; Zhang, X.; Berg, M. A. *ChemPhysChem* **2007**, *8*, 1761.
(14) Khurmi, C.; Berg, M. A. *J. Phys. Chem. A* **2008**, *112*, 3364.
(15) Khurmi, C.; Berg, M. A. *J. Opt. Soc. Am. B* **2009**, *26*, 2357.
(16) Berg, M. A. *J. Chem. Phys.* **2010**, *132*, 144105.
(17) Berg, M. A. *J. Chem. Phys.* **2010**, *132*, 144106.
(18) Sahu, K.; Berg, M. A. *J. Chem. Phys.* **2011**, *134*, 144502.
(19) Sahu, K.; Kern, S. J.; Berg, M. A. *J. Phys. Chem. A* **2011**, *115*, 7984.
(20) Kern, S. J.; Sahu, K.; Berg, M. A. *Nano Lett.* **2011**, *11*, 3493.
(21) Berg, M. A. *Advances in Chemical Physics* **2012**, *150*, 1.
(22) Sahu, K.; Wu, H.; Berg, M. A. *J. Am. Chem. Soc.* **2013**, *135*, 1002.
(23) Sahu, K.; Wu, H.; Berg, M. A. *J. Phys. Chem. B* **2013**, *117*, 15257.
(24) von Jena, A.; Lessing, H. E. *Optical and Quantum Electronics* **1979**, *11*, 419.
(25) Fayer, M. D. *Annu. Rev. Phys. Chem.* **1982**, *33*, 63.
(26) Eichler, H. J. *Laser-Induced Dynamic Gratings*; Springer: Berlin, 1986.
(27) Hahn, E. L. *Phys. Rev.* **1950**, *80*, 580.
(28) Kurnit, N. A.; Abella, I. D.; Hartmann, S. R. *Phys. Rev. Lett.* **1964**, *13*, 567.
(29) Ernst, R. R.; Bodenhausen, G.; Wokaun, A. *Principles of Nuclear Magnetic Resonance in One and Two Dimensions*; Clarendon Press: Oxford, 1987; Vol. 14.

(30) Bax, A. *Two-Dimensional Nuclear Magnetic Resonance in Liquids*; Delft University Press: Delft, Holland, 1982.

(31) Jonas, D. M. *Annu. Rev. Phys. Chem.* **2003**, *54*, 425.

(32) Zheng, J.; Kwak, K.; Fayer, M. D. *Acc. Chem. Res.* **2007**, *40*, 75.

(33) Remorino, A.; Hochstrasser, R. M. *Acc. Chem. Res.* **2012**, *45*, 1896.

(34) Brixner, T.; Stenger, J.; Vaswani, H. M.; Cho, M.; Blankenship, R. E.; Fleming, G. R. *Nature* **2005**, *434*, 625.

(35) Ginsberg, N. S.; Cheng, Y.-C.; Fleming, G. R. *Acc. Chem. Res.* **2009**, *42*, 1352.

(36) Kim, J.; Mukamel, S.; Scholes, G. D. *Acc. Chem. Res.* **2009**, *42*, 1375.

(37) Turner, D. B.; Wen, P.; Arias, D. H.; Nelson, K. A. *Phys. Rev. B* **2011**, *84*, 165321.

(38) Wang, L.; Middleton, C. T.; Singh, S.; Reddy, A. S.; Woys, A. M.; Strasfeld, D. B.; Marek, P.; Raleigh, D. P.; de Pablo, J. J.; Zanni, M. T.; Skinner, J. L. *J. Am. Chem. Soc.* **2011**, *133*, 16062.

(39) Lott, G. A.; Perdomo-Ortiz, A.; Utterback, J. K.; Widom, J. R.; Aspuru-Guzik, A.; Marcus, A. H. *Proceedings of the National Academy of Sciences* **2011**, *108*, 16521.

(40) Caram, J. R.; Lewis, N. H. C.; Fidler, A. F.; Engel, G. S. *J. Chem. Phys.* **2012**, *136*, 104505.

(41) Mukamel, S. *Principles of Nonlinear Optical Spectroscopy*; Oxford University Press: New York, 1995; Vol. 6.

(42) Lebedev, L. P.; Cloud, M. J. *Tensor Analysis*; World Scientific Publishing: Singapore, 2003.

(43) Klimov, V. I. *Annu. Rev. Phys. Chem.* **2007**, *58*, 635.

(44) McGuire, J. A.; Joo, J.; Pietryga, J. M.; Schaller, R. D.; Klimov, V. I. *Acc. Chem. Res.* **2008**, *41*, 1810.

(45) Genberg, L.; Bao, Q.; Gracewski, S.; Miller, R. J. D. *Chem. Phys.* **1989**, *131*, 81.

(46) Yan, Y.-X.; Nelson, K. A. *J. Chem. Phys.* **1987**, *87*, 6240.

(47) Duggal, A. R.; Nelson, K. A. *J. Chem. Phys.* **1991**, *94*, 7677.

(48) Kimura, Y.; Fukuda, M.; Kajimoto, O.; Terazima, M. *J. Chem. Phys.* **2006**, *125*, 194516.

(49) Klimov, V. I.; Mikhailovsky, A. A.; Xu, S.; Malko, A.; Hollingsworth, J. A.; Leatherdale, C. A.; Eisler, H.-J.; Bawendi, M. G. *Science* **2000**, *290*, 314.

(50) Peterson, J. J.; Nesbitt, D. J. *Nano Lett.* **2009**, *9*, 338.

(51) Nair, G.; Chang, L.-Y.; Geyer, S. M.; Bawendi, M. G. *Nano Lett.* **2011**, *11*, 2145.

(52) Klimov, V. I.; Mikhailovsky, A. A.; McBranch, D. W.; Leatherdale, C. A.; Bawendi, M. G. *Science* **2000**, *287*, 1011.

(53) Caruge, J. M.; Chan, Y.; Sundar, V.; Eisler, H. J.; Bawendi, M. G. *Phys. Rev. B* **2004**, *70*, 085316.

(54) Klimov, V. I.; McGuire, J. A.; Schaller, R. D.; Rupasov, V. I. *Phys. Rev. B* **2008**, *77*, 195324.

(55) Nair, G.; Bawendi, M. G. *Phys. Rev. B* **2007**, *76*, 081304.

(56) Rosen, S.; Schwartz, O.; Oron, D. *Phys. Rev. Lett.* **2010**, *104*, 157404.

(57) Zhao, J.; Nair, G.; Fisher, B. R.; Bawendi, M. G. *Phys. Rev. Lett.* **2010**, *104*, 157403.

(58) Cordones, A. A.; Bixby, T. J.; Leone, S. R. *Nano Lett.* **2011**, *11*, 3366.

(59) García-Santamaría, F.; Brovelli, S.; Viswanatha, R.; Hollingsworth, J. A.; Htoon, H.; Crooker, S. A.; Klimov, V. I. *Nano Lett.* **2011**, *11*, 687.
(60) Nair, G.; Zhao, J.; Bawendi, M. G. *Nano Lett.* **2011**, *11*, 1136.
(61) Park, Y. S.; Malko, A. V.; Vela, J.; Chen, Y.; Ghosh, Y.; Garcia-Santamaria, F.; Hollingsworth, J. A.; Klimov, V. I.; Htoon, H. *Phys. Rev. Lett.* **2011**, *106*, 187401.
(62) McGuire, J. A.; Sykora, M.; Joo, J.; Pietryga, J. M.; Klimov, V. I. *Nano Lett.* **2010**, *10*, 2049.
(63) Cichos, F.; von Borczyskowski, C.; Orrit, M. *Current Opinion in Colloid & Interface Science* **2007**, *12*, 272.
(64) Tyagi, P.; Kambhampati, P. *J. Chem. Phys.* **2011**, *134*, 094706.
(65) Osborne, M. A.; Lee, S. F. *ACS Nano* **2011**, *5*, 8295.
(66) Wu, H.; Berg, M. A. *J. Chem. Phys.* **2013**, *138*, 034201.
(67) Huxter, V. M.; Scholes, G. D. *J. Chem. Phys.* **2006**, *125*, 144716.
(68) Kim, J.; Wong, C. Y.; Scholes, G. D. *Acc. Chem. Res.* **2009**, *42*, 1037.
(69) Wang, L.-W.; Califano, M.; Zunger, A.; Franceschetti, A. *Phys. Rev. Lett.* **2003**, *91*, 056404.
(70) Norris, D. J.; Bawendi, M. G. *Phys. Rev. B* **1996**, *53*, 16338.
(71) Malko, A. V.; Mikhailovsky, A. A.; Petruska, M. A.; Hollingsworth, J. A.; Klimov, V. I. *J. Phys. Chem. B* **2004**, *108*, 5250.
(72) Schwartz, O.; Oron, D. *Isr. J. Chem.* **2012**, *52*, 992.
(73) Chung, I.; Bawendi, M. G. *Phys. Rev. B* **2004**, *70*, 165304.
(74) Lee, S. F.; Osborne, M. A. *ChemPhysChem* **2009**, *10*, 2174.
(75) Achermann, M.; Hollingsworth, J. A.; Klimov, V. I. *Phys. Rev. B* **2003**, *68*, 245302.
(76) Bonati, C.; Mohamed, M. B.; Tonti, D.; Zgrablic, G.; Haacke, S.; van Mourik, F.; Chergui, M. *Phys. Rev. B* **2005**, *71*, 205317.
(77) Robel, I.; Gresback, R.; Kortshagen, U.; Schaller, R. D.; Klimov, V. I. *Phys. Rev. Lett.* **2009**, *102*, 177404.
(78) Kambhampati, P. *Acc. Chem. Res.* **2011**, *44*, 1.
(79) Insert citation to companion paper.
(80) Nelson, K. A.; Casalegno, R.; Miller, R. J. D.; Fayer, M. D. *J. Chem. Phys.* **1982**, *77*, 1144.
(81) Fayer, M. D., *Ultrafast Infrared and Raman Spectroscopy*. Marcel Dekker: New York, NY, 2001.
(82) Hamm, P.; Zanni, M. *Concepts and Methods of 2D Infrared Spectroscopy*; Cambridge University Press: Cambridge, 2011.
(83) Stone, K. W.; Gundogdu, K.; Turner, D. B.; Li, X.; Cundiff, S. T.; Nelson, K. A. *Science* **2009**, *324*, 1169.
(84) Cundiff, S. T. *J. Opt. Soc. Am. B* **2012**, *29*, A69.
(85) Moody, G.; Singh, R.; Li, H.; Akimov, I. A.; Bayer, M.; Reuter, D.; Wieck, A. D.; Cundiff, S. T. *Phys. Rev. B* **2013**, *87*, 045313.
(86) Wong, C. Y.; Scholes, G. D. *J. Phys. Chem. A* **2010**, *115*, 3797.
(87) Turner, D. B.; Hassan, Y.; Scholes, G. D. *Nano Lett.* **2011**, *12*, 880.
(88) Velizhanin, K. A.; Piryatinski, A. *J. Phys. Chem. B* **2011**, *115*, 5372.
(89) Block, S. B.; Yurs, L. A.; Pakoulev, A. V.; Selinsky, R. S.; Jin, S.; Wright, J. C. *J. Phys. Chem. Lett.* **2012**, *3*, 2707.

(90) Harel, E.; Rupich, S. M.; Schaller, R. D.; Talapin, D. V.; Engel, G. S. *Phys. Rev. B* **2012**, *86*, 075412.

(91) Griffin, G. B.; Ithurria, S.; Dolzhnikov, D. S.; Linkin, A.; Talapin, D. V.; Engel, G. S. *J. Chem. Phys.* **2013**, *138*, 014705.

(92) Fingerhut, B. P.; Richter, M.; Luo, J.-W.; Zunger, A.; Mukamel, S. *Annalen der Physik* **2013**, *525*, 31.

(93) de Mello Donegá, C.; Koole, R. *J. Phys. Chem. C* **2009**, *113*, 6511.

(94) Klimov, V. I.; McBranch, D. W.; Leatherdale, C. A.; Bawendi, M. G. *Phys. Rev. B* **1999**, *60*, 13740.

(95) Burda, C.; Link, S.; Mohamed, M.; El-Sayed, M. *J. Phys. Chem. B* **2001**, *105*, 12286.

(96) Hines, M. A.; Guyot-Sionnest, P. *J. Phys. Chem.* **1996**, *100*, 468.

(97) Dabbousi, B. O.; Rodriguez-Viejo, J.; Mikulec, F. V.; Heine, J. R.; Mattoussi, H.; Ober, R.; Jensen, K. F.; Bawendi, M. G. *J. Phys. Chem. B* **1997**, *101*, 9463.

(98) Kimura, Y.; Yamamoto, Y.; Terazima, M. *J. Chem. Phys.* **2005**, *123*, 054513.

(99) Foggi, P.; Neuwahl, F. V. R.; Moroni, L.; Salvi, P. R. *J. Phys. Chem. A* **2003**, *107*, 1689.

(100) Schaller, R. D.; Petruska, M. A.; Klimov, V. I. *Appl. Phys. Lett.* **2005**, *87*, 253102.

(101) Schaller, R. D.; Sykora, M.; Jeong, S.; Klimov, V. I. *J. Phys. Chem. B* **2006**, *110*, 25332.

(102) Sewall, S. L.; Cooney, R. R.; Anderson, K. E. H.; Dias, E. A.; Sagar, D. M.; Kambhampati, P. *J. Chem. Phys.* **2008**, *129*, 084701.

(103) Knowles, K. E.; McArthur, E. A.; Weiss, E. A. *ACS Nano* **2011**, *5*, 2026.

(104) McArthur, E. A.; Morris-Cohen, A. J.; Knowles, K. E.; Weiss, E. A. *J. Phys. Chem. B* **2010**, *114*, 14514.

(105) Franceschetti, A.; Zhang, Y. *Phys. Rev. Lett.* **2008**, *100*, 136805.

(106) Klimov, V. I. *J. Phys. Chem. B* **2000**, *104*, 6112.

(107) Jiang, Z.-J.; Kelley, D. F. *Nano Lett.* **2011**, *11*, 4067.

(108) insert reference to companion paper

(109) Eichler, H.; Stahl, H. *J. Appl. Phys.* **1973**, *44*, 3429.

(110) Miller, R. J. D.; Casalegno, R.; Nelson, K. A.; Fayer, M. D. *Chem. Phys.* **1982**, *72*, 371.

(111) Nelson, K. A.; Miller, R. J. D.; Lutz, D. R.; Fayer, M. D. *J. Appl. Phys.* **1982**, *53*, 1144.

(112) Nelson, K. A.; Fayer, M. D. *J. Chem. Phys.* **1980**, *72*, 5202.

(113) Andrews, J. R.; Hochstrasser, R. M. *Chem. Phys. Lett.* **1980**, *76*, 207.

(114) Morais, J.; Ma, J.; Zimmt, M. B. *J. Phys. Chem.* **1991**, *95*, 3885.

(115) Terazima, M. *J. Phys. Chem. A* **1998**, *102*, 545.

(116) Yan, Y.-X.; Cheng, L.-T.; Nelson, K. A. *J. Chem. Phys.* **1988**, *88*, 6477.

(117) Sun, T.; Morais, J.; Diebold, G. J.; Zimmt, M. B. *J. Chem. Phys.* **1992**, *97*, 9324.

(118) Fukuda, M.; Kajimoto, O.; Terazima, M.; Kimura, Y. *J. Mol. Liq.* **2007**, *134*, 49.

(119) George, J.; Sastry, N. V. *J. Chem. Eng. Data* **2003**, *48*, 977.

(120) Fleming, G. R. *Chemical Applications of Ultrafast Spectroscopy*; Oxford University Press: Oxford, 1986.

(121) Williams, A. M.; Jiang, Y.; Ben-Amotz, D. *Chem. Phys.* **1994**, *180*, 119.

(122) Hyde, P. D.; Ediger, M. D. *J. Chem. Phys.* **1990**, *92*, 1036.
(123) Brocklehurst, B.; Young, R. N. *J. Phys. Chem. A* **1999**, *103*, 3818.
(124) Daniel, S. N.; Niemeyer, E. D.; Bright, F. V. *Macromolecules* **1999**, *32*, 8084.
(125) Jiang, Y.; Blanchard, G. J. *J. Phys. Chem.* **1995**, *99*, 7904.
(126) Goldie, S. N.; Blanchard, G. J. *J. Phys. Chem. A* **1999**, *103*, 999.
(127) Hay, C. E.; Marken, F.; Blanchard, G. J. *J. Phys. Chem. A* **2010**, *114*, 4957.
(128) Sluch, M. I.; Somoza, M. M.; Berg, M. A. *J. Phys. Chem. B* **2002**, *106*, 7385.
(129) Somoza, M. M.; Sluch, M. I.; Berg, M. A. *Macromolecules* **2003**, *36*, 2721.
(130) Wei, C.-Y. J.; Vanden Bout, D. A. *J. Phys. Chem. B* **2009**, *113*, 2253.
(131) Ito, N.; Arzhantsev, S.; Heitz, M.; Maroncelli, M. *J. Phys. Chem. B* **2004**, *108*, 5771.
(132) Wang, L.-M.; Richert, R. *J. Chem. Phys.* **2004**, *120*, 11082.
(133) Fourkas, J. T.; Trebino, R.; Fayer, M. D. *J. Chem. Phys.* **1992**, *97*, 69.
(134) Ediger, M. D. *Annu. Rev. Phys. Chem.* **2000**, *51*, 99.
(135) Yang, M.; Richert, R. *J. Chem. Phys.* **2001**, *115*, 2676.
(136) Jin, H.; Li, X.; Maroncelli, M. *J. Phys. Chem. B* **2007**, *111*, 13473.
(137) Santhosh, K.; Banerjee, S.; Rangaraj, N.; Samanta, A. *J. Phys. Chem. B* **2010**, *114*, 1967.
(138) Suda, K.; Terazima, M.; Kimura, Y. *Chem. Phys. Lett.* **2012**, *531*, 70.
(139) Fruchey, K.; Fayer, M. D. *J. Phys. Chem. B* **2010**, *114*, 2840.
(140) Kaufman, L. J. *Annu. Rev. Phys. Chem.* **2013**, *64*, 177.
(141) Berthier, L.; Biroli, G.; Bouchaud, J.-P.; Cipelletti, L.; van Saarloos, W., *Dynamical Heterogeneities in Glasses, Colloids and Granular Media*. Oxford University Press: Oxford, 2011; p 480.
(142) Quitevis, E. L.; Marcus, A. H.; Fayer, M. D. *J. Phys. Chem.* **1993**, *97*, 5762.
(143) H. Wu and M. A. Berg, to be submitted for publication.
(144) Steinbach, P. J. MemExp Web Site. http://cmm.cit.nih.gov/memexp/
(145) Steinbach, P. J. *J. Chem. Inf. Comput. Sci.* **2002**, *42*, 1476.
(146) Equation 64 of Ref. 18.
(147) Hintermeyer, J.; Herrmann, A.; Kahlau, R.; Goiceanu, C.; Rössler, E. A. *Macromolecules* **2008**, *41*, 9335.
(148) Ito, N.; Arzhantsev, S.; Maroncelli, M. *Chem. Phys. Lett.* **2004**, *396*, 83.
(149) Paul, A.; Mandal, P. K.; Samanta, A. *J. Phys. Chem. B* **2005**, *109*, 9148.
(150) Mandal, P. K.; Sarkar, M.; Samanta, A. *J. Phys. Chem. A* **2004**, *108*, 9048.
(151) Shim, Y.; Jeong, D.; Choi, M. Y.; Kim, H. J. *J. Chem. Phys.* **2006**, *125*, 061102.
(152) Tokuda, H.; Hayamizu, K.; Ishii, K.; Susan, M. A. B. H.; Watanabe, M. *J. Phys. Chem. B* **2005**, *109*, 6103.
(153) Das, S. K.; Sahu, P. K.; Sarkar, M. *J. Phys. Chem. B* **2013**, *117*, 636.
(154) Liang, M.; Zhang, X.-X.; Kaintz, A.; Ernsting, N. P.; Maroncelli, M. *J. Phys. Chem. B* **2014**, *118*, 1340.
(155) Zhang, X.-X.; Liang, M.; Ernsting, N. P.; Maroncelli, M. *J. Phys. Chem. B* **2012**, *117*, 4291.
(156) Steinbach, P. J.; Ionescu, R.; Matthews, C. R. *Biophys. J*. **2002**, *82*, 2244.
(157) Costela, A.; García-Moreno, I.; Pintado-Sierra, M.; Amat-Guerri, F.; Sastre, R.; Liras, M.; Arbeloa, F. L.; Prieto, J. B.; Arbeloa, I. L. *J. Phys. Chem. A* **2009**, *113*, 8118.

(158) Bañuelos Prieto, J.; López Arbeloa, F.; Martínez Martínez, V.; Arbeloa López, T.; López Arbeloa, I. *J. Phys. Chem. A* **2004**, *108*, 5503.

(159) Montejano, H. A.; Amat-Guerri, F.; Costela, A.; García-Moreno, I.; Liras, M.; Sastre, R. *J. Photochem. Photobiol., A* **2006**, *181*, 142.

APPENDIX A – SUGGESTING MECHANISMS FOR BIEXCITON DECAY

The biexciton decay $S(t)$ shown in Figure 2B of the main text can be fit with various forms, each suggesting a different mechanism. Several forms are shown in Figure S1. In each case, the amplitudes of the data and fit have been matched.

Biexponential. $S(t) = 0.635 \exp(-t/6 \text{ ps}) + 0.365 \exp(-t/40 \text{ ps})$. The fit to the data is shown in Figure 1B of the main paper.

Stretched Exponential. $S(t) = \exp[-(t/6.5 \text{ ps})^{0.48}]$. The fit to the data is shown in Figure S1A.

Gaussian Distribution of Barriers. The rate distribution on a log-lifetime scale (for example, Figure 3) is assumed to be a Gaussian. A Gaussian distribution of barrier heights in an Arrhenius process is an example of this model. The lifetime at the peak of the Gaussian is 7.7 ps and the standard deviation is 0.6. This standard deviation corresponds to a 26-fold variation in the rate distribution at its half-width. The fit to the data is shown in Figure S1B.

Maximum-Entropy Method. This method is a standard one for fitting a continuous distribution of lifetimes of arbitrary shape.[144, 145, 156] The distribution is shown in Figure 3. The fit to the data is shown in Figure S1C.

Time-Dependent Rate. The signal decays with a rate k that is time dependent: $k(t) = 0.025 \text{ ps}^{-1} + 0.07 \text{ ps}^{-1} \exp[-(t/40 \text{ ps})]$. The fit to the data is shown in Figure S1D.

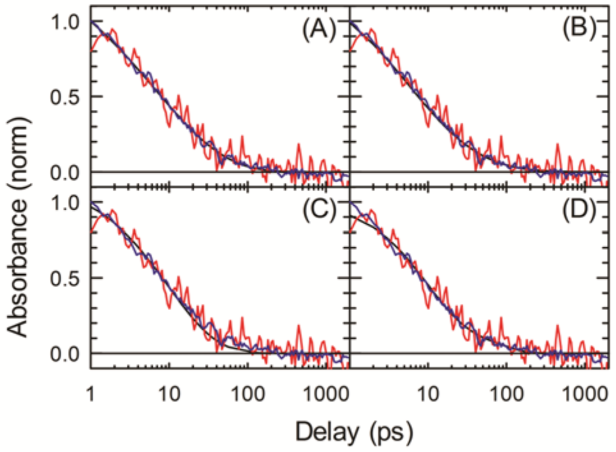

Figure A1. Other possible fits to the biexciton decay. The red and blue curves are MUPPETS and fluence-dependent data from Figure 2B, respectively. The black curves are the fits: (A) stretched exponential, (B) Gaussian distribution of rates, (C) maximum-entropy method, and (D) time-dependent rate. The fit to a biexponential is shown in Figure 1B.

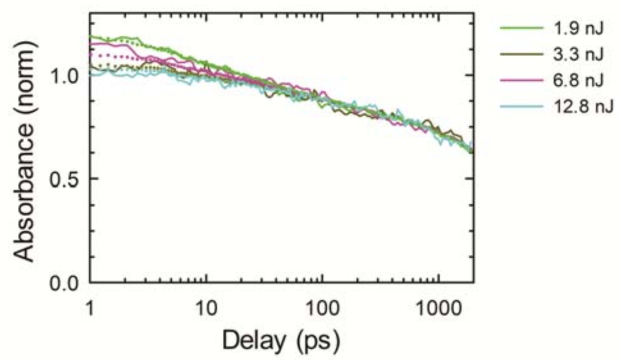

Figure A2. Additional data not shown in Figure 1A.

APPENDIX B – OFF-DIAGONAL TIME EVOLUTION

The calculation of the off-diagonal elements of the Green's function starts by dividing the time evolution between two times, t_1 and t_2, by M intermediate times t'_a:

$$\mathbf{G}(t_2, t_1) = \mathbf{G}(t_2, t'_M) \ldots \mathbf{G}(t'_{a+1}, t'_a) \ldots \mathbf{G}(t'_1, t_1) \, . \tag{A210}$$

Taking matrix elements gives

$$G_{1'}^{2'}(t_2, t_1) = G_{1'}^{n'}(t_2, t'_M) \ldots G_{l'}^{k'}(t'_{a+1}, t'_a) \ldots G_{i'}^{2'}(t'_1, t_0) \, , \tag{A211}$$

where the indices i, …, n run over all nonzero states. Because relaxation is only downward, all but one of these matrix elements must be diagonal. The only remaining terms are

$$G_{1'}^{2'}(t_2, t_1) = \sum_{a=1}^{N-1} G_{1'}^{1'}(t_2, t'_{a+1}) G_{1'}^{2'}(t'_{a+1}, t'_a) G_{2'}^{2'}(t'_a, t_1) \, , \tag{A212}$$

where sequences of diagonal elements have been recombined. The limit $M \quad \infty$ and $dt' = t'_{a+1} - t'_a \quad 0$ can now be applied. Equation (7) provides the infinitesimal Green's operator

$$\mathbf{G}(t + dt', t) = 1 - \mathbf{R}(t) dt' \, , \tag{A213}$$

resulting in

$$G_{1'}^{2'}(t_2, t_1) = -\int_{t_1}^{t_2} G_{1'}^{1'}(t_2, t') R_{1'}^{2'}(t') G_{2'}^{2'}(t', t_1) dt' \, . \tag{A214}$$

Using Eq. (32) for the rate matrix element gives Eq. (50) of the main text.

We now use the specific structure of an excitonic rate matrix [Eq. (32)] to replace the off-diagonal rate with a diagonal element:

$$G_{1'}^{2'}(t_2,t_1)=\int_{t_1}^{t_2}G_{1'}^{1'}(t_2,t')R_{1'}^{1'}(t')G_{2'}^{2'}(t',t_1)dt' . \tag{A215}$$

Because relaxation is only downward, Eq. (7) also applies to diagonal matrix elements and yields

$$G_{1'}^{2'}(t_2,t_1)=\int_{t_1}^{t_2}\left(\frac{d}{dt'}G_{1'}^{1'}(t_2,t')\right)G_{2'}^{2'}(t',t_1)dt' . \tag{A216}$$

Integration by parts gives

$$\begin{aligned}G_{1'}^{2'}(t_2,t_1)&=G_{2'}^{2'}(t_2,t_1)-G_{1'}^{1'}(t_2,t_1)\\&-\int_{t_1}^{t_2}G_{1'}^{1'}(t_2,t')\left(\frac{d}{dt'}G_{2'}^{2'}(t',t_1)\right)dt' .\end{aligned} \tag{A217}$$

This form can be used directly to derive Eq. (67) in the limit of zero incoherent coupling [Eq. (66)].

To look at the opposite limit of strong coupling, we define a change in occupation of |1′],

$$\delta G_{1'}^{1'}(t,t_1)=1-G_{1'}^{1'}(t,t_1) , \tag{A218}$$

which is assumed to be small over the biexciton lifetime. The term in Eq. (A217) can be written

$$G_{1'}^{1'}(t_2,t)=\frac{G_{1'}^{1'}(t_2,t_1)}{1-\delta G_{1'}^{1'}(t,t_1)} . \tag{A219}$$

Putting a power series expansion of Eq. (A219) into Eq. (A217) and integrating the first term leads to

$$\begin{aligned} G_{1'}^{2'}(t_2,t_1) = G_{2'}^{2'}(t_2,t_1) - G_{1'}^{1'}(t_2,t_1)\Big[& G_{2'}^{2'}(t_2,t_1) \\ & + \int_{t_1}^{t_2} \delta G_{1'}^{1'}(t',t_1) k_2(t') dt' \\ & + \frac{1}{2}\int_{t_1}^{t_2} \left(\delta G_{1'}^{1'}(t',t_1)\right)^2 k_2(t') dt' + \ldots \Big]. \end{aligned} \tag{A220}$$

Keeping only the leading term give Eq. (51) of the main text. The same results hold if the states 2′ and 1′ are replaced by any two neighboring states.

We note that a simple, empirical formula interpolates between the limits of strong [Eq. (51)] and zero [Eq. (67)] incoherent coupling:

$$G_{1'}^{2'}(t_2,t_1) = \frac{G_{2'}^{2'}(t_2,t_1)}{G_{1'}^{1'}(t_2,t_1)}\left(1 - G_{1'}^{1'}(t_2,t_1)\right). \tag{A221}$$

The accuracy of this approximation has not been tested.

One can consider couplings outside this range. In this case, the biexciton decay rate is less than twice the exciton decay rate. The presence of a second excitation slows the decay of the first. Although this situation is not forbidden, it is uncommon.

APPENDIX C – PHASE-DEPENDENT TRANSIENT-GRATING DATA AND CROSS RELAXATION TERM

1. Static Absorption Spectrum

The static absorption spectrum of the sample is shown in Figure S1. The band-edge transition forms a defined peak that is well matched to the laser spectrum.

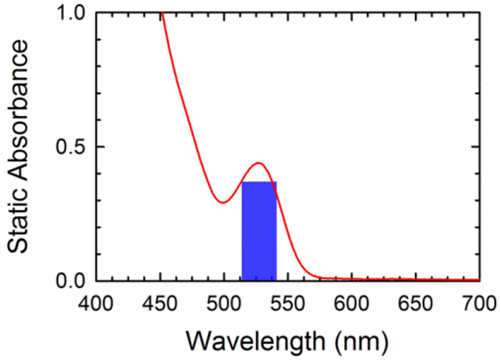

Figure C1. The static absorption spectrum $A'^{(0)}$ of the sample (red). The frequency and approximate bandwidth of the laser pulses are indicated by the blue bar.

2. Phase-Dependent Transient-Grating Data

The process of reducing phase-dependent data to the decay of a complex absorbance was illustrated using 2D MUPPETS data in Figure 3. An example of phase-dependent transient-absorption data and its reduction is shown in Figure S2. The real and imaginary parts shown in Figure S2B are converted to phase and magnitude before contributing to Figure 5A–B.

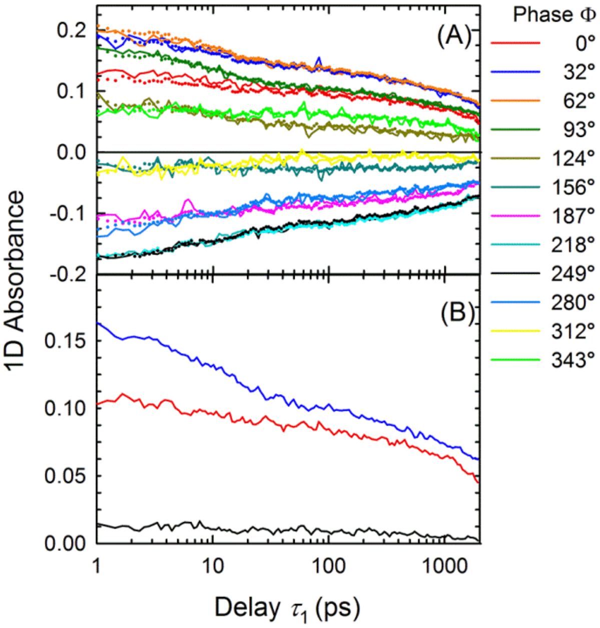

Figure C2. Extracting a complex absorbance from a phase-dependent signal. (A) Transient-grating absorbance versus phase Φ, $A^{(1)}(\tau_1;\ \Phi)/A'^{(0)}$, for 3.3 nJ pulses (solid). (B) Fourier decomposition of the data in (A) yields cosine (red), sine (blue) and DC (black) components.[1] Reconstructing the data in (A) from the components in (B) gives the dots shown in (A). The cosine and sine components must be rotated to the correct absolute phase to obtain the real and imaginary parts of the absorbance (see Figure 5A–B). Compare to Figure 3.

3. Cross-Relaxation Formulas

The formula for the 1D cross-correlation function $C_{1'}^{2'}(\tau_1)$ was given in eq 19. The 2D cross-relaxation function $C_{1'1'}^{2'}(\tau_2,\tau_1)$ differs for each of the four models used in section 4.5 of chapter 4. Reference 2 [eqs (49) and (51)] shows that when the cross-relaxation is small,

$$C_{1'1'}^{2'}(\tau_2,\tau_1) = C_{2'1'}(\tau_2,\tau_1) - \left\langle G_{2'}^{2'}(t_2,t_1) G_{1'}^{1'}(t_2,t_0) G_{1'}^{1'}(t_2,t_0) \right\rangle, \tag{S1}$$

where $G_j^i(t_1,t_0)$ is the probability for a single molecule to evolve from state i at time t_0 to state j at time t_1.

If the exciton and biexciton dynamics are uncorrelated, eq S1 reduces to

$$C_{1'1'}^{2'}(\tau_2,\tau_1)=C_{2'}(\tau_2)\left(C_{1'}(\tau_1)-C_{1'1'}(\tau_1,\tau_2)\right). \tag{S2}$$

When the exciton decay is also homogeneous (model one), eq 22 holds and

$$C_{1'1'}^{2'}(\tau_2,\tau_1)=C_{2'}(\tau_2)C_{1'}(\tau_1)\left(1-C_{1'}(\tau_2)\right). \tag{S3}$$

On the other hand, when the exciton decay is heterogeneous (model two), eq 21 holds and

$$C_{1'1'}^{2'}(\tau_2,\tau_1)=C_{2'}(\tau_2)\left(C_{1'}(\tau_1)-C_{1'}(\tau_2+\tau_1)\right). \tag{S4}$$

When the exciton and biexciton dynamics are correlated, eq S1 is rewritten with all the time evolution terms starting at t_0

$$C_{1'1'}^{2'}(\tau_2,\tau_1)=C_{2'1'}(\tau_2,\tau_1)-\left\langle \frac{G_{2'}^{2'}(t_2,t_0)}{G_{2'}^{2'}(t_1,t_0)}G_{1'}^{1'}(t_2,t_0)\right\rangle. \tag{S5}$$

If the decays are homogeneous (model four), the ensemble average is not important. We also assume that the bath relaxation is the same in the exciton and biexciton states. Using eq 28, eq S5 reduces to

$$C_{1'1'}^{2'}(\tau_2,\tau_1)=\frac{C_{2'}(\tau_2+\tau_1)}{C_{2'}(\tau_1)}\left(C_{1'}(\tau_1)-C_{1'}(\tau_2+\tau_1)\right) \tag{S6}$$

In model three, there is an ensemble to average over, but it has just two members (see eqs 25 and 26). Thus, we combine two terms like the one in eq S6:

$$C_{1'1'}^{2'}(\tau_2,\tau_1)=aC_{1'1'a}^{2'}(\tau_2,\tau_1)+bC_{1'1'b}^{2'}(\tau_2,\tau_1) \tag{S7}$$

APPENDIX D – THERMAL TIME EVOLUTION OPERATOR AND FLUENCE-DEPENDENT MUPPETS PHASE DATA

1. Construction of the Model for $\mathbf{G}_\varepsilon$

The model for thermal time evolution is specified by the elements of the time-evolution operator $\left(\mathbf{G}_\varepsilon\right)_{j\,q}^{i\,p}(t_2,t_1)$. The electronic labels *i* and *j* are in the basis set of {0, 1, 2} representing the ground, exciton and biexciton states respectively (Figure I.7A). The labels *p* and *q* represent the quanta of solvent heat n_ε. The only elements needed are

$$\left(\mathbf{G}_\varepsilon\right)_{j0}^{i\,0} = \begin{pmatrix} G_2^2 & 0 & 0 \\ (1-Q_2)G_1^2 & G_1^1 & 0 \\ (1-Q_1)(1-Q_2)G_0^2 & (1-Q_1)G_0^1 & 1 \end{pmatrix}, \tag{S1}$$

$$\left(\mathbf{G}_\varepsilon\right)_{j1}^{i\,0} = \begin{pmatrix} 0 & 0 & 0 \\ Q_2G_1^2 & 0 & 0 \\ \left[(1-Q_1)Q_2+Q_1(1-Q_2)\right]G_0^2 & Q_1G_0^1 & 0 \end{pmatrix}, \tag{S2}$$

and

$$\left(\mathbf{G}_\varepsilon\right)_{j2}^{i\,0} = \begin{pmatrix} 0 & 0 & 0 \\ 0 & 0 & 0 \\ Q_1Q_2G_0^2 & 0 & 0 \end{pmatrix}. \tag{S3}$$

Here $G_j^i(t_2,t_1)$ are elements of the time-evolution operator for the solute electronic states, Q_1 is the fraction of the electronic energy that appears as solvent heat upon relaxation of the exciton to the ground state, and Q_2 is the fraction electronic energy that appears as solvent heat upon relaxation of the biexciton to the exciton. For simplicity, the time variables are suppressed. In writing these equations, it was assumed that the decay of the biexciton to the ground state occurs in sequential steps, $\left(G_\varepsilon\right)_{02}^{20} = \left(G_\varepsilon\right)_{02}^{11}\left(G_\varepsilon\right)_{11}^{20}$.

Once written in this unprimed, eigenstate basis, the solute portions of the matrices are transformed to the primed, exciton basis using the transformation matrices[1]

$$\mathcal{T}_{j'}^{j} = \sqrt{2}\begin{pmatrix} 1 & 0 & 0 \\ 1 & 1 & 0 \\ 1/\sqrt{2} & 1/\sqrt{2} & 1/\sqrt{2} \end{pmatrix} \tag{S4}$$

and

$$\left(\mathcal{T}^{-1}\right)_{j'}^{j} = \frac{1}{\sqrt{2}}\begin{pmatrix} 1 & 0 & 0 \\ -1 & 1 & 0 \\ 0 & -1 & \sqrt{2} \end{pmatrix} \tag{S5}$$

In the primed basis set, only elements with $j' = 0'$ and $p \neq 0$ will create a detectable signal. Also, because thermal signals do not propagate across multiple time periods, only $q = 0$ elements are relevant. Thus, the only portions of the transformed matrices that are needed are

$$\left(\mathbf{G}_\varepsilon\right)_{0'1}^{i'\,0} = \frac{1}{\sqrt{2}}\begin{pmatrix} \begin{matrix}\left[\left(1-Q_1\right)Q_2 + Q_1\left(1-Q_2\right)\right]G_0^2 \\ +Q_2 G_1^2 - Q_1 G_0^1\end{matrix} & Q_1 G_0^1 & 0 \end{pmatrix} \tag{S6}$$

and

$$\left(\mathbf{G}_{\varepsilon}\right)^{i'\,0}_{0'\,2} = \frac{1}{\sqrt{2}} \begin{pmatrix} Q_1 Q_2 G_0^2 & 0 & 0 \end{pmatrix} \tag{S7}$$

Completing the transformation requires that the elements G_j^i appearing in the matrices be transformed to the primed basis set. This process yields

$$\left(\mathbf{G}_{\varepsilon}\right)^{i'\,0}_{0'\,1} = \frac{1}{\sqrt{2}} \begin{pmatrix} \begin{array}{c} Q_2\left(1 - G^{2'}_{2'}\right) - Q_1 G^{2'}_{1'} \\ -2 Q_1 Q_2 G^{2'}_{0'} \end{array} & Q_1 G^{1'}_{0'} & 0 \end{pmatrix} \tag{S8}$$

and

$$\left(\mathbf{G}_{\varepsilon}\right)^{i'\,0}_{0'\,2} = \frac{1}{\sqrt{2}} \begin{pmatrix} Q_1 Q_2 G^{2'}_{0'} & 0 & 0 \end{pmatrix} \tag{S9}$$

The final simplification is to recognize that the linearity of the thermal response allows the substitution |*i*′ 2] → 2|*i*′ 1]. Thus, eqs S8 and S9 are combined

$$\begin{aligned} \left(\mathbf{G}_{\varepsilon}\right)^{i'\,0}_{0'\,1} + 2\left(\mathbf{G}_{\varepsilon}\right)^{i'\,0}_{0'\,2} &\rightarrow \left(\mathbf{G}_{\varepsilon}\right)^{i'\,0}_{0'\,1} \\ &= \frac{1}{\sqrt{2}} \begin{pmatrix} Q_2\left(1 - G^{2'}_{2'}\right) - Q_1 G^{2'}_{1'} & Q_1 G^{1'}_{0'} & 0 \end{pmatrix}, \end{aligned} \tag{S10}$$

and $\left(\mathbf{G}_{\varepsilon}\right)^{i'\,0}_{0'\,2}$ is dropped from the problem. This result corresponds to eqs 49 and 50 of the main text.

2. Fluence-Dependent MUPPETS Phase Data

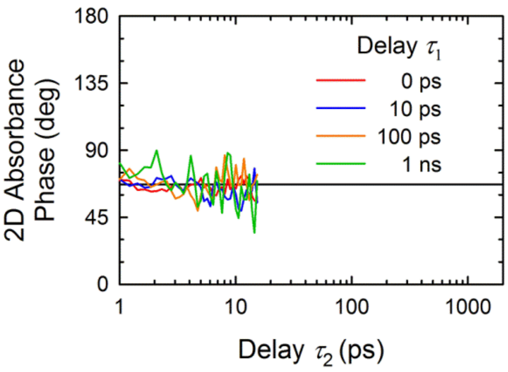

Figure D1. Phases of the fluence-dependent component of the MUPPETS data at various values of τ_1. The corresponding magnitudes are given in Figure 4A. The phases are expected to be constant at the phase of the biexciton transition, $\Phi_{12} = 67°$ (black line).

APPENDIX E – SUPPORTING INFORMATION FOR "TWO-DIMENSIONAL ANISOTROPY MEASUREMENTS SHOW LOCAL HETEROGENEITY IN A POLYMER MELT"

I. Pyrromethene 597

Pyrromethene 597 has many properties desirable for a rotational probe of solvent structure.[157-159] It has a symmetric, compact shape (Figure E1), high fluorescence and low triplet quantum yields, and good photochemical stability. It is soluble in a wide range of solvents, but its photophysical properties are insensitive to solvent. In particular, solvent induced Stokes shifts are small.

To the best of our knowledge, ours is the first use of this molecule as a rotational probe. The results in toluene (Figure 1) are simple and conventional. They confirm that PM597 has no unusual properties on its own and is a good reporter of the local solvent structure.

II. 1D anisotropy decays

1D anisotropies were measured in the apparatus shown in Figure 2 using only beams 1*a* and 3*b*. Typical results are shown in Figure E3 and Table S1.

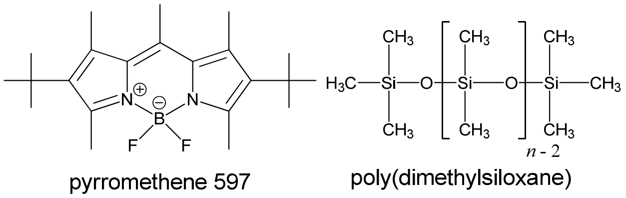

Figure E1. Left: Chemical structure of the probe molecule, pyrromethene 597 (PM597). Chemical name: 1,3,5,7,8-penta-methyl-2,6-di-*t*-butylpyrromethene difluoroborate complex. CAS#: 137829-79-9. Right: Chemical structure of PDMS.

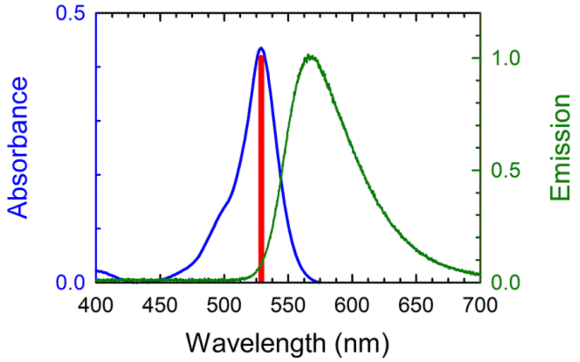

Figure E2. Absorption (blue) and emission (green, arbitrary intensity) spectra of the sample (PM597 in 5970 g/mol PDMS). The red bar indicates the wavelength and bandwidth of the optical pulses used.

Although eqs 1 and 6 are correct for an idealized experiment, it is common to introduce a factor *g* to correct for small polarization errors in the real experiment. Thus, we have used

$$r^{(1)}(\tau_1) = \frac{A^{(1)}(\tau_1;0°) - gA^{(1)}(\tau_1;90°)}{A^{(1)}(\tau_1;0°) + 2gA^{(1)}(\tau_1;90°)} \tag{S222}$$

and

$$r^{(2)}(\tau_2,\tau_1) = \frac{A^{(2)}(\tau_2,\tau_1;\theta_m,\theta_m) - gA^{(2)}(\tau_2,\tau_1;-\theta_m,\theta_m)}{5A^{(2)}(\tau_2,\tau_1;\theta_m,\theta_m) + 7gA^{(2)}(\tau_2,\tau_1;-\theta_m,\theta_m)} \tag{S223}$$

Because the anisotropy is not exactly zero at the end of our time range, we adjust *g* to make the anisotropy decay exponentially in its tail. A value of $g = 0.95$ was chosen for the 1D measurements and $g = 0.88$ for the 2D measurements.

Our 1D magic-angle results (Figure E3a) fit well to a single exponential with a lifetime (4.3 ns) close to that of previous reports (3.91 ns).[157]

Table S1. Fit parameters and physical properties of PDMS: molecular weight *M*, number of monomers *n*, viscosity *η* and stretched-exponential fit parameters *T* and *β* (see Figure 1b).

	M (g/mol)	n	η (cP)	T (ps)	β
Toluene	92	—	0.6	52.6	1.0
PDMS	770	10	4.6	200	0.74
PDMS	5 970	76	97	400	0.69
PDMS	17 250	221	486	424	0.70

III. MUPPETS-Phase measurements

In general, the signal in a heterodyned experiment, such as MUPPETS, contains both components due to changes in absorption and index-of-refraction. These are expressed as a complex absorbance with a phase representing the ratio of absorptive and index-of-refraction responses.[21] If there are spectral changes during the decays, the phase is time-dependent and corrections must be applied to separate spectral decays from spectral shifts. PM597 is known to have small Stokes shifts and the solvents used have low polarity, so large spectral changes are not anticipated.

Figure E4 shows an experimental test for this complication. The raw signals versus the phase delay between the two probe beams are shown in Figure E4a. A Fourier analysis of these data[21] yields the magnitude and phase of the sample shown in Figure E4b. All reported phases are relative; no calibration of the absolute phase was done. The phase is time independent, which allows uncorrected magnitudes to be used throughout the main part of the paper. The reported data consist of the difference of just two phases separated by 180°.

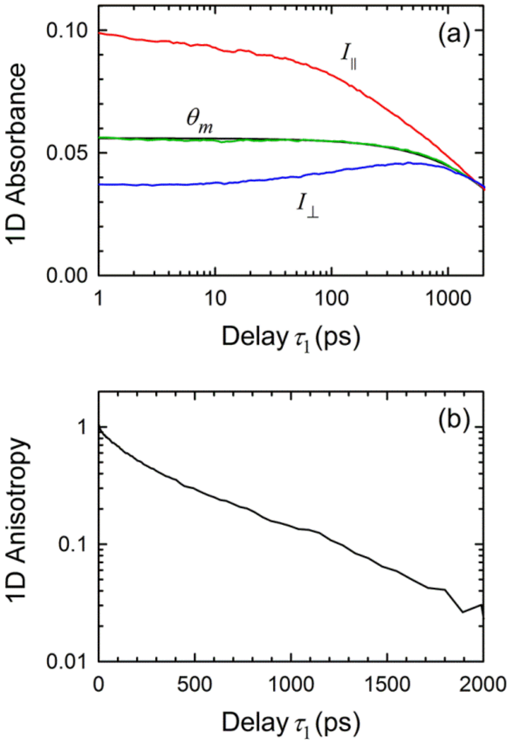

Figure E3. An example of the data used to generate the anisotropy decay curves shown in Figure 1(a) of the main text. (a) Pump–probe decays of PM597 in 5970 g/mol PDMS with parallel (red), perpendicular (blue), and magic-angle (green) polarizations. The black curve is an exponential fit. (b) 1D anisotropy derived from (a) using eq 1.

IV. Isotropic-MUPPETS results

To focus on rotational dynamics, a probe's electronic-state decay should have neither dispersion nor heterogeneity. Figure E5 shows the 2D electronic-state data derived from the sum of our polarized results,

$$C^{\{0,0\}}(\tau_2,\tau_1) \propto 5A^{(2)}(\tau_2,\tau_1;\theta_m,\theta_m) \\ +7gA^{(2)}(\tau_2,\tau_1;-\theta_m,\theta_m)\,. \qquad \text{(S224)}$$

The decays in Figure E5 fit to a single exponential with a time constant of 2.1 ns. This value is shorter than the one obtained from the 1D magic-angle measurement (Figure E3a). The reason for this discrepancy is not understood at present.

The results are invariant to τ_1, so there is no possibility of electronic-state heterogeneity contaminating our rotational results.

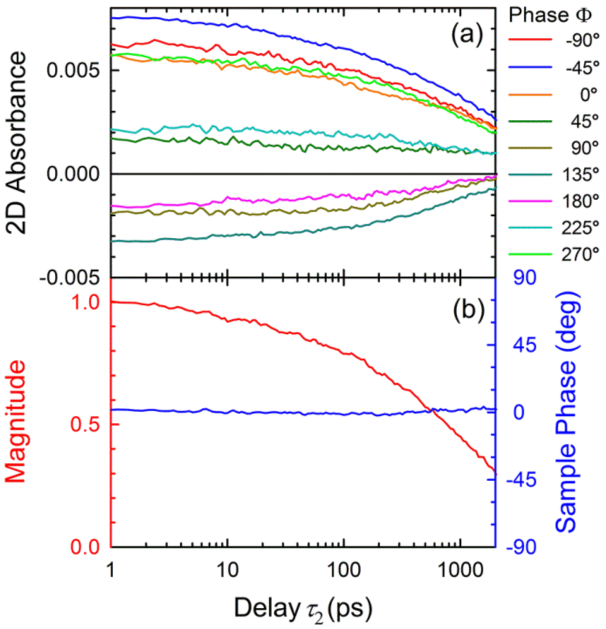

Figure E4. (a) A series of MUPPETS data taken of PM597 in 5970 g/mol PDMS in different experimental phase angles Φ at $\tau_1 = 0$. (b) The magnitude (red) and relative sample phase (blue) extracted from the data in (a).

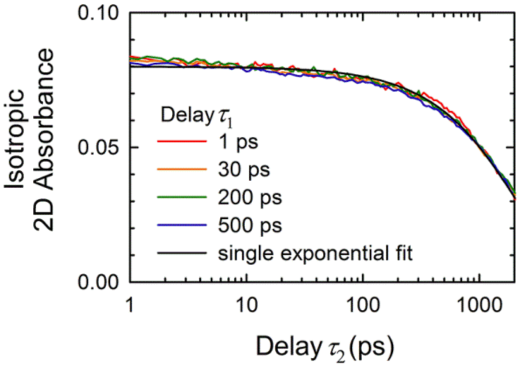

Figure E5. 2D isotropic signals calculated from the data in Figure 3a calculated from eq 7.